Journal of Materials Chemistry A

REVIEW

View Article Online
View Journal | View Issue

Cite this: J. Mater. Chem. A, 2023, 11, 17977

Solid oxide electrolysis cells – current material development and industrial application

Stephanie E. Wolf, †[ab] Franziska E. Winterhalder, †[cd] Vaibhav Vibhu, [a] L. G. J. (Bert) de Haart, [a] Olivier Guillon, [cd] Rüdiger-A. Eichel [ab] and Norbert H. Menzler *[cd]

Solid Oxide Electrolysis Cells (SOECs) have proven to be a highly efficient key technology for producing valuable chemicals and fuels from renewably generated electricity at temperatures between 600 °C and 900 °C, thus providing a carbon-neutral method for energy storage. The successful implementation of this technology on an industrial level in particular requires the long-term stability of all system components with a concurrent overall degradation rate of a maximum of 0.75% kh^{-1} or even better 0.5% kh^{-1}, corresponding to a performance loss of 20% over approx. five years under constant operating parameters. However, the materials currently used for SOEC systems have been developed and optimized in recent decades for fuel cell operation. The degradation of these Solid Oxide Fuel Cell (SOFC) materials used in SOECs, however, slows down the technology and market ramp-up. Accordingly, a selection and development of materials specifically for use in SOEC operation, must therefore be based not only on the highest performance but also on the lowest achievable degradation rate. In general, the systematic development of new SOEC materials must be driven towards key performance parameters such as mechanical, thermal, and chemical stability as well as an application-oriented assessment (cost effectiveness, simple manufacturing). This review presents the state-of-the-art materials in current industrial use for planar SOECs as well as future challenges regarding materials design and degradation. Recent advances in material compositions are discussed and evaluated in terms of their performance, stability, and potential for industrial implementation. In addition, a materials selection for interconnects, coatings, and sealants is briefly listed to outline current developments in these areas.

Received 11th April 2023
Accepted 22nd June 2023

DOI: 10.1039/d3ta02161k

rsc.li/materials-a

1. Introduction

The detrimental impact of fossil-fuel-based energy carriers on the global climate has led to an increasing interest in carbon-neutral energy technologies such as wind, solar, and biomass to renewably generate electricity and the usage of green hydrogen (H_2) as an energy carrier. Hydrogen can also be stored and re-electrified in a fuel cell, as well as be used as a sustainable feedstock for the chemical industry (power-to-X, power-to-fuel, power-to-chemicals, power-to-heat), thus facilitating the large-scale integration of renewables, enabling efficient global energy logistics and locally supporting the balancing of the grid.

Due to its versatile application possibilities, hydrogen plays a key role in a future sustainable energy system as a coupling element for different sectors. Therefore, in addition to an intensive expansion of renewably generated power, a flexible hydrogen infrastructure is necessary. Hydrogen is a non-toxic energy carrier with a high mass-based specific energy content that can be produced in either a carbon-neutral or carbon-free manner. The chemical industry and refineries are currently the main hydrogen consumers. Of the total hydrogen production in 2020 (90 Mt), 44% (40 Mt) was used for the production of valuable oil products in refineries through hydrocracking and hydrotreatments for the desulfurization of fossil fuels.[1] An additional 45 Mt H_2 was consumed in the chemical industry as a basic component for the production of methanol and ammonia.[1] The remaining 5 Mt were mostly used for steel-making with less than 0.02% H_2 (<20 kt H_2) used for transport. Hydrogen fuel produced from renewably generated power sources could decarbonize these sectors as well as various energy-intensive industries (*e.g.*, steel), the mobility sector, and residential heating demand. Using natural resources also means a reduction in the price of generating electricity.

[a]*Forschungszentrum Jülich GmbH, Institute of Energy and Climate Research, IEK-9: Fundamental Electrochemistry, 52425, Jülich, Germany*

[b]*RWTH Aachen University, Institute of Physical Chemistry, 52074, Aachen, Germany*

[c]*Forschungszentrum Jülich GmbH, Institute of Energy and Climate Research, IEK-1: Materials Synthesis and Processing, 52425, Jülich, Germany. E-mail: n.h.menzler@fz-juelich.de*

[d]*RWTH Aachen University, Institute of Mineral Engineering (GHI), Department of Ceramics and Refractory Materials, 52074, Aachen, Germany*

† These authors contributed equally to the publication.

Strategies are being implemented worldwide to build a hydrogen economy and infrastructure, as highlighted in Fig. 1. The political effort to increase hydrogen production includes supporting research and innovation projects, scaling up and decarbonizing existing hydrogen production facilities, expanding logistics infrastructure, and establishing larger-scale storage facilities. Europe is expected to achieve climate neutrality in 2050, which is why a continent-wide hydrogen network is planned. A significant aspect is the repurposing of *e.g.*, existing natural gas pipelines for the global hydrogen trade of gaseous hydrogen to lower the delivery costs. The hydrogen pipeline network may connect industrial end users with large-scale electrolyzers also found outside of the EU. In addition, establishment of new pipeline networks to transport hydrogen as ammonia, methanol, and liquid organic hydrogen carriers (LOHC) is considered.[2]

In particular, green hydrogen produced by renewably generated power sources is considered essential for a sustainable transition of the energy system. However, current hydrogen production is mainly based on gray power sources. Hydrogen production routes and sources are shown in Table 1 with the corresponding color encoding according to their present-day classification.[1] Hydrogen production *via* coal gasification results in high carbon emissions and the end product is referred to as black or brown hydrogen depending on the coal type. Hydrogen produced by the steam methane reforming (SMR) of natural gas was the main source of hydrogen in 2020, representing 59% of global production. In naphtha reforming, most refineries produce hydrogen as a by-product, with 21% of global hydrogen production attributed to this route. Obtaining hydrogen from oil oxidation, on the other hand, is negligible at 0.6%. All three synthesis routes produce grey hydrogen and are considered 'carbon-positive' technologies. The industrial

Stephanie E. Wolf graduated with distinction from RWTH Aachen University, Germany, in 2020 with a degree in chemistry, focusing on catalysis, computational chemistry, and spectroscopy. Since October 2020, she has been working as a PhD candidate at the Institute of Energy and Climate Research (IEK-9: Fundamental Electrochemistry) at Forschungszentrum Jülich. Her fields of research include material synthesis, chemo-physical material characterization, solid oxide cell preparation, electrochemical cell characterization, long-term degradation studies as well as postmortem analyses.

Franziska E. Winterhalder is currently pursuing her PhD in materials engineering at the Institute of Energy and Climate Research (IEK-1: Materials Synthesis and Processing) at Forschungszentrum Jülich under the supervision of Norbert H. Menzler. She received her Master's degree in Materials Sciences from the Friedrich Schiller University Jena in 2021. Her research interests include material development and engineering for solid oxide cells, currently focusing on alternative fuel electrodes.

Vaibhav Vibhu studied chemistry and obtained his master's degree from the University of Delhi and the University of Grenoble Alpes. He then completed his PhD in 2016 at the ICMCB-CNRS, University of Bordeaux, France, on "Stability and ageing studies of praseodymium-based nickelates as cathodes for SOFCs". Afterward, he moved to IEK-9 at Forschungszentrum Jülich, Germany, to continue his work in the field of solid oxide cells (SOFCs/SOECs). His research focuses on the development of electrode materials, materials characterizations and processing, the manufacturing of cells, electrochemical characterizations and the identification of reaction mechanisms of electrodes and degradation phenomena of cells.

*L. G. J. (Bert) de Haart (*1958) studied Chemistry at State University of Utrecht (The Netherlands) and obtained his Master degree (Drs.) with specialty Solid State Chemistry in 1981. In 1985 he obtained his PhD degree (Dr) also from the State University of Utrecht. From 1987–1992 he was research assistant (Post-Doc) at the University of Twente (The Netherlands) in the Department of Chemical Technology. In 1992 he joined the Forschungszentrum Jülich (Germany) where he continued his work on the development of Solid Oxide Fuel and Electrolysis Cells (SOFC/SOEC) with emphasis on materials development and cell- and stack-design, -manufacturing and -characterization.*

chloralkali process generates clean, white hydrogen as a by-product, although it does produce CO_2 emissions, which stem from electricity produced to operate the electrolyzers. In recent years, low-carbon hydrogen technologies have emerged. Blue hydrogen is classified as production using the SMR process, with the subsequent storage of carbon emissions (CCS). This method still has a low share of global H_2 production (0.7%) and is considered a bridging technology. Hydrogen production from fossil fuels has the disadvantage that the gaseous product stream has to be treated in downstream processes to reach an adequate level of purity for further catalytic utilization. Green hydrogen is produced by water electrolysis based on various renewable energy sources. The electrochemical conversion of water to hydrogen results in an almost pure product gas without detrimental impurities. To achieve the goal of net-zero carbon emissions by 2050, water electrolyzer capacities will have to be increased to meet the increasing demand for green hydrogen especially in the additional field of energy logistics.[3]

Water electrolyzers are classified, depending on their operating conditions and charge carrier type (OH^-, H^+, O^{2-}), as alkaline electrolyzers, proton exchange-membrane (PEM) electrolyzers, and solid oxide electrolyzers (SOE). Alkaline electrolysis is a commercially mature, low-cost, and stable technology, usually operated at 20–80 °C, up to 30 bar, with process efficiency of about 62–82%.[4,5] The charged Raney nickel electrodes are immersed in a liquid alkaline electrolyte, which is commonly potassium hydroxide (KOH). A diaphragm permeable only for OH^- anions separates the product gases. Polymer electrolyte membrane (PEM) electrolysis is also commercially available and can operate at high current densities of around -2 A cm^{-2} to -3 A cm^{-2} between 50–80 °C. Compared to alkaline electrolyzers, the polymer electrolyte membrane Nafion® is much thinner, provides good proton conductivity (0.12 ± 0.04 S cm^{-1}),[6] and has a quicker input response. This results in efficiencies of 67–82% for PEM electrolyzers. The use of expensive noble metal electrodes, for example, Ir, Pt, Ru, and Pr, is essential due to the acidic environment.[4] In anion exchange membrane (AEM) electrolyzers, the conventional diaphragm of alkaline electrolyzers is replaced with a quaternary ammonia (polysulfone) AEM permeable for negatively charged OH^- ions. These membranes are less expensive than Nafion®-based membranes in PEM electrolysis and enable the use of transition metal catalysts instead of noble metals. AEM electrolysis is still a developing technology operated at 50–70 °C with up to -1.0 A cm^{-2} at ~2 V and a current efficiency of ~40%.[7,8] The specific technological comparison of the limitations, advantages, and disadvantages of different electrolyzer systems depends on the application as well as on the economic and ecological point of view. However, this is not the focus point of this paper and is discussed in more detail elsewhere.[9–11]

Electrochemical energy conversion to generate chemical fuels with high efficiency is possible in traditional oxide ion-conducting electrolysis cells (SOECs) as well as protonic

Olivier Guillon is a materials scientist and engineer. He became director at the Institute of Energy and Climate Research – Materials Synthesis and Processing (IEK-1, Forschungszentrum Jülich) and professor at the RWTH Aachen University in 2014. He is the spokesperson of the research program "Materials and Technologies for the Energy Transition" within the Helmholtz Association and works on ceramic materials and components for solid oxide fuel and electrolysis cells, gas separation membranes, solid-state batteries and high-temperature applications. He has published more than 300 articles in international referred journals and is member of the World Academy of Ceramics, fellow of the American and European Ceramic Societies.

Rüdiger-A. Eichel studied physics at the University of Cologne and completed his PhD at the Swiss Federal Institute of Technology (ETH) in Zurich. In 2012, he became a director at the IEK-9 at Forschungszentrum Jülich and simultaneously was appointed full professor for physical chemistry at RWTH Aachen University. His research interests in the field of solid oxide cells focus on the development, characterization, and optimization of high-temperature electrolysis and fuel cell stacks and systems. In his institute, systems and system components are conceived, designed, modeled, built as well as tested, and electrochemically analyzed.

Norbert H. Menzler studied Materials Science at the University of Erlangen–Nuremberg from where he got his Diploma and his PhD Afterwards, he acted as a Managing Director of a Bavarian research network. In 2000 he joined Forschungszentrum Jülich working now on solid oxide cells. His specialization is the cell materials, their processing, and the post-test analysis of operated stacks. Since 2016 he has been the head of the solid oxide cell department of the Institute of Energy and Climate Research (IEK-1: Materials Synthesis and Processing). In 2019 he received an honorary professorship from the RWTH Aachen University.

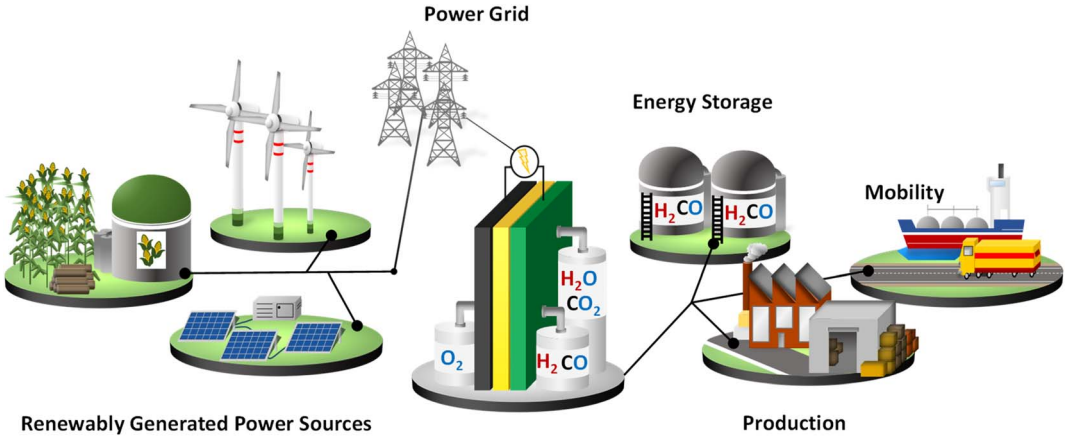

Fig. 1 Schematic representation of a hydrogen infrastructure: renewably generated power is used to generate hydrogen through a high-temperature solid oxide electrolysis cell (SOEC). Energy-intensive industries, *e.g.*, production and mobility, are powered by the low-emission energy carrier hydrogen, and surplus chemical energy is stored.

Table 1 Types of hydrogen generation methods and sources with the corresponding theory of hydrogen colors. The percentage share of production for 2020 is shown along with the generation method[1]

Color	Source	Method	Production in 2020[a]/%
Black H_2	Black coal	Gasification	19%
Brown H_2	Brown coal/lignite	Gasification	
Grey H_2	Natural gas	Natural gas reforming	59%
	Oil	Partial oxidation	0.6%
	By roduct	Naphtha reforming	21%
White H_2	By product	Chloralkali electrolysis	
Blue H_2	Natural gas + carbon capture and storage (CCS)	Natural gas reforming	0.7%
Turquoise H_2	Methane	Pyrolysis	
Pink H_2	Nuclear energy	Water electrolysis	
Yellow H_2	Mixed grid energy	Water electrolysis	
Green H_2	Renewable-generated power sources	Water electrolysis	0.03%

[a] Production is calculated as more than 100% in reference.

ceramic electrolysis cells (PCECs). Proton-conducting materials have attracted increasing interest due to their lower operating temperatures (450–700 °C).[12] As proton-conducting cells are currently still in the development phase and not commercially available, this review focuses on commercially available oxygen ion-conducting electrolysis cells. Solid oxide electrolyzer cells (SOECs) are typically operated between 600 °C and 900 °C, consist of two porous electrodes separated by a dense pure oxide-ion conducting electrolyte, and can achieve technical efficiencies up to 100% due to advantageous thermodynamics and reaction kinetics.[13–15] In steam electrolysis, steam (H_2O) is electrochemically reduced to hydrogen (H_2) at the negatively charged fuel electrode. The resulting oxide ions migrate through the electrolyte to the positively charged oxygen electrode, where they are oxidized to molecular oxygen (eqn (1) and (2)). Green CO production through direct CO_2 electrolysis is also feasible in SOECs.[16] This process has attracted increasing interest in a possible "closed recycling loop" within the synthetics industry (eqn (3)). A unique advantage of SOECs is also the direct production of syngas (H_2 + CO) through co-electrolysis, which is the simultaneous conversion of H_2O and CO. H_2 : CO ratios from 1 : 1 to 3 : 1, which are currently of great importance in the chemical industry, can be achieved using high-temperature SOECs.[17] The operating conditions and equilibrium process impact the (reverse) water gas shift reaction ((R)WGS) (eqn (4)) occurring during the co-electrolysis process, with the product ratio on the fuel side being variable. Synthetic natural gas and methane are derived from methanation with an H_2 : CO ratio of 3 : 1. In Fischer–Tropsch synthesis, syngas with lower ratios of 1.8 : 1.2 is used to generate liquid hydrocarbons, for example, synthetic fuels and chemical lubricants.[18,19] Additionally, aldehydes synthesized *via* the "oxo process" hydroformylation are valued products and give way to bulk chemicals such as esters, alcohols, and amines.[20]

$$2H_2O + 4e^- \rightarrow 2H_2 + O_2 \quad (1)$$

$$O^{2-} \rightarrow 2e^- + O_2 \quad (2)$$

$$2CO_2 + 4e^- \rightarrow 2CO + O_2 \quad (3)$$

$$CO_2 + H_2 \rightleftarrows H_2O + CO \quad (4)$$

The high operating temperature is the main advantage of SOECs, which results in lower ohmic losses compared to alkaline and proton exchange membrane electrolyzers as well as advantageous kinetics and thermodynamics. The required process enthalpy ΔH of the endothermic steam reduction process can be supplied in the form of heat and electrical energy (Gibbs energy ΔG). With increasing temperatures, the enthalpy increases slightly for steam reduction while the electrical energy demand ΔG becomes smaller at higher temperatures. The remaining energy demand $T\Delta S$ can be supplied in the form of heat.[21] By integrating the electrolyzer system into pre-existing chemical industry plants, the heat demand can be supplied from the external waste heat of exothermic downstream chemical processes, for example, the production of synthetic fuels, ammonia, or industrial processes such as the production of steel, copper, aluminum, cement, or ceramics. In addition, the internal cell resistances lead to the production of Joule heat, which adds to the enthalpy for educt-to-product conversion. At the thermo-neutral voltage E_{tn}, the exact power required for the endothermic electrolysis process is produced, and therefore no external thermal management is necessary aside from compensating for the heat loss to the surroundings. The energy efficiency of up to 100% and the use of inexpensive catalyst materials make SOEC systems more cost-effective in comparison to alkaline and PEM electrolyzers.[22]

The current demonstrator systems for SOECs on laboratory and industrial scales have been tested for up to 23 000 h at a high current density of -0.9 A cm^{-2} with a voltage increase of 7.4 mV kh^{-1} (Table 2). Between 2016 and 2019, the European project GrInHy manufactured an rSOC system (reversible solid oxide cell) with 48 stacks, each with 30 Sunfire cells, arranged in six modules, with a power of 143 kW in electrolysis mode ($84\%_{el,LHV}$) and 30 kW ($48\%_{el,LHV}$) in fuel cell mode.[23] The world's most powerful industrial high-temperature electrolyzer (as of 2022) is showcased in the subsequent European collaboration project, GrInHy2.0, in which hydrogen is produced using waste heat from an iron and steel factory.[24] The industrial implementation of SOEC technology produces 200 Nm^3 h^{-1} green H_2 at 850 °C with a nominal power input of 720 kW and an electrical efficiency of $84\%_{el,LHV}$.

An example of a schematic layout of established stack systems is presented in Fig. 2 for the laboratory scale of the Jülich integrated module.[25] All necessary system parts are organized around the integrated module and inlet fuels are kept at room temperature before being fed into the system. On the fuel side, steam and hydrogen can be supplied to the stack by mass flow controllers (MFCs). The steam is generated by the evaporation of demineralized water. The system is connected at the air side to inlet tubes for both compressed air as well as purified ambient air. Fuel and air are heated before being fed into the stack. Post-reaction, the gas mixture on the fuel side is separated into hydrogen and steam in a plate heat exchanger. In a downstream recirculation unit, the off-gas is condensed and compressed with a double-headed prototype diaphragm compressor to overcome the pressure drop of the recirculation loop. The product gas is cooled down and transported out of the system. The reintegration of off-heat and off-gas on the fuel side increases the efficiency of the system.[26–29] On the air side, the off-gas is partly recirculated and cooled down with heat exchangers, thus making way for fresh air. The system surrounding the integrated module is permanently ventilated with fresh air to reduce safety risks, for example, the ignition limits of hydrogen.

The long-term operation of solid oxide cells in fuel cell mode has been well developed and demonstrated for more than 100 000 h with a voltage degradation rate of only 0.5% kh^{-1}.[30] In contrast, SOEC stack designs still exhibit higher degradation rates of 0.6–1.5% kh^{-1}, depending on the respective operating conditions applied, for example, current density.[31] Table 2 provides an overview of long-term SOEC tests with different cell configurations and operating conditions conducted in cooperation between research institutes and industry. Long-term system durability is a key challenge to the increased economic competitiveness and more widespread industrial implementation of SOEC technology in the future.

The reliable long-term performance of an SOEC stack system requires all components to be thermally stable. However, state-of-the-art systems have shown several lifetime issues related to single-stack components. The interconnect plates separate the stacked ceramic cells to give mechanical stability, thus also separating the fuel and the air gas feed and connecting the electrical current. Cr alloys and high Cr-containing ferritic stainless steel (FSS) are currently used due to their good mechanical strength and matching thermal expansion coefficients (TECs) with other SOC stack materials. When operated at high temperatures, the metallic interconnect oxidizes in the presence of steam or oxygen. This promotes the growth of an electronically conductive oxide layer on the interconnect, which may lead to spallation phenomena. Additionally, further chromium oxidation can lead to the formation of Cr^{6+}, which is known to negatively impact the SOC electrodes *via* Cr evaporation[39] from the oxide scale and react either electrochemically or chemically.[40] Glass-ceramic sealants are used to separate the gas

Table 2 Steam electrolysis test overview performed on cell stack systems in fuel electrode (FE) and electrolyte-supported configurations

Operators	Degrad./% kh^{-1}	T °C	Time/h	Ref.
Electrolyte-supported cell-based stack				
Topsoe, EIFER	4.6–5.6	820	4055	32
INL, Ceramtec	5.6, 4.6	800	1000	33
IKTS	0.5	800	2100	34
Sunfire, EIFER	0.8	830	4224	35
Sunfire, DLR	0.3–1.4	820	3370	36
Fuel-electrode-supported cell-based stack				
Jülich	0.7	800	2400	37
	1.9	700	2300	
	1.9	750	700	
	0.4–1	800	14 600	
Jülich	1.5	810	2034	31
		810	1001	
Solydera, EIFER	0.5	710	3250	38
			7450	

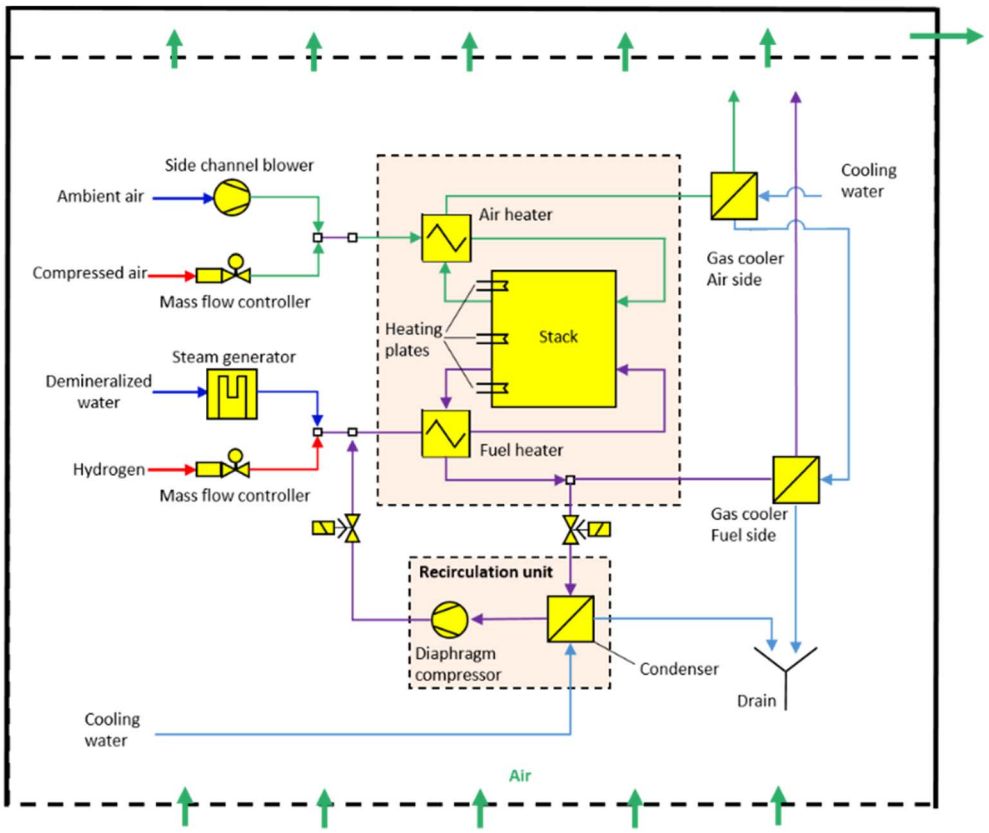

Fig. 2 Flow scheme of a laboratory-scale SOC system at Forschungszentrum Jülich. This work is licensed under the terms of the Creative Commons Attribution 4.0 License © 2021 by the authors (CC BY, (https://creativecommons.org/licenses/by/4.0/)).[25]

chambers in the horizontal plane, seal the cell into the interconnect, and ensure gas-tightness to the outer surrounding of the stacks. They require similar properties to the interconnect, for example, thermal expansion match and mechanical robustness. In addition, they must be gas-tight and show good creep resistance. In long-term operation, sealants can show reactivity with other stack components, for example, interdiffusion, and delamination.[41] The long-term and large-scale deployment of SOEC technology also currently faces the challenge of electrode and electrolyte durability. The state-of-the-art materials of SOECs are adopted from materials used in solid oxide fuel cells. However, since the operating conditions/reaction mechanisms are different for SOFC and SOEC operation modes, the electrode materials requirements also vary depending on the mode of operation. Compared to SOFC operation, different reactions take place at the electrode/electrolyte interfaces, the materials must be stable in different atmospheres/oxygen partial pressures and under different applied voltages. At the moment, the state-of-the-art materials considered from SOFC research exhibit microstructural degradation as a consequence of the different gas compositions and pollutants present in the gas stream.[42,43] For a successful commercial implementation of SOEC technology as part of a future hydrogen infrastructure, the stack costs and the longevity of the system have to be addressed. To meet the industrial goal of a maximum degradation rate of a maximum of 0.75% kh^{-1} or even better 0.5% kh^{-1}, corresponding to a performance loss of 20% in approx. five years, the materials used in current SOEC systems need to be optimized or new innovative materials engineered that exhibit excellent chemical stability and high electrochemical performance in long-term, high-temperature operation.[2]

For the oxygen electrode, new perovskite-based materials such as double perovskites *e.g.*, $Sr_2Fe_{1.5}Mo_{0.5}O_{6-\delta}$ (SFM), $PrBaCo_2O_{5+\delta}$ (PBC) and $GdBaCo_2O_{5+\delta}$ (GBC) as well as Ruddlesden–Popper phases such as $La_2NiO_{4+\delta}$ (LNO), $Nd_2NiO_{4+\delta}$ (NNO), and $Pr_2NiO_{4+\delta}$ (PNO) are currently under investigation and have already shown sufficient performance in short-term measurements up to ~200 h. Doped perovskite oxides based on $La_{0.2}Sr_{0.8}TiO_{3+\delta}$ (LST), $La_{0.75}Sr_{0.25}Cr_{0.5}Mn_{0.5}O_{3-\delta}$ (LSCM), $La_{0.6}Sr_{0.4}Fe_{0.8}Mn_{0.2}O_{3-\delta}$, (LSFM), or double perovskites system $Sr_2Fe_{1.5}Mo_{0.5}O_{6-\delta}$ (SFM) or $Sr_2FeNbO_{6-\delta}$ (SFN) are investigated as alternative fuel electrode materials.[44]

In this paper, we elaborate on the key challenges in state-of-the-art materials for all essential components, for example, electrodes, interconnects, coatings, sealants, and electrolytes used in commercial SOC stack systems. Novel material classes, their production methods, and the assessment of their potential in terms of real-life use are essential to prolonging the longevity of SOEC stack systems and establishing them within a future hydrogen infrastructure. Special emphasis is placed on the cell materials and the development of the electrode

microstructure from the laboratory scale to current commercial applications.

2. Solid oxide electrolysis cell configurations and designs

There are mainly two different cell configurations used in solid oxide cells: the planar and the tubular type. Both configurations consist of at least three different layers – oxygen electrode, electrolyte, and fuel electrode – as displayed in Fig. 3.

Tubular cells are of interest due to their inherent high mechanical stability, quick start-up capability, easier sealing, and improved thermal cycling ability compared to planar cells, however, their application in SOECs and reversible SOCs (rSOCs) is still in the research and development phase.[45,46] Therefore, laboratory and industrial applications are predominantly focused on planar cells, as these cells achieve higher current densities as well as being easier to manufacture, for example, by tape casting and screen-printing techniques, thus increasing cost-effectiveness. Furthermore, planar cells exhibit a lower internal resistance as well as higher flexibility in gas flow configurations compared to tubular cells. However, challenges in using the planar cell in stack configurations include more complicated sealing requirements and contact issues between interconnects and cells.[45,47–49] Regardless of cell design, each cell requires a thick mechanical support layer, which ensures good handleability during processing and absorbs the stresses that may result from SOC operation. The cell design classification depends on the supportive layer. Industrially manufactured and investigated cell designs are electrolyte-supported cells (ESCs), fuel electrode-supported cells (FESCs), oxygen electrode-supported cells (OESCs), and metal-supported cells (MSCs).[45,50,51]

2.1. Electrolyte-supported cell

Electrolyte-supported cells typically consist of an electrolyte layer with a thickness of 50–250 μm in between a fuel electrode (5–20 μm) and an oxygen electrode (15–80 μm).[50] The advantages of ESCs are their good mechanical robustness and better redox behavior compared to electrode-supported cells.[52–54] ESCs for high-temperature electrolysis are currently produced on an industrial scale and sold by, for example, Kerafol, while also being operated in SOEC stacks by Sunfire[55] or Bloom Energy. However, they exhibit high ohmic resistances due to the relatively thick electrolyte layer of partially stabilized zirconia, which shows higher strength but lower oxygen-ion conductivity, leading to lower power densities and thus requiring operating temperatures above 800 °C. These high operating temperatures require good thermal insulation and expensive thermostable materials.[47,53,56]

2.2. Electrode-supported cell

In electrode-supported cells, a thick, porous electrode layer offers mechanical support. As a cell consists of two different electrodes, a distinction can be made between two types of electrode-supported cells: fuel electrode-supported cells

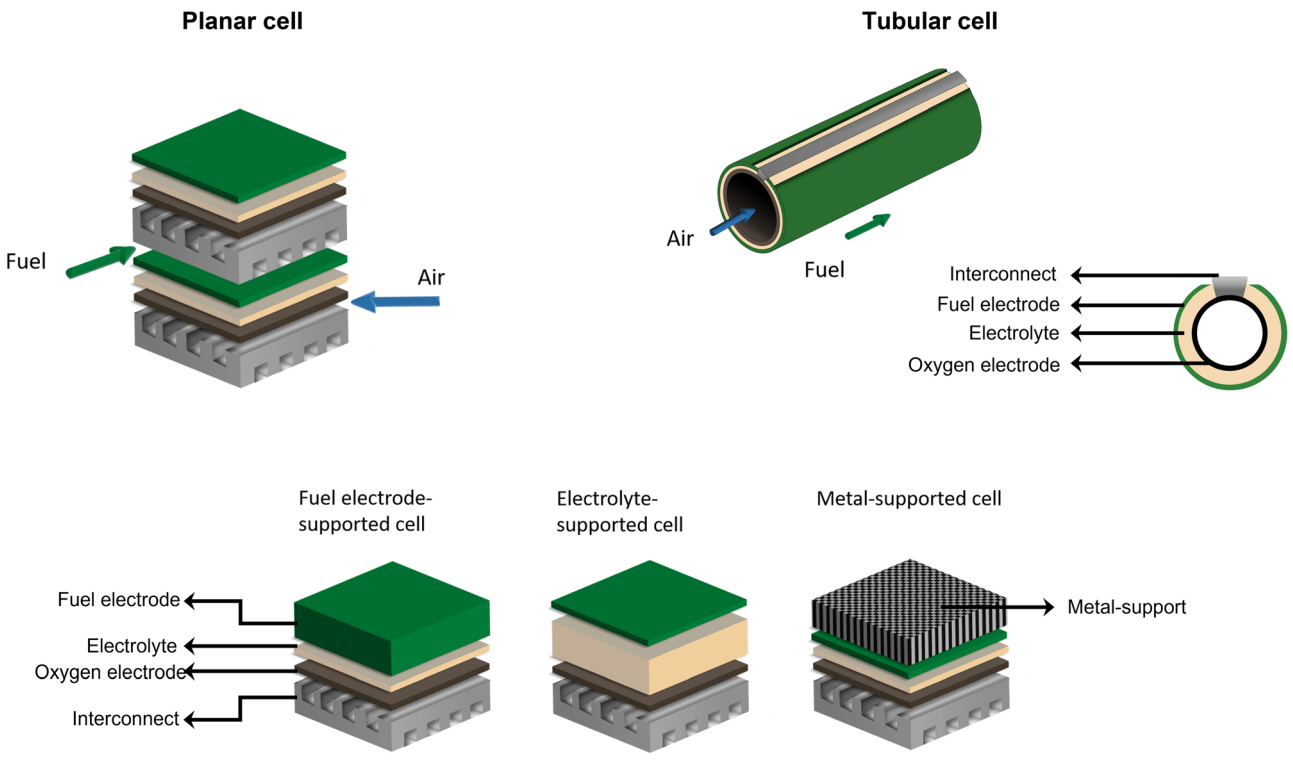

Fig. 3 Planar and tubular cell designs and schematic representation of the three different cell support types reported in the literature: (fuel-) electrode-supported cells, electrolyte-supported cells, and metal-supported cells.

(FESCs) and oxygen electrode-supported cells (OESCs). Here, the electrolyte layer can be significantly thinner (2–20 μm), whereas the supporting layer is 250–1000 μm for FESCs and ~1 mm for OESCs.[50] However, the thickness of the active electrode layers is 5–20 μm for the fuel electrode and 15–80 μm for the oxygen electrode.[50] The reduced thickness of the electrolyte in this cell design leads to a decrease in ohmic resistance and the option of lowering the operating temperatures. When comparing FESCs and OESCs, the fuel electrode-supported cells are more favorable due to their higher power densities, especially at lower temperatures, which is why they are mainly used at present.[45,47,50] Nevertheless, electrode-supported SOCs exhibit higher electronic resistance and low redox stability, resulting in higher sensitivity for damage caused by redox cycling.[53,54,56] At present, fuel electrode-supported cells are key components in Elcogen SOEC stacks as well as in SolydEra solid oxide electrolysis (SOE) systems.[57]

2.3. Metal-supported cell

Another possibility for mechanically stabilizing an SOC is the application of metal support. In this design, the electrolyte thickness and the active fuel and oxygen electrode thicknesses correspond to those of electrode-supported cells. The metallic support has a thickness of ~1 mm.[50] Literature reports indicate that MSCs can overcome many of the above-mentioned restrictions for ESCs, FESCs, and OESCs. They exhibit high mechanical robustness, fast start-up times, and high redox tolerance. A further advantage of metal-supported cells is their low material costs thanks to the minimization of the thickness of the expensive, electrochemically active ceramic layers, for example.[51,58–62] MSCs can also operate at medium-to-low temperatures (of around 650 °C) in 50% H_2O + 50% H_2 with a 20% lower area-specific resistance (ASR) and a significantly lower degradation rate compared to state-of-the-art Ni-YSZ fuel electrode-supported cells.[58] One major drawback of MSCs might be their complex operating conditions, for example, the differences in the TECs between the metal and ceramic components.[51,56,60,63] As MSCs are currently being used successfully in the SOFC systems of Ceres Power, SOEC systems are now being developed.[64] However, there is a lack of publications on the long-term operation of MSC-based stacks in both fuel cell and electrolysis mode.

3. Solid oxid electrolysis cell components

3.1. Electrolytes

3.1.1. Requirements. The electrolyte separates the fuel and oxygen electrode in a solid oxide electrolysis cell and must therefore be stable in both reducing and oxidizing conditions. The gas-tightness of the thin and dense electrolyte layer prevents the reactants on both sides from mixing. The material should possess high oxide ion conductivity (>0.1 S cm^{-1})[65] at operating temperature with negligible electric conductivity to avoid current leakage. The performance of the electrolytes predominantly depends on temperature, material properties, and thickness. High operating temperatures increase the ionic conductivity of the materials and promote thermally activated electrochemical processes. For electrolyte-supported cells, the electrolyte material governs the thermal expansion of the full multi-layer cell, thus preventing delamination of other layers, such as the electrodes, caused by a thermal expansion mismatch.[66,67]

3.1.2. Zirconia- and ceria-based electrolytes. In high-temperature SOCs, the extensively used electrolyte is composed of yttrium-stabilized zirconium (YSZ) oxide, which has good oxygen ionic conductivity between 700 °C and 900 °C. Below 700 °C, 8 mol% yttria-stabilized zirconia (8YSZ) exhibits sufficient performance if the electrolyte layer is thin enough (~3 μm) and the grain size is around 0.6 μm.[68] Direct substitution with 8–10 mol% yttria stabilizes the cubic fluorite structure of ZrO_2, which exhibits numerous vacant octahedral interstitial sites. In addition, large concentrations of oxygen vacancies are created through charge balance. This improves the ionic conductivity of ZrO_2 and results in an extended oxygen partial pressure range of ionic conduction, making stabilized zirconia a suitable and most commonly used electrolyte for high-temperature electrolysis.[69] The dopant valence, the ion size of the dopant, and the dopant concentration in ZrO_2 influence ionic conductivity.[70] Higher doping concentrations have led to immobile defect clusters, thus reducing conductivity. In some industrial solid oxide stack applications,[71–73] mostly ESC-based stacks, 3 mol% YSZ (3YSZ) is employed due to its better fracture toughness (~10 MPa $m^{0.5}$) and high flexural strength (~1 GPa) despite its lower conductivity at high temperatures ($T > 550$ °C).[74] The 8 mol% YSZ has shown the highest conductivity of 0.14 S cm^{-1} at 1000 °C, but a higher conductivity of 0.3 S cm^{-1} at 1000 °C was achieved for ZrO_2 with 11 mol% Sc_2O_3.[70,75] However, the structure becomes rhombohedral over 9 mol% Sc[76] and the conductivity decreases below 600 °C. This is due to the similar ionic radii of Sc^{3+} and Zr^{4+}, resulting in a compact structure with small structural defects.

Doped ceria is a fluorite-type material with a higher ionic conductivity than stabilized zirconia at medium temperatures between 600 °C and 800 °C (Fig. 4). The ionic conductivity reaches its maximum with around 15 mol% of dopant.[77] A widely used dopant is Gd, while Sm and Y have also been used to a lesser extent.[67,68] A major disadvantage of doped ceria electrolytes is the observed reducibility of Ce^{4+} to Ce^{3+} in a reducing environment, resulting in possible mechanical instability and electrical conductivity.[66,78]

In addition to its physical characteristics, 8YSZ is still the material of choice due to its cost advantages over scandia-stabilized zirconia (ScSZ) and gadolinium-doped ceria (GDC). Fuel electrode-supported cells with an 8YSZ electrolyte have proven their long-term stability in various tests conducted at Forschungszentrum Jülich,[25,37,79,80] Topsoe,[81,82] EPFL,[38] CEA,[83–85] DTU,[86] DLR,[87,88] and EIFER.[89]

3.1.3. Alternative electrolyte materials: apatites and lanthanum gallates. One way to increase the longevity of SOEC systems is to operate them at more moderate temperatures, thus slowing down the detrimental thermally activated degradation processes. Lanthanum apatites $La_8B_2Si_6O_{26}$ (B = Mg, Ca,

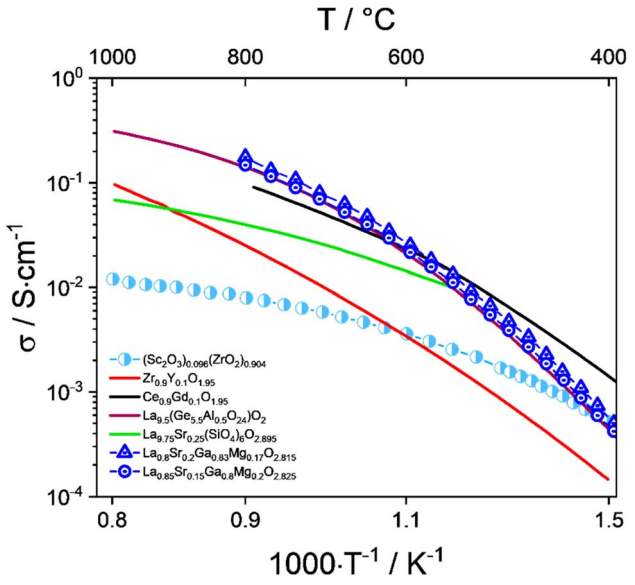

Fig. 4 Total conductivity of oxide ion electrolyte materials (Sc_2O_3)$_{0.096}$(ZrO_2)$_{0.904}$,[104] $Zr_{0.9}Y_{0.1}O_{1.95}$ (YSZ),[105] $La_{9.75}Sr_{0.25}(SiO_4)_6O_{2.895}$ (Si-apatite),[98] $La_{9.5}(Ge_{5.5}Al_{0.5}O_{24})O_2$ (Ge-apatite),[106] $Ce_{0.9}Gd_{0.1}O_{1.95}$ (GDC),[107] $La_{0.8}Sr_{0.2}Ga_{0.83}Mg_{0.17}O_{2.815}$, and $La_{0.85}Sr_{0.15}Ga_{0.8}Mg_{0.2}O_{2.825}$ (LSGM).[108]

Sr, Ba) are a promising alternative, as they exhibit higher conductivity than YSZ and GDC at intermediate temperatures.[90,91] The oxygen interstitials migrate in the conduction channels along the *c*-axis.[90] Lanthanum silicate-based apatites crystallize in a hexagonal structure ($P6_3/m$) and have been reported to exhibit higher oxide ion conductivity at intermediate temperatures than YSZ ($La_{10-x}Si_6O_{26+\delta}$ > 10^{-3} S cm^{-1} at 500 °C).[92–96] The oxide ion conductivity can be optimized by cation doping at both the La and B sites.[97,98] Despite the advantageous material properties, apatites require high preparation temperatures (>1600 °C).[99] One widely studied perovskite-structured oxide is doped lanthanum gallate. Studies have shown the best ionic conductivities for $La_{0.8}Sr_{0.2}Ga_{0.8}Mg_{0.2}O_3$ and $La_{0.8}Sr_{0.2}Ga_{0.85}Mg_{0.15}O_3$ (LSGM)[100] exceeding the ionic conductivity of YSZ over a wide range of oxygen partial pressure.[101] However, under a reducing atmosphere, gallium evaporation was observed.[102,103]

3.1.4. Summary of electrolyte materials. Stabilized zirconia remains a state-of-the-art electrolyte material in electrolyte- and fuel-electrode-supported cells (ESCs, FESCs). In ESCs, partially stabilized (3YSZ) zirconia or scandia-ceria-stabilized zirconia (ScCeSZ) are typically used due to their higher mechanical stability compared to 8YSZ. In FESCs, 8YSZ is the material of choice as it is mechanically supported by a thick support layer on the fuel electrode side. In metal-supported cells (MSCs), GDC is most commonly used as its operating temperature is typically lower than that of ESCs and FESCs (~600 °C). This is due to the enhanced corrosion of the metal support at higher temperatures. If a GDC electrolyte is used, an additional very thin YSZ electron blocking layer must be applied (*e.g.*, by vapor deposition or electrophoretic deposition) to suppress electron leakage.[109] Alternative electrolyte materials are still in the research and development phase, including the first single-cell tests.

3.2. Oxygen electrode

3.2.1. Requirements. Solid oxide cells (SOCs) can be operated reversibly, as solid oxide fuel cells (SOFCs) for power generation from chemical fuels or as solid oxide electrolyzer cells (SOECs) using electricity for the production of chemical fuels. As discussed previously, higher degradation rates have been observed for SOEC compared to SOFC operation. With regards to the oxygen electrode, the origin of degradation processes has been related to the different oxygen activity in the electrode and varied catalytic activity for the oxygen evolution reaction (OER) in SOEC and the oxygen reduction reaction (ORR) in SOFC mode.[110] For the electrolysis reaction, a larger pO_2 gradient across the electrode/electrolyte interface has been suggested, which enhances degradation processes such as the formation of oxygen bubbles at the electrode/electrolyte interface and subsequent delamination or microstructural changes at the electrolyte/oxygen electrode interface. Due to the larger pO_2 gradient, the oxygen electrode material requirements for solid oxide electrolysis cells (SOECs) should meet several criteria, such as excellent catalytic activity for the oxygen evolution reaction (OER) and high chemical stability in an oxidizing environment without the formation of resistive phases with the electrolyte. The thermomechanical properties of the material should be similar to those of the electrolyte to avoid stresses upon heating or cooling, and high electrical conductivity is essential for long-term industrial applications.

The electrode material catalyzes the dissociated oxygen anions to oxygen molecules and surplus electrons (Fig. 5). The mechanism of oxygen evolution at the oxygen electrode includes several steps: ion transfer along the electrode/electrolyte interface, charge transfer, solid-state bulk, surface diffusion, surface desorption, and gas diffusion processes. Among them, bulk transport and surface transport are generally considered to be rate-limiting steps.[111] The catalytic activity and usability of an oxygen electrode material are determined by the surface exchange coefficient (k^*) and the oxygen self-diffusion coefficient (D^*). Adler, Lane and Steele[112] proposed the ALS model in 1996 to calculate the chemical reaction contribution R_{chem} of oxide ion migration in the porous electrode in relation to the oxygen self-diffusion coefficient (D^*, cm^2 s^{-1}), the surface exchange coefficient (k^*, cm s^{-1}), and microstructural parameters such as tortuosity τ, fractional porosity ε, and oxygen surface concentration C_o. Taking the charge transfer resistance into account, they expressed the total impedance according to eqn (5) as the sum of chemical impedance derived from the oxygen evolution reaction (OER) and diffusion at the oxygen electrode (z_{chem}), the electrolyte resistance ($R_{electrolyte}$), and the electrochemical kinetics at the electrolyte/electrode interface ($z_{interface}$). Their models showed that when the surface exchange and solid-state diffusion dominate, the total cell impedance would be reduced to $Z = R_{chem}$.

$$Z = R_{electrolyte} + z_{interface} + z_{chem} \quad (5)$$

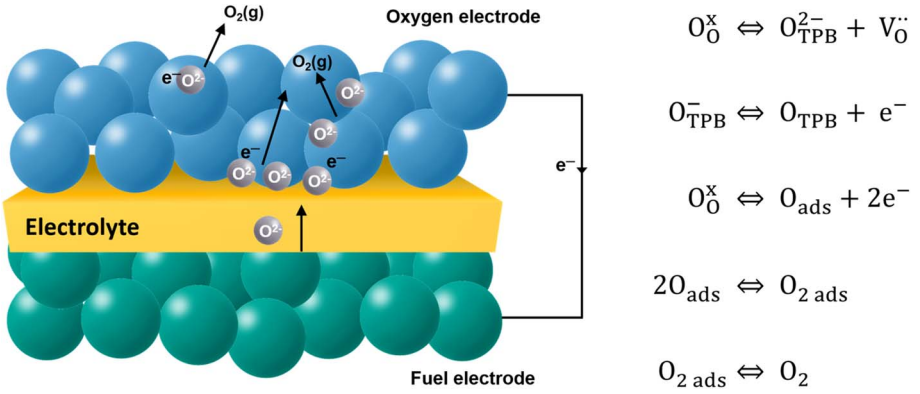

Fig. 5 Schematic description of the oxygen evolution reaction (OER) at the oxygen electrode surface.

$$R_{chem} = \frac{RT}{2F^2}\sqrt{\frac{\tau}{(1-\varepsilon)aC_o^2k^*D^*}} \quad (6)$$

High surface exchange coefficients (k^* ~10^{-7} cm s^{-1} at 700 °C) and a high oxygen diffusion coefficient (D^* ~10^{-7} to 10^{-8} cm^2 s^{-1} at 700 °C) are prerequisites for enhanced oxygen transport and oxygen electrode kinetics in addition to sufficient electrode porosity.[113] The diffusion and surface exchange properties of the oxygen electrode material are a good measure for the catalytic activity of the oxygen electrode and are therefore investigated by oxygen isotope exchange measurements.

The oxygen electrode material should be compatible with the other cell component materials and possess high chemical stability. The thermal expansion coefficient (TEC) gives the relative expansion with temperature, and a mismatch between the electrode material and electrolyte could pose the risk of delamination. The typical value for common electrolyte materials such as yttrium-stabilized zirconia (YSZ), gadolinium-doped ceria (GDC), strontium, and magnesium-doped lanthanum gallium oxide (LSGM) is around 10–13 × 10^{-6} K^{-1}.[114] A similar or adapted thermal expansion for the electrode thus avoids thermo-mechanical stress and ensures long-term system operation. The thermal expansion coefficient depends on the crystal structure as well as the perovskite cation radii.[115] One way of tailoring the TEC is to dope the perovskite material at the A- or B-site. However, this substitution also affects the electrochemical properties of the material.[116] It should be noted that the prerequisite of adapted TECs is based on theory, for example, FESCs with an LSC (*cf.* chapter 3.2.1.1) oxygen electrode, which has a very high TEC (20.5 × 10^{-6} K^{-1}), are being used by Elcogen®, for instance. They do not show any delamination or other mechanical problems during normal operation and even during thermal cycles.[117] High chemical stability under different long-term operating atmospheres is necessary to prevent degradation, which affects efficient oxygen evolution, shortens the lifetime of the cell, and therefore increases costs. High electronic and oxide ion conductivity under an oxidizing atmosphere of over 100 S cm^{-2} and 10^{-3} S cm^{-2}, respectively, ensure good oxygen ion transport through the electrode as well as a high conversion rate per area, resulting in low ohmic cell resistance.[118]

Electrode materials are assigned as either n- or p-type conductors. For the n-type conductor, an oxygen deficiency is required to create electrons, which is why these materials are not stable under oxidizing conditions like ambient air. P-type electronic conductors, on the other hand, are stable in air, as they require oxygen excess to generate holes.[119,120] Mixed ionic–electronic conducting (MIEC) single-phase perovskite oxides have increasingly become a field of study due to their advantageous material properties such as faster oxygen diffusion with improved surface exchange kinetics. Due to their improved performance under varied atmospheres and high potential chemical stability, double perovskites with ordering on A- as well as B-sites are a topic of high interest. Ruddlesden–Popper phases have shown conductivities below the targeted 100 S cm^{-1}, but their thermal expansion coefficient matches closely to state-of-the-art electrolytes.

Electrode microstructure plays an important role in the performance of solid oxide fuel and electrolysis cells, as it determines the reactive surface sites. The most important parameters include grain size, grain size distribution, porosity ε, tortuosity τ, and electrode thickness ("active penetration depth") d. The penetration depth stands for the distance at the electrode/electrolyte interface, in which the electrode is impacted by polarization by the applied potential and takes part in the oxygen evolution reaction. Beyond this distance, the electrode remains in equilibrium with the gas phase. According to Adler, the penetration depth for an MIEC electrode is described by the following equation, where L_c is the characteristic thickness and α the volume-specific surface area of the electrode:[112,121]

$$d = \sqrt{\frac{(1-\varepsilon)}{\tau}} \times \frac{L_c}{\alpha} \quad (7)$$

The grain size and the grain size distribution affect grain growth in the sintering process, thus directly influencing electrode performance. The loss of performance can result from microstructural densification (grain size too big) and unpercolated grain particles (grain size too small). The optimization of tortuosity and porosity is aimed at an ideal gas distribution/conversion at the interface between the gas phase, the

electron-conducting electrode, and the ion-conducting electrolyte referred to as the triple-phase (TPB) or double-phase boundary (DPB in the case of MIECs) sites of the electrode.

3.2.2. Electrode materials

3.2.2.1. Simple ABO_3 perovskites. Noble metals such as platinum have previously been selected for the oxygen electrode. However, perovskite materials made of earth-abundant materials are of greater interest due to their better cost-effectiveness and higher compatibility with the electrolyte.[123,124] Interest in perovskite materials for high-temperature solid oxide electrolysis cells (SOECs) has continuously increased over the last few decades due to their advantageous properties such as high chemical stability, high conductivity including mixed conductivity, excellent catalytic activity for OER, and good cost-effectiveness. The ideal simple perovskite structure has an ABO_3 stoichiometry, as shown in Fig. 6a for the example of $SrTiO_3$. The A-site cations located at the corners of the cubes are coordinated by twelve oxygen ions, while the smaller B-cations are coordinated octahedrally and sit in the cubic center. The A-site cation is commonly characterized by a rare-earth, alkaline, or alkaline-earth ion of low charge and is, therefore, larger than the B-site cation represented by transition metals. Perovskites can exhibit a wide range of physical properties such as ionic conductivity or ferromagnetism, which are influenced by their structure.

Lanthanum manganite ($LaMnO_3$) and lanthanum strontium manganite ($La_{1-x}Sr_xMnO_{3-\delta}$) crystallize in the simple perovskite structure ABO_3 and have attracted widespread research interest due to their high perovskite stability, which improves with increasing A-site cation radii. The partial substitution of the rare-earth cation La^{3+} with the divalent Sr^{2+} introduces p-type conductivity due to the principle of electroneutrality: when La^{3+} is exchanged for Sr^{2+}, an electric hole is formed on the B-site cation.

$$LaMnO_3 \xrightarrow{x\mathrm{SrO}} La^{3+}_{1-x}Sr^{2+}_{x}Mn^{3+}_{1-x}Mn^{4+}_{x}O_3 \quad (8)$$

Electronic conductivity increases with an increase in x and a maximum electronic conductivity of 200–490 S cm^{-1} was obtained for $x = 0.5$ at 1000 °C.[125] The investigation of the oxygen diffusion coefficient and oxygen surface exchange coefficient of Sr-doped $LaMnO_3$ by SIMS technique showed that D^* increases slightly with increased A-site doping from 4.8×10^{-12} cm^2 s^{-1} for $La_{0.9}Sr_{0.1}MnO_{3-\delta}$ to 1.3×10^{-11} cm^2 s^{-1} measured for the composition $La_{0.8}Sr_{0.2}MnO_{3-\delta}$, as this provided further oxygen vacancies.[126,127] In the case of electronic conductors, the reaction sites are located at the interface between the electrode, the electrolyte, and the gaseous phase. To enhance the electrochemically active area, composite LSM-YSZ oxygen electrodes were fabricated.[128,129] The combination of ionic conducting YSZ and LSM as an oxygen electrode is applicable through careful tailoring of the stoichiometry of LSM and choosing appropriate sintering conditions of the composite on YSZ. The sintering temperature should ensure good adhesion and no chemical interaction. The combination of the ion-conducting YSZ phase with the p-type electronic-conducting LSM phase results in substantially enhanced electrocatalytic activity for the composite oxygen electrode due to an extended triple-phase boundary (TPB) and enhanced stability. The electrochemical performance can be enhanced by varying the LSM/YSZ ratio[130] as well as the microstructure.[131] The microstructure is an essential factor for the performance of composite electrodes, as micro-sized particles cause TPB length loss and negatively impact cell performance. Different preparation techniques were

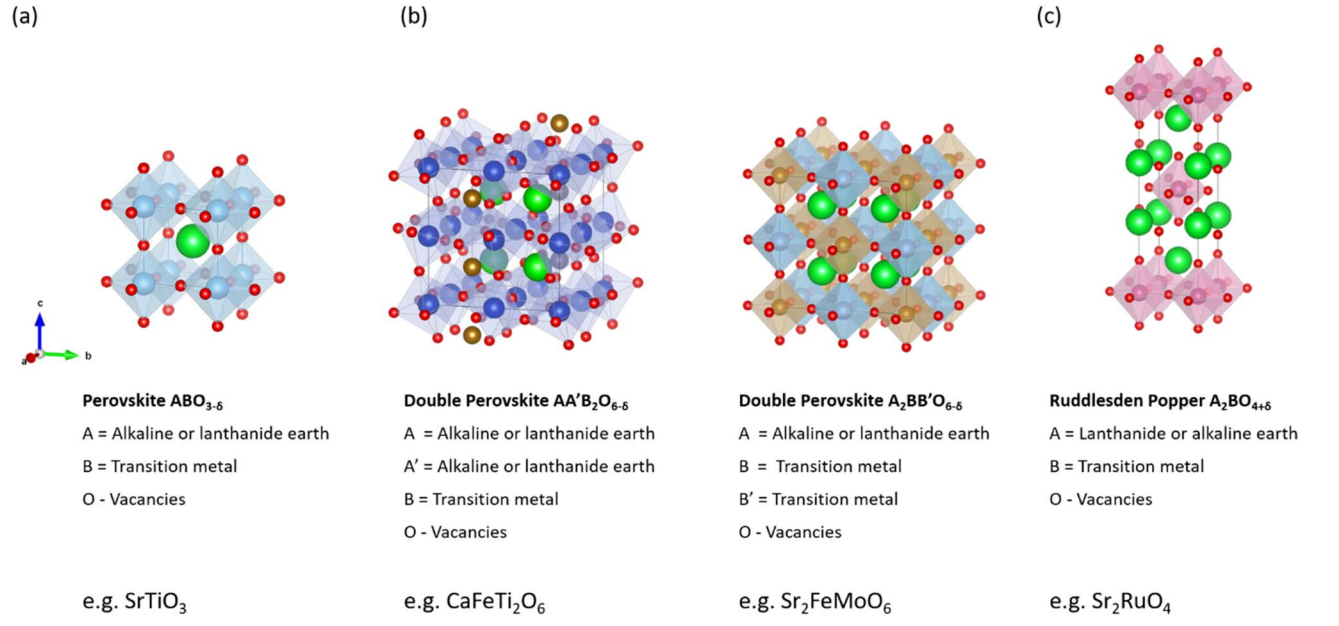

Fig. 6 Crystal structure of cathode materials for (a) simple $SrTiO_3$ perovskite, (b) double $CaFeTi_2O_6$/Sr_2FeMoO_6 perovskites, and (c) Ruddlesden–Popper structure Sr_2RuO_4. Crystal structures produced with VESTA©.[122]

therefore employed to synthesize ultrafine nano-sized particles. In addition to the fast solid-state reaction, smaller nanoparticles were targeted by preparation with the combustion method,[128] the hydrothermal method,[132] spray pyrolysis,[129] and sol–gel synthesis.[133] Although nanostructuring of the LSM enhances initial performance, high operating temperatures are necessary due to the relatively poor catalysis of the LSM/YSZ mixture. This, in turn, quickly changes the nanostructuring to a micro-sized structure and again decreases the performance. Similar to LSM electrodes, the catalytic activity of the LSM-YSZ composite is enhanced by the application of cathodic polarization but the enhanced performance is lost under SOEC conditions.[134] Despite the high electrical conductivity, which made pure LSM a conventional oxygen electrode material in solid oxide cell applications as early as the 1980s and 1990s, the low ionic conductivity and catalytic activity have shifted research to other perovskite materials with mixed ionic and electronic conducting (MIEC) properties.

Cobalt-based lanthanum strontium oxide ($La_{1-x}Sr_xCoO_{3-\delta}$ (LSC)) and lanthanum strontium ferrite oxide ($La_{1-x}Sr_xCo_{1-y}Fe_yO_{3-\delta}$ (LSCF)) are the current state-of-the-art oxygen electrode materials with MIEC properties that have found widespread interest due to their higher catalytic activity as well as their high ionic and electronic conductivity. In contrast to purely electronic conducting (EC) materials such as LSM, the reaction zone, *i.e.*, the TPB where gas phase, electronic, and ionic conductor meet, is extended to the two-dimensional double-phase boundary (DPB) at the mixed ionic/electronic conductor interface with the gas phase. Compared to LSM, Co-based perovskite electrodes have shown higher structural and performance stability under long-term SOEC operation conditions.[135] However, the materials exhibit higher thermal expansion coefficients (TECs) of up to around 20.5 × 10^{-6} K^{-1} (30–1000 °C),[136] which is higher than TEC values of common electrolyte materials (Table 5). One strategy for lowering the TEC value is to substitute the rare-earth cation La^{3+} (*e.g.*, $La_{0.4}Sr_{0.6}Co_{0.8}Fe_{0.2}O_{3-\delta}$, 21.4 × 10^{-6} K^{-1}, 25–1000 °C)[137] with the smaller Pr^{3+} ($Pr_{0.4}Sr_{0.6}Co_{0.8}Fe_{0.2}O_{3-\delta}$, 20.6 × 10^{-6} K^{-1}, 25–1000 °C) or Gd^{3+} ($Gd_{0.4}Sr_{0.6}Co_{0.8}Fe_{0.2}O_{3-\delta}$, 17.6 × 10^{-6} K^{-1}, 25–1000 °C).[137] With the substitution of Fe ions for Co, the TEC also decreases.[138] LSCF has a high electronic and ionic conductivity (280 S cm^{-1} and 8.0 × 10^{-3} S cm^{-1} at 800 °C) in addition to high oxygen diffusion properties, for example, oxygen self-diffusion coefficient D^* (5.00 × 10^{-7} cm^2 s^{-1}, 800 °C) and oxygen surface exchange k^* (6.00 × 10^{-6} cm^2 s^{-1}, 800 °C). This is much higher than that of LSM, as shown in Table 3. The electrical and ionic conductivities of LSC surpass LSCF and LSM with an electrical and ionic conductivity of 1585 S cm^{-1} and 0.22 S cm^{-1}, respectively at 800 °C. The ionic conductivity σ_i in LSCF depends on the substitution of Co with Fe, with the conductivity decreasing with a higher Fe content. The ionic conductivity σ_i for $La_{0.8}Sr_{0.2}Co_{0.8}Fe_{0.2}O_{3-\delta}$ (4.0 × 10^{-2} S cm^{-1}, 800 °C) is, therefore, one order of magnitude higher than for $La_{0.8}Sr_{0.2}Co_{0.2}Fe_{0.8}O_{3-\delta}$ (2.3 × 10^{-3} S cm^{-1}, 800 °C).[138] Higher Sr and Co contents have shown higher oxygen permeability and an increase in oxide ion mobility D^*, which was linked to the smaller oxygen ion binding energy of Co and the increased oxygen vacancy concentration as a result of the substitution of La with Sr.[139] The lowest polarization resistance (R_P) value obtained for $La_{0.6}Sr_{0.4}Co_{1.05}O_{3-\delta}$ (LSC) is 62 mΩ cm^2 at 600 °C. Depending on the sintering temperature, LSCF electrodes show resistances of 2.7–4.0 Ω cm^2.[140] Despite the advantageous oxygen diffusion properties and conductivities for state-of-the-art LSC and LSCF electrode materials, layered perovskites have attracted increased interest as an alternative oxygen electrode material.

3.2.2.2. Double perovskites. Double perovskite compounds are derived from half-substituted B′-site cation places with B″ cations, for example, resulting in the structure A_2 B′B″X_6 with alternatively arranged B′O_6 and B″O_6 octahedra (Fig. 6b). In these perovskites, two different transition metal (TM) cations can be found at the B-site, which govern physicochemical material properties such as electrical conductivity and oxygen binding energy, thus offering higher flexibility compared to ABO_3-structured perovskites.

The introduction of two different B-site cations can lead to disordered as well as ordered A_2 B′B″X_6 double perovskites. The key factor in determining the probability of ordering is the

Table 3 Thermal expansion coefficient (TEC), electronic (σ_e) and ionic (σ_i) conductivities in air, the oxygen self-diffusion coefficient D^*, and the surface exchange coefficient k^* for different ABO_3 perovskite materials

Composition	TEC/10^{-6} K^{-1}	σ_e/S cm^{-1}	σ_i/S cm^{-1}	D^*/cm^2 s^{-1}	k^*/cm s^{-1}	Ref.
$La_{0.8}Sr_{0.2}MnO_{3-\delta}$	11.62 (100–900 °C)	200–300 (900 °C)	5.93 × 10^{-7} (1000 °C)	4.0 × 10^{-15} (800 °C)	5.62 × 10^{-9} (800 °C)	127 and 141–144
	13.13 (900 °C)	152 (800 °C)	4.0 × 10^{-8} (900 °C)	1.0 × 10^{-16} (700 °C)	1.39 × 10^{-10} (700 °C)	145–149
$La_{0.6}Sr_{0.4}CoO_{3-\delta}$	20.5 (30–1000 °C)	1585 (800 °C)	0.22 (800 °C)	2.86 × 10^{-9} (600 °C)	9.09 × 10^{-8} (600 °C)	136, 138 and 150
		1595 (800 °C)	0.37 (832 °C)	8.45 × 10^{-10} (600 °C)	7.33 × 10^{-7} (600 °C)	136, 151 and 152
$La_{0.6}Sr_{0.4}Co_{0.2}Fe_{0.8}O_{3-\delta}$	17.5 (30–1000 °C)	210 (900 °C)	8.0 × 10^{-3} (800 °C)	5.00 × 10^{-7} (800 °C)	6.00 × 10^{-6} (800 °C)	136, 138, 144 and 153
	15.3 (100–600 °C)	280 (800 °C)	1.0 × 10^{-2} (1000 °C)	3.3 × 10^{-9} (700 °C)	1.5 × 10^{-6} (700 °C)	136, 138 and 154–156

oxidation state difference between the B′ and B″ cations. In addition to the B-site cations, the order degree depends on the size of the A cation and decreases with an increasing A cation radius.[157]

The Mo-doped $SrFeO_{3-\delta}$ is an MIEC perovskite oxide that has shown high sensitivity of the B-site cation order on physical properties such as electrical conductivity.[158–160] Oxygen defect formation, electrical properties, and catalytic activity are influenced by the incorporation of the high-valence Mo ions, which influence the oxidation state of iron in the perovskite. With increasing Mo dopant concentration in the brownmillerite structure $SrFeO_{3-\delta}$ under an oxidizing atmosphere, the activation energy for oxygen transport decreases.[161,162] At higher Mo doping ($0.5 \leq x \leq 1.5$), the structure crystallizes as a double perovskite $Sr_2Fe_{2-x}Mo_xO_{6-\delta}$.[163–165] The ferromagnetic perovskite $Sr_2Fe_1Mo_1O_{6-\delta}$, therefore, finds no widespread use as an oxygen electrode. It can only be synthesized under reducing conditions due to the lack of Mo solubility under oxidizing conditions, resulting in a large detectable $SrMoO_4$ phase.[166,167]

The $Sr_2Fe_{1.5}Mo_{0.5}O_{6-\delta}$ double perovskite phase, however, has attracted interest due to its high ionic conductivity of 0.13 S cm^{-1} in air (800 °C).[168] This is significantly higher than for current state-of-the-art materials such as $La_{0.6}Sr_{0.4}Co_{0.2}Fe_{0.8}O_3$ (8.0×10^{-3} S cm^{-1}, 800 °C)[138] and is comparable to the high-performance oxygen electrode material $La_{0.6}Sr_{0.4}CoO_3$ (0.22 S cm^{-1}, 800 °C).[169] In contrast to simple perovskite materials, the p-type conducting material $Sr_2Fe_{1.5}Mo_{0.5}O_{6-\delta}$ exhibits weak Fe–O bonds and upon removal of the neutral oxygen atom, an extra charge delivered to the lattice is fully delocalized, thus forming a high concentration of oxygen vacancies.[170] Values for the total conductivity in air (14.93 S cm^{-1}, 750 °C;[171] 14.5 S cm^{-1}, ~450 °C (ref. 172)) do not compare to state-of-the-art oxygen electrode materials.[173] They display a thermal expansion coefficient value of 18.1×10^{-6} K^{-1} for $Sr_2Fe_{1.5}Mo_{0.5}O_{6-\delta}$, which is lower than for cobaltites but slightly higher than for common electrolyte materials such as 8 mol% yttrium-stabilized zirconia (8YSZ), gadolinium-doped ceria (GDC), and $La_{0.9}Sr_{0.1}Ga_{0.8}Mg_{0.2}O_3$ (LSGM) in the temperature range of 200 °C to 1200 °C.[174] Nevertheless, $Sr_2Fe_{1.5}Mo_{0.5}O_{6-\delta}$ exhibits a higher TEC compared to Mn-based cathodes such as $La_{0.8}Sr_{0.2}MnO_3$ with a TEC of 11.6×10^{-6} K^{-1} in air[141] but can surpass Co-based materials such as $La_{0.6}Sr_{0.4}CoO_3$ (20.5×10^{-6} K^{-1}),[127] which shows a higher value. Similar to other Sr-containing electrode materials, SFM exhibits good chemical compatibility with known electrolyte materials, except for YSZ, with which an insulting secondary phase formation can be observed.[166]

An investigation of the rate-determining steps of oxygen surface exchange showed that in an oxidizing atmosphere, $Sr_2Fe_{1.5}Mo_{0.5}O_{6-\delta}$ exhibits high oxygen conductivity and oxygen diffusion, but is limited by the oxygen incorporation rate.[175] Diffusion coefficient D^* (5.0×10^{-6} cm^2 s^{-1}, 750 °C) and surface exchange coefficient k^* (2.8×10^{-5} cm s^{-1}, 750 °C) for SFM were determined to be in line with the diffusion properties of $La_{0.6}Sr_{0.4}Co_{0.2}Fe_{0.8}O_3$ (LSCF),[176] corresponding to $La_{0.6}Sr_{0.4}MnO_{3+\delta}$.[175] However, these values for the high-performance oxygen electrode material $La_{0.6}Sr_{0.4}CoO_3$ are slightly higher than reported for SFM.[177] The exchange current density of $Sr_2Fe_{1.5}Mo_{0.5}O_{6-\delta}$ in air (0.186 A cm^{-2})[87] is higher than that of LSM (0.003–0.004 A cm^{-2})[177,178] at 800 °C and comparable to the Co-based materials (0.005–0.519 A cm^{-2}).[174,177,178] These results suggest that SFM may have good electrochemical activity for the oxygen evolution reaction. Table 6 provides examples of electrochemical performance for state-of-the-art materials compared to double perovskite materials such as oxygen electrode material in solid oxide electrolysis cells. To improve the performance of $Sr_2Fe_{1.5}Mo_{0.5}O_{6-\delta}$ in air, doped SFM materials and composite electrodes have been investigated using symmetrical SFM cells due to their excellent redox stability.[179] An excessive Cu doping ($x > 0.1$) in $Sr_2Fe_{1.5-x}Cu_xMo_{0.5}O_{6-\delta}$ (SFCM) resulted in the expansion of the unit cell, which had a detrimental effect on oxygen ion diffusion.[172] The maximum total conductivity of 49.3 S cm^{-1} at 450 °C was observed for 10% mol Cu due to a high electric charge carrier concentration (electron holes). With decreased Cu doping ($x < 0.1$), the oxygen vacancies increased but could not compensate for the decrease in the electron–hole concentration. $Sr_2Fe_{1.4}Cu_{0.1}Mo_{0.5}O_{6-\delta}$ also showed the best electrochemical performance with an area-specific resistance (ASR) of 0.26 Ω cm^2 compared to undoped SFM (0.63 Ω cm^2) and $Sr_2Fe_{1.2}Cu_{0.3}Mo_{0.5}O_{6-\delta}$ (0.45 Ω cm^2) at 800 °C. The electrochemical characterization of composite electrodes of SFC0.1M with $Sm_{0.2}Ce_{0.8}O_{1.9}$ (SDC) resulted in an ASR of 0.15 Ω cm^2 for the mass ratio of 60 : 40 SFC0.1M to SDC. Measurements in H_2O/CO_2 co-electrolysis with similar composite SFM-SDC/LSGM/SFM-SDC cells showed a lower polarization resistance of 0.48 Ω cm^2 at OCV with an electrolysis current density of −0.73 A cm^{-2} at 850 °C and 1.3 V. The durability test with −120 mA cm^{-2} at 800 °C showed an increased cell voltage of 0.13 mV h^{-1}.[180,181] Symmetrical cells (SFM/GDC/6Yb4ScSZ/GDC/SFM) tested in SOEC (90% H_2O + 10% Ar) and co-SOEC (75% H_2O + 25% CO_2) mode presented a high current density of −1.4 A cm^{-2} and −1.1 A cm^{-2} at 1.3 V.[182] Electrochemical impedance spectroscopy also underlined the high performance with an ASR at −0.5 A cm^{-2} of around 0.31 Ω cm^2 in 90% H_2O + 10% Ar and 0.42 Ω cm^2 in 75% H_2O + 25% CO_2. The durability in H_2O/CO_2 co-electrolysis showed promising short-term performance for 24 h (36 mV) at 900 °C.

Doped double perovskites of the formation $A'A''B_2X_{5+\delta}$, with A′ being a lanthanide cation and A″ an alkaline-earth element such as Sr or Ba exhibit rapid oxygen ion transport. The structural investigation for oxygen-deficient perovskites $LnBaCo_2O_{5+\delta}$[183] derived from the "112"-type $YbaFeCuO_5$ (ref. 184) showed that the Ba and Ln ions order in alternating layers (001). The oxygen content decreased along the lanthanide series with the cell volume ($LaBaCo_2O_{5+\delta}$: $\delta_{oxygen} = 0.806$; $GdBaCo_2O_{5+\delta}$: $\delta_{oxygen} = 0.698$).[185–187] An advantage of layered perovskites is the good oxygen diffusion and surface exchange kinetics at rather low temperatures of around 600 °C ($k^* = 2.8 \times 10^{-7}$ cm s^{-1} and $D^* = 4.8 \times 10^{-10}$ cm^2 s^{-1} at 575 °C (ref. 188)), which is in the same order of magnitude as simple ABO_3-type perovskites[187,189] due to the reduced oxygen bonding strength in the [AO] layer and the formation of crystalline channels for enhanced ion transport. The high ionic conductivity was linked to the mixed

valence state of Co in the presence of divalent cations (Ba^{2+}, Sr^{2+}) with $Co^{2+/3+}$ and $Co^{3+/4+}$ and, therefore, reduced oxygen ion hopping energy.[190]

These layered materials can also significantly display high electronic conductivity[191] that is sufficient for SOEC applications in the range of ~960 S cm^{-1} at 470 °C down to ~500 S cm^{-1} at around 800 °C.[189] However, as with other cobalt-containing perovskites, the A-site cation-ordered perovskites have a high thermal expansion coefficient (24.0×10^{-6} K^{-1} for $PrBaCo_2O_{5+\delta}$ (PBC))[192] that is not in the range of common electrolytes, such as yttrium-doped zirconia (8YSZ, 10.5×10^{-6} K^{-1})[193] and gadolinium-doped ceria (GDC, 12.5×10^{-6} K^{-1}),[193] as listed in Table 5. The secondary alternative electrolyte material, strontium magnesium-doped lanthanum gallate (LSGM, 10.9×10^{-6} K^{-1}),[193] offers a similar comparison. These large differences could lead to thermal stress between the cell components. Enhanced electrode reaction kinetics and improved mechanical compatibility have led to the development of composite electrodes consisting of A-site ordered cobalt-containing perovskites and ceria-based electrolyte materials.

$PrBaCo_2O_{5+\delta}$ is a new, intensely studied material for SOC applications as the electrochemical performance in the $LnBaCo_2O_{5+\delta}$ series increases from La to Pr as an A-site cation (Pr > Gd > Nd > Sm > La).[187] The incorporation of GDC in PBC has an unfavorable effect on electrical conductivity, which decreases with increasing GDC content.[194] However, at a typical SOEC operating temperature of 800 °C, the electrical conductivities are sufficient for application with 360 S cm^{-1}, 456 S cm^{-1}, 569 S cm^{-1}, and 682 S cm^{-1} for $x = 20$ wt%, 20 wt%, 10 wt%, and 0 wt%, respectively. Symmetrical cell measurements in air have shown a lower R_P of 0.86 Ω cm^2 at 600 °C compared to 1.2 Ω cm^2 for $La_{0.6}Sr_{0.4}Co_{0.2}Fe_{0.8}O_{3-\delta}$ (LSCF) under similar conditions.[140,195] Single-cell measurements with a PBC-10 wt% GDC oxygen electrode in a temperature range of 550–850 °C indicate good catalytic activity and improved mechanical stability with the addition of GDC, for example, 0.698 Ω cm^2 and 0.550 Ω cm^2 at 550 °C for PBC and PBC-10 wt% GDC.[194] The A-site cation-deficient $PrBa_xCo_2O_{5+\delta}$ (PB_xCO, $x = 0.90$–1.0)[196] has shown a higher performance than $(La_{0.6}Sr_{0.4})_{1-x}Co_{0.2}Fe_{0.8}O_{3-\delta}$[197] and $(Ba_{0.5}Sr_{0.5})_{1-x}Co_{0.8}Fe_{0.2}O_{3-\delta}$[198] PB_xCO (x = 0.90–1.0) shows increased electrical conductivity (>600 S cm^{-1}) at the desired operating temperatures and a decrease in the thermal expansion coefficient with Ba deficiency.[196] The composition $PrBa_{0.94}Co_2O_{5+\delta}$ exhibits the highest electrocatalytic activity with a low polarization resistance of 42 mΩ cm^2 at 600 °C in addition to a high conductivity of ~935 S cm^{-1} (700 °C). An increase in the content of Ba results in an increased TEC of 17.4×10^{-6} K^{-1} (50–300 °C) for $PrBaCo_2O_{5+\delta}$ and a higher R_P (160 mΩ cm^2) in addition to lower electrical conductivity (~672 S cm^{-1}, 700 °C). Decreasing the Ba doping to $PrBa_{0.90}Co_2O_{5+\delta}$ also results in less electrical conductivity (~876 S cm^{-1}, 700 °C), a higher polarization resistance (86 mΩ cm^2), and a slightly increased TEC (15.2×10^{-6} K^{-1}, 50–300 °C) compared to $PrBa_{0.94}Co_2O_{5+\delta}$.[196] Other oxygen electrode materials, for example the cobalt-free perovskite $SrNb_{0.1}Fe_{0.9}O_{3-\delta}$ (SNF)[199] and the cobalt-containing perovskite $Ba_{0.5}Sr_{0.5}Co_{0.8}Fe_{0.2}O_{3-\delta}$ (BSCF)[200] exhibit higher resistances than $PrBa_{0.4}Co_2O_{5+\delta}$ (390 mΩ cm^2 and 72 mΩ cm^2, respectively). This highlights the potential of $PrBa_{0.4}Co_2O_{5+\delta}$ for application in electrochemical devices.

3.2.2.3. Ruddlesden–Popper nickelates. Despite the high performance and good durability of perovskite-structured materials such as $La_{1-x}Sr_xCoO_{3-\delta}$ or $La_{1-x}Sr_xCo_{1-y}Fe_yO_{3-\delta}$, the search for new materials with a better matching TEC has sparked interest in alternative Ruddlesden–Popper lanthanide nickelates $Ln_2NiO_{4+\delta}$ (Ln = La, Pr or Nd) presented in Fig. 7 and 6c. They show high surface exchange coefficients (k^*) and high anionic bulk diffusion (D^*) with good electrical conductivity (~100 S cm^{-1} (ref. 201)) as well as good thermal expansion properties matching state-of-the-art electrolyte materials (Tables 5 and 7) and cell components such as metallic interconnects.[202–205]

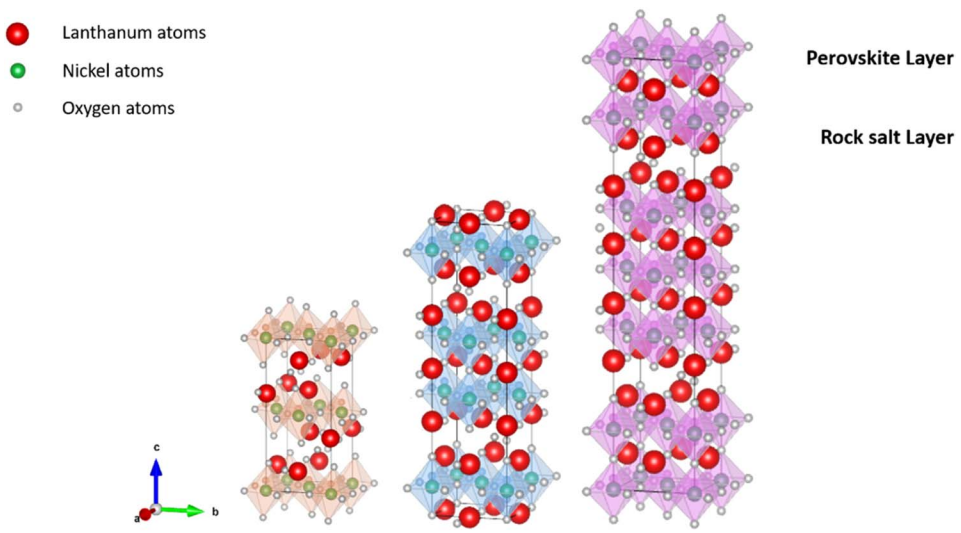

Fig. 7 Schematic representation of La_2NiO_4 ($n = 1$),[206] $La_3Ni_2O_7$ ($n = 2$),[207] and $La_4Ni_3O_{10}$ ($n = 3$),[208] with n-stacked NiO_6 octahedral layers sandwiched between rock-salt LaO layers. Crystal structures produced with VESTA©.[122]

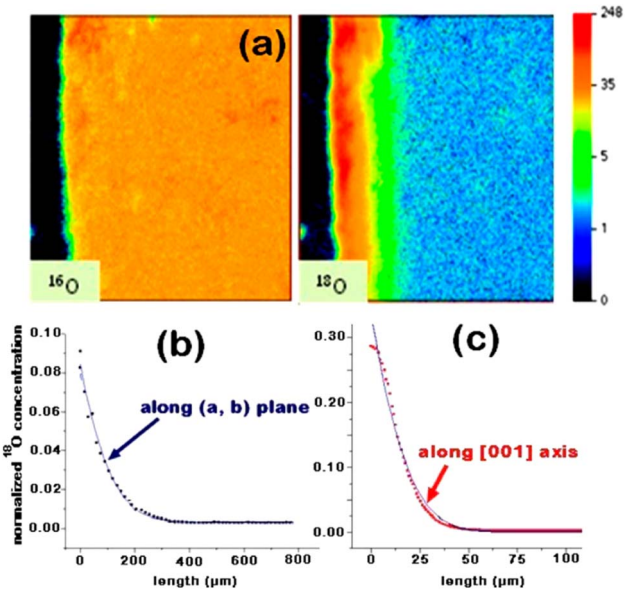

Fig. 8 $Nd_2NiO_{4+\delta}$ crystal exchange experiment at 703 °C for 856 s: (a) surface scanning methods: ^{16}O and ^{18}O SIMS images (along the *c*-axis). (b) Using the line-scanning method, the normalized ^{18}O concentration profile along the (*a*,*b*)-plane was recorded. (c) Normalized ^{18}O concentration profile extract along the *c*-axis (obtained from image in (a)). Reprinted with permission from ref. 214. Copyright 2013 American Chemical Society.

The nickelate structure $Ln_{n+1}Ni_nO_{3n+1}$ ($n = 1$) consists of alternate Ln_2O_2 rock-salt layers and polyhedral NiO_2 square plane layers with interstitial oxygen in the salt layers.[209,210] This material accommodates the oxygen excess in the form of interstitial oxygen in the Ln_2O_2 rock-salt layer, which leads to a mixed-valence of the B-site cation Ni (Ni^{2+}/Ni^{3+}) and, in turn, leads to fast oxygen ion transport.[202,211–213] The oxygen ion mobility in the *ab*-plane is favored and induces anisotropy to the ion conductivity. Any diffusion along the *c*-axis of the structure involves a less favorable diffusion pathway through the occupied oxygen sites in the perovskite blocks. This is highlighted by Fig. 8, which shows ^{16}O and ^{18}O SIMS images (along the *c*-axis, Fig. 8a) obtained using the surface scanning method alongside the normalized ^{18}O concentration profile extract along the (*a*,*b*)-plane in Fig. 8b for $Nd_2NiO_{4+\delta}$. Although the diffusion D_c^* is three orders of magnitude lower than D_{ab}^*, the overall ionic conductivity of the nickelates is compatible with known SOC oxygen electrode materials and higher than those of LSCF at 700 °C (ref. 202 and 214–216) (Fig. 9).

The investigation of diffusion coefficients for different lanthanide nickelates showed higher diffusion along the *ab*-plane and lower activation energy for diffusion for $Pr_2NiO_{4+\delta}$ compared to $Nd_2NiO_{4+\delta}$ (E_a^{Pr} ~0.7 eV and E_a^{Nd} ~1.4 eV). This is in contrast to D_c^*, which is very similar for both materials, with similar activation energies (1.1–1.3 eV) for oxygen diffusion.[214] Of the lower order Ruddlesden–Popper phases, $La_2NiO_{4+\delta}$ (LNO), $Pr_2NiO_{4+\delta}$ (PNO), and $Nd_2NiO_{4+\delta}$ (NNO) have been investigated as the most promising oxygen electrode materials for SOC application.[217–222] The oxygen over stoichiometry ($+\delta$) indicates the ionic conductivity of the lanthanide nickelates and is highly dependent on the rare-earth cation size. Lanthanum nickelate $La_2NiO_{4+\delta}$ (LNO) has a lower amount of oxygen interstitials ($\delta \sim 0.13$)[216] and a larger La^{3+} cation radius (1.16 Å) compared to $Pr_2NiO_{4+\delta}$ (PNO) ($\delta \sim 0.21$)[216] and the smaller ionic radius of Pr^{3+} (1.126 Å). $Nd_2NiO_{4+\delta}$ (NNO) with Nd^{3+} (0.98 Å) was reported to have the highest oxygen diffusion coefficient above 850 °C and an interstitial oxygen amount with $\delta \sim 0.22$.[216,217,223,224] The cation of lanthanide nickelates also influences material properties. PNO shows the highest electrochemical performance, *i.e.*, the lowest polarization resistance (R_P) value, better ionic and electronic conductivity, as well as diffusion properties compared to LNO, especially at intermediate temperatures (600–700 °C).[217,225] In comparison, LNO

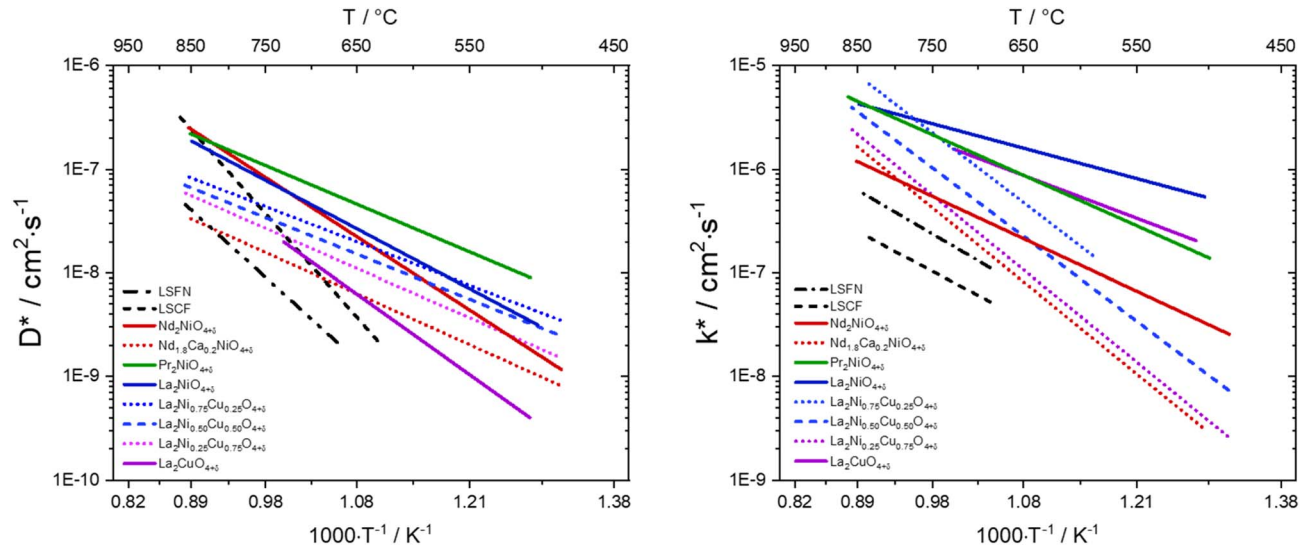

Fig. 9 Diffusion properties of different oxygen electrode materials compared to $La_{0.6}Sr_{0.4}Fe_{0.8}Ni_{0.2}O_{3-\delta}$ (LSFN), $La_{0.6}Sr_{0.4}Fe_{0.8}Co_{0.2}O_{3-\delta}$ (LSFC).[201,216]

exhibits higher chemical stability. At high temperatures of around 800–950 °C, the decomposition of $Pr_2NiO_{4+\delta}$ after 6.5 h into PrO_x and $Pr_4Ni_3O_{4+\delta}$ was reported.[226] In the intermediate temperature range from 600 °C to 800 °C, a decomposition into Pr_6O_{11}, $PrNiO_{3-\delta}$, and $Pr_4Ni_3O_{10+\delta}$ was observed.[227,228] The comparison of polarization values R_P before and after the complete dissociation of PNO as a measure of electrochemical performance showed no change at $i_{dc} = 0$. The second RP nickelate structure ($Ln_3Ni_2O_{7\pm\delta}$) is composed of two NiO_6 layers connected in the *c*-axis between rock-salt layers. $Ln_4Ni_3O_{10\pm\delta}$ ($n = 3$) has a similar structure to three infinite NiO_6 sheets connected between the rock-salt layers. Higher order RP phases have relatively high total conductivity and are oxygen understoichiometric in contrast to the $n = 1$ phases.[229] No Ni^{2+}/Ni^{3+} impurity phase formation for $La_3Ni_2O_{6.95}$ and $La_4Ni_3O_{9.78}$ was reported in contrast to $La_2NiO_{4+\delta}$ and $La_2Ni_{1.9}Co_{0.1}O_{4+\delta}$ at 900 °C after two weeks in air.[229–231] $Pr_4Ni_3O_{10+\delta}$ shows metallic behavior[232] and higher conductivity than $Nd_4Ni_3O_{10+\delta}$ and $La_4Ni_3O_{10+\delta}$. $Pr_4Ni_3O_{10+\delta}$ was shown to be an over-stoichiometric MIEC type under air and oxygen.

Doped lanthanide nickelates were synthesized to improve diffusivity, surface exchange coefficients, conductivity, and electrochemical performance. The substitution of the A-and/or B-site cation can lead to improved electronic and ionic conductivity. Ni is frequently substituted with Co, and La with Sr and Ca. Atomistic simulations predicted that the substitution of Ni^{2+} with Co^{3+} or Fe^{3+} would increase the oxygen interstitial concentration, but also have a detrimental effect on oxygen ion diffusivity.[233] The investigation concerning factors affecting the ionic transport in oxygen-hyperstoichiometric phases with K_2NiF_4-type structures such as the lanthanum nickelates found that the decreasing radii of the A-site rare-earth cation led to a decrease in ionic transport.[212]

Electrochemical studies as to the effect of Co doping on $Pr_2NiO_{4+\delta}$ showed an increase in electrochemical performance and long-term stability of the lanthanide nickelates.[217] Increasing the cobalt content ($x = 0.0$, 0.1, and 0.2) led to an increase in δ, which is one indication for better electrochemical properties and higher diffusivity/ionic conductivity. Symmetrical cell measurements under pO_2 attributed the process resistances to the gas diffusion process and the oxygen surface exchange reaction, *i.e.*, the charge transfer process (surface diffusion of the adsorbed/desorbed oxygen atoms and their consequent reduction/evolution).[217] The charge transfer process was identified as the rate-limiting step among the electrode processes for these PNO and Co-substituted PNO electrodes. An investigation of single cells (NiO-YSZ/YSZ/GDC/electrode, CeramTec®, ASC-10C type) exhibited very high performance for $Pr_2Ni_{0.8}Co_{0.2}O_{4+\delta}$ (PNCO20) with an R_P value of 118 mΩ cm^2 compared to 128 mΩ cm^2 (PNO). Stability tests at 800 °C with −1 A cm^{-2} up to 250 h showed less degradation for cells containing Co-doped nickelates as oxygen electrodes. The degradation of LSCF and PNO cells were similar (~88 mV kh^{-1}), although $Pr_2Ni_{0.9}Co_{0.1}O_{4+\delta}$ (PNCO10) and $Pr_2Ni_{0.8}Co_{0.2}O_{4+\delta}$ (PNCO20) exhibited less than half with 36 mV kh^{-1} and 22 mV kh^{-1}, respectively. $La_2Ni_{0.8}Co_{0.2}O_{4+\delta}$ (LNCO20) showed similar degradation (~30 mV kh^{-1}).[234] Post-test analysis showed no severe damage or delamination/cracks for Co-doped nickelate electrodes, but SEM-EDS revealed the reactivity of GDC and PNO in the form of Ce and Pr interdiffusion at the electrode/electrolyte interface. The investigation of thin PNO and PNCO10 films showed an improved performance of PNO with cobalt substitution due to an enhancement in the diffusion coefficient (D^*) and surface exchange coefficient (k^*).[235] $La_2NiO_{4+\delta}$ shows a relatively lower electrical conductivity of 70–80 S cm^{-1} between 600 °C and 800 °C. For this reason, attempts to substitute the A-site cation with Ca and Sr were conducted. The investigation of Sr-substituted LNO showed higher oxygen diffusivity of $La_{1.9}Sr_{0.1}NiO_{4+\delta}$ than $La_xSr_{1-x}Co_yFe_{1-y}O_{3-\delta}$, but lower transport properties than $La_{1-x}Sr_xCoO_{3-\delta}$[223] and $La_2NiO_{4+\delta}$. Substituting the A-site cation La^{3+} with Sr^{2+} ($La_{2-x}NiO_{4+\delta}$ with $x = 0.1$ and 0.2) leads to a decrease in the diffusion coefficient D^* compared to the non-doped $La_2NiO_{4+\delta}$ due to a decrease in interstitial oxygen atoms.[216] This decrease was observed to be less severe for the substitution (Nd, Ca) than for (La, Sr) due to the similar ionic radius of Ca^{2+} and Nd^{3+} (1.18 and 1.16 Å) compared to La^{3+} and Sr^{2+} (1.22 and 1.31 Å). Similar trends were observed by other authors.[212,223,230,236] In contrast, the creation of Nd vacancies on the A-site improved the oxygen diffusivity and had a beneficial effect on k^*. The substitution of Ni (B-site) with other transition metal ions (Fe, Cu, Co) gave mixed results regarding the diffusion properties. The substitution of Ni with Co ($x \geq 0.5$) leads to slightly higher diffusion and largely enhanced surface exchange coefficients, with remarkably low activation energies of around 20 kJ mol^{-1} reported.[202,237] Although the surface exchange coefficient k^* for $La_{2-x}Sr_xNi_{1-y}M_yO_{4+\delta}$ (M = Fe, Cu, Co) showed an increase after the substitution of Ni with Co, iron did not have a significant effect and Cu substitution was detrimental to the coefficient k^* up to around 800 °C.[238] Similar observations were made for Ca-doped NNO ($x = 0.2$).[216] Another strategy to enhance material properties is the development of mixed or composite nickelate electrodes, which have shown improved performance compared to single phases as well as better TEC matching between the electrode material and electrolyte.[239] A significant improvement in conductivity σ, δ-values, and electrochemical performance was achieved for mixed composition nickelate electrodes $La_{2-x}Pr_xNiO_{4+\delta}$ ($0.0 \leq x \leq 2.0$) (LPNO).[240–243] In this series, the highest R_P was observed for LNO with 0.28 Ω cm^2 at 700 °C. With increasing Pr content, the R_P decreased to 0.03 Ω cm^2 for PNO.[240] The composite electrodes with a $La_2NiO_{4+\delta}$ and $La_4Ni_3O_{10-\delta}$ ratio of 40 : 60 showed the highest conductivity of ~29 S cm^{-1} at 700 °C, in the same range as $La_4Ni_3O_{10-\delta}$ (~30 S cm^{-1}) and with a much lower ASR in symmetrical cell measurements (0.90 Ω cm^2) compared to $La_4Ni_3O_{10-\delta}$ (~1.47 Ω cm^2). The best electrochemical performance was observed for a 50 : 50 wt% mix with an ASR of 0.62 Ω cm^2 at 700 °C.[244] Table 8 summarizes the electrochemical performance of nickelate materials as an oxygen electrode material in solid oxide electrolysis cells.

3.2.3. Electrode microstructure. In addition to the selected electrode material, the electrode performance is highly influenced by the microstructural design, including electrode thickness, particle connectivity, particle size and distribution,

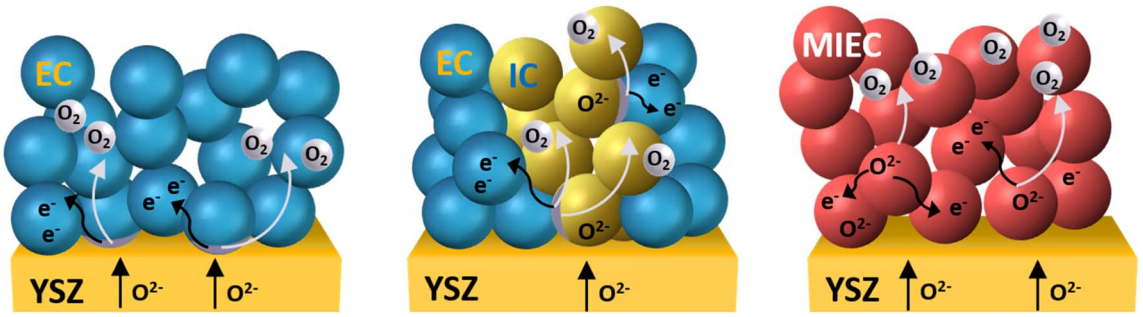

Fig. 10 Microstructures for SOC electrodes. (left) Single-phase electron conductor, *e.g.*, LSM; (middle) ion conduction (IC)/electronic conduction (EC) composite structure, *e.g.*, LSM-YSZ. (right) Single-phase MIEC electrode, *e.g.*, LSCF. The oxygen evolution reaction (OER) is restricted to the triple-phase boundaries (TPBs) in the case of a single EC layer as well as for the composite oxygen electrode including both an electronic conductor and an ionic conductor (EC + IC). Materials with mixed ionic and electronic conductivity (MIEC) properties enable the reaction at triple- and double-phase boundaries, thus extending the reaction zone.

electrochemically active penetration depth, and adhesion to the electrolyte. Thermal treatment, material synthesis, and the different fabrication techniques determine the active area of the chosen material (*e.g.*, triple/double-phase boundary length or available surface).[245–247] For single-phase electron conductor materials, for example, LSM and composite electrodes, the active areas are located exclusively at the interface between the gas phase, the electron-conducting (EC) electrode, and the ion-conducting (IC) electrolyte, as illustrated in Fig. 10a and b, which is therefore referred to as the triple-phase boundary (TPB). As seen in Fig. 10c, MIEC electrodes, for example, LSCF, have an entirely electrochemically active electrode surface, thus extending the reaction zone from TPB to include reactions taking place at the solid/gas double-phase boundary (DPB).

The development of the oxygen electrode for solid oxide cells at Forschungszentrum Jülich optimized the electrode material parameters, for example, microstructure, chemical composition, and thickness as well as the processing techniques. Fig. 11 shows cross-sections of the typical fuel electrode-supported O^{2-}-conducting SOC developed over the last few decades.

Until 2010, the "state-of-the-art" fuel electrode-supported cells manufactured at Forschungszentrum Jülich were characterized by a double-layered $La_{0.65}Sr_{0.3}MnO_3$ (LSM)/LSM-Y_2O_3-stabilized ZrO_2 (YSZ) oxygen electrode applied on a thin YSZ electrolyte (Fig. 11a).[248] These cells were mainly operated in fuel cell mode at temperatures between 800 °C and 900 °C. Subsequent studies focused on the variation of the LSM/YSZ ratio, thickness, and porosity of the oxygen electrode functional layer and current collector layer as well as the grain size distribution of the electrode material.[248–250] Early studies on LSM and the composite LSM-YSZ electrode investigated the correlation between microstructure and electrode performance. A correlation between performance and structure was observed for screen-printed LSM on YSZ and identified the length of the TPB and electrode thickness as the main influencing factors.[251] The performance of a composite LSM-YSZ layer and two current collecting layers of LSM sintered at different temperatures showed that decreasing sintering temperatures led to smaller grain size and higher electrode porosity.[252] Several studies also underlined the decrease in cell resistance with reduced particle size and an optimized current collector layer.[121,253,254] Noble-metal-containing oxygen electrodes showed enhanced catalytic activity due to higher surface reactions in comparison to conventional Ni-8YSZ/8YSZ/LSM-8YSZ/LSM cells manufactured at Forschungszentrum Jülich with a 60/40 wt% LSM-8YSZ functional layer.[255]

The development of mixed ionic–electronic conducting perovskite-type electrode materials, for example, lanthanum

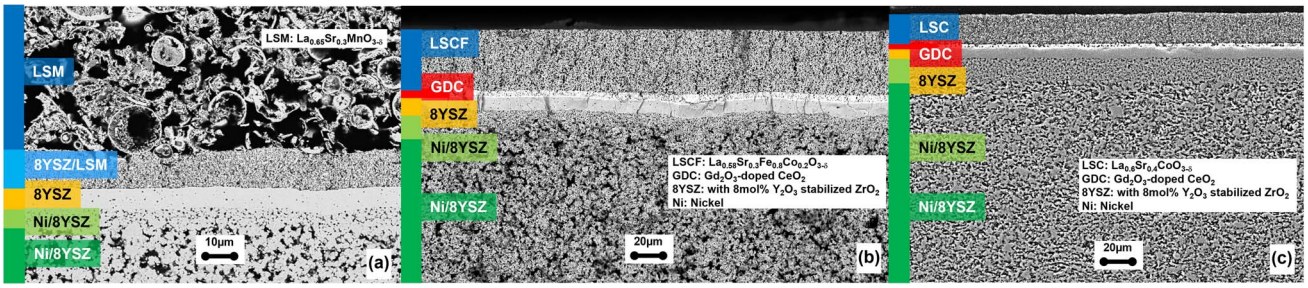

Fig. 11 Novel SEM micrographs of the fuel electrode-supported single cell cross sections comparable to:[248,261] (a) cell manufactured at Forschungszentrum Jülich and characterized by a double-layered $La_{0.65}Sr_{0.3}MnO_3$ (LSM)/LSM-Y_2O_3-stabilized ZrO_2 (YSZ) oxygen electrode applied on a thin YSZ electrolyte. (b) Cell manufactured at Forschungszentrum Jülich with a 5 µm-thick diffusion barrier layer (GDC, gadolinia-doped ceria) and a 40 µm-thick $La_{0.58}Sr_{0.4}Co_{0.2}Fe_{0.8}O_{3-\delta}$ (LSCF) oxygen electrode. (c) Pre-test commercial Elcogen® cell made of LSC with a GDC barrier layer reduced at 900 °C.[262]

strontium cobalt ferrite (LSCF), aimed to achieve higher power densities for fuel electrode-supported cells (Fig. 11b). In addition, the operating temperature could be lowered due to higher electrocatalytic activity and higher oxygen-ion conductivity. The new cells were assembled as the LSM electrode cells in the first approach with equivalent materials and layer thicknesses for the fuel electrode, support, and electrolyte. Later studies optimized the cell geometry in terms of the electrode thickness, material composition, and sintering temperature.[256,257] Due to the chemical reactivity of these materials with the YSZ electrolyte, the investigation of thin-film processes for barrier interlayers comprised of GDC gained an increased significance.[258] A screen-printed diffusion barrier layer made of GDC is now applied whenever an LSC(F)-based electrode is used for intermediate operating temperatures (~700 °C). State-of-the-art commercial Elcogen® fuel electrode-supported cells (Fig. 11c) incorporate oxygen electrodes comprised of strontium-substituted lanthanum cobaltite ($La_{1-x}Sr_xCoO_{3-\delta}$, (LSC)), which exhibits significant ionic conductivity (0.01–0.45 S cm^{-1}) in addition to high electronic conductivity in the operating temperature range of 650–800 °C.[259] Lower operating temperatures (<700 °C) in fuel cell mode with LSCF oxygen electrodes require thinner barrier layers applied by, for example, PVD or sol–gel technology.[109,260]

In recent years, the influence of electrode microstructure was studied by electrostatic spray deposition (ESD).[121,129,263–266] Electrospray is a low-cost electrohydrodynamic method used to deposit thin films and coatings with various morphologies. The inorganic or organometallic precursor materials dissolved in organic solvents result in sub-micrometer droplets accelerated towards the substrate. The morphology can be varied depending on the deposition conditions, which enables the fabrication of, for example, nanosponge-like, nanopillar, or dense materials.[267]

$La_{0.6}Sr_{0.4}Co_{0.2}Fe_{0.8}O_{3-\delta}$ (LSCF) cathode films with different morphologies on a dense $Ce_{0.9}Gd_{0.1}O_{2-\delta}$ (GDC) electrolyte were synthesized as shown in Fig. 12.[263] The FIB-SEM reconstruction differentiated between cracked, coral, and dense microstructures. The coral microstructures showed distinct features, with solid particles arranged in highly ramified structures and a thickness of up to 25 μm. The cracked films exhibited a thickness varying between 3 μm and 8 μm and contained noncontinuous reticulated surfaces, with gaps of ~1 μm throughout the surface. All films displayed the three elementary steps identified as the charge transfer process at the LSCF/GDC interface, the diffusion process within the volume of LSCF, and oxygen transfer at the LSCF/gas interface. The lowest polarization resistance R_P of 0.82 Ω cm^2 at 600 °C was found for the coral sample with a high surface area of around 24.7, normalized to the geometrical area. Nanostructured MIEC electrode materials can therefore be regarded as promising candidates for intermediate temperatures. The influence of different microstructures for two LSCF layers sequentially deposited onto the $Ce_{0.9}Gd_{0.1}O_{2-\delta}$ (GDC) substrate was shown as well.[121] The first layer of nano-scaled LSCF with a thickness of 7 μm was deposited by electrostatic spray deposition (ESD). A current collector layer of $La_{0.58}Sr_{0.4}Co_{0.2}Fe_{0.8}O_{3-\delta}$ with a thickness of ~45 μm and a larger particle size was deposited by screen printing after annealing. The area-specific resistance (ASR) determined from impedance spectroscopy measurements decreased from 0.82 Ω cm^2 (ref. 268) to 0.3 Ω cm^2 at 600 °C.

Similar investigations were made into the microstructural design of $La_2NiO_{4+\delta}$ (LNO) as an oxygen electrode on $Ce_{0.9}Gd_{0.1}O_{2-\delta}$ (GDC) electrolyte to enhance electrochemical properties characterized through the polarization resistance (R_P).

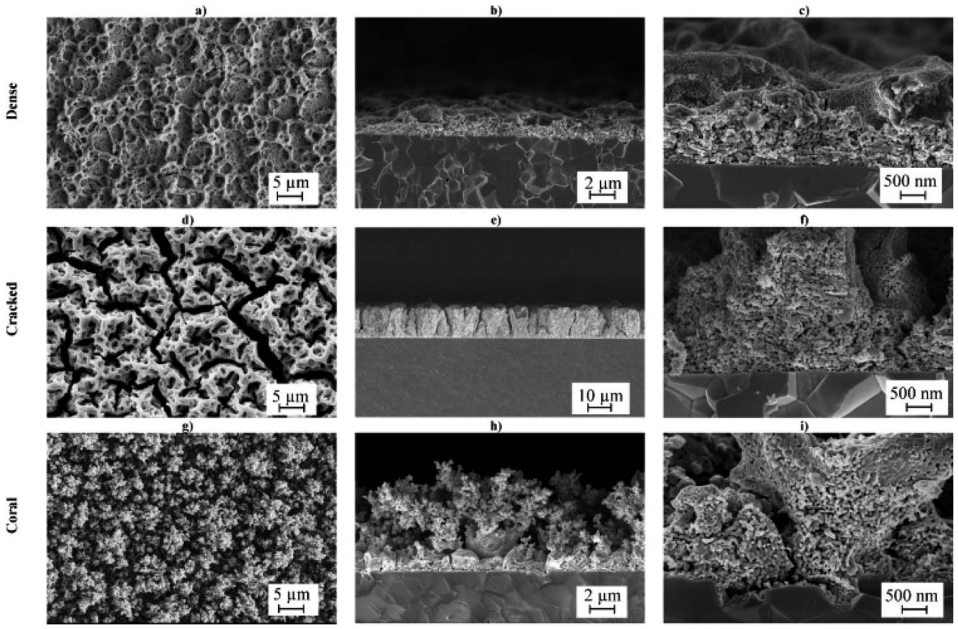

Fig. 12 SEM micrographs of surface and cross-sectional views of dense (a–c), cracked (d–f), and coral (g–i) $La_{0.6}Sr_{0.4}Co_{0.2}Fe_{0.8}O_{3-\delta}$ (LSCF) films. Reprinted from ref. 264, copyright 2012, with permission from Elsevier.

Compact 1–2 μm-thick LNO layers were deposited in addition to a 12 μm porous screen-printed LNO electrode on top (particles in the range of 1–2 μm), thus decreasing the R_P value from 7.4 to 1.0 Ω cm^2 at 700 °C.[269] The thin, compact LNO layer enhanced the contact between the electrode and the electrolyte and therefore also oxygen mobility. Higher sintering temperatures can also increase layer connectivity while simultaneously decreasing the electrode surface area. The insertion of a dense base layer was shown to lower the sintering temperature and enlarge the TPB region. This decreased the ASR at 600 °C by 35% compared to the best porous cell.[270]

The polarization resistance of $La_2NiO_{4+\delta}$ electrodes with different microstructures prepared on $Ce_{0.9}Gd_{0.1}O_{2-\delta}$ (GDC) by ESD and screen printing (SP) was analyzed (Fig. 13).[266] The porous electrode with a 3D coral microstructure and a thickness of 20 μm (sample 1, particle size ~100 nm) exhibited an intermittent cathode/electrolyte interface coupled with a rough contact between the current collector and the top of the electrode (R_P = 40.73 Ω cm^2 at 600 °C). The implementation of a thin, dense LNO interlayer with a 3D coral microstructure on top (sample 2, particle size ~120 nm) improved the cathode/electrolyte interface connectivity, which is crucial for the charge transfer process from cathode to electrolyte (R_P = 3.33 Ω cm^2 at 600 °C). A screen-printed cathode with a thickness of 20 μm (sample 3, particle size ~400 nm, R_P = 3.53 Ω cm^2 at 600 °C) was reported. Vibhu *et al.* achieved an R_P of 0.93 Ω cm^2 at 600 °C for a 20 μm thick screen-printed LNO electrode with an average particle size of 0.6 μm on a YSZ electrolyte.[240]

The optimized R_P of 0.42 Ω cm^2 was achieved at 600 °C by combining the thin, dense LNO interlayer with an LNO 3D coral microstructure and a screen-printed current collecting layer on top (sample 4). The improved electrochemical performance is related to the improved electric contact between the current collector and the electrode, resulting in decreased ohmic resistance. The thin, dense contact enhances the oxygen ion transfer between the electrode and the electrolyte.

Nanostructured materials have been suggested as a means of improving gas diffusivity in the electrode bulk and increasing the specific surface area of the porous electrode structure. Electrospun ceramic one-dimensional (1-D) nanofibers provide a large surface-to-volume ratio with good catalytic activity and high charge mobility. The diameters of the as-spun nanofibers range from 100 nm to 300 nm (ref. 271 and 272) depending on the materials. With a successful synthesis of LSCF nanofibers by electrospinning, a polarization resistance of 0.26 Ω cm^2 at 750 °C was achieved.[271] The cell performance was further improved by the infiltration of 20 wt% GDC, decreasing the R_P to 0.21 Ω cm^2 at 750 °C. $Sr_2Fe_{1.5}Mo_{0.5}O_{6-\delta}$ nanofibers used as electrode material in a symmetrical cell setup with humidified air exhibited a similar performance at 750 °C. Despite the performance of nanostructured materials, the microstructural changes when sintered at elevated temperatures will affect the performance and change the nanofiber porosity.[273]

3.2.4. Degradation mechanisms

3.2.4.1. Chemical stability and delamination. ABO_3 perovskite oxides (Fig. 6a), double perovskites like $AA'B_2O_{5+\delta}$ (Fig. 6b), and Ruddlesden–Popper $A_{n+1}B_nO_{3n+1}$ (RP, n = 1 shown in Fig. 6d) exhibit remarkable capabilities as oxygen electrodes for electrolysis, but they are hindered by degradation effects. The fast degradation of the oxygen electrode responsible for the

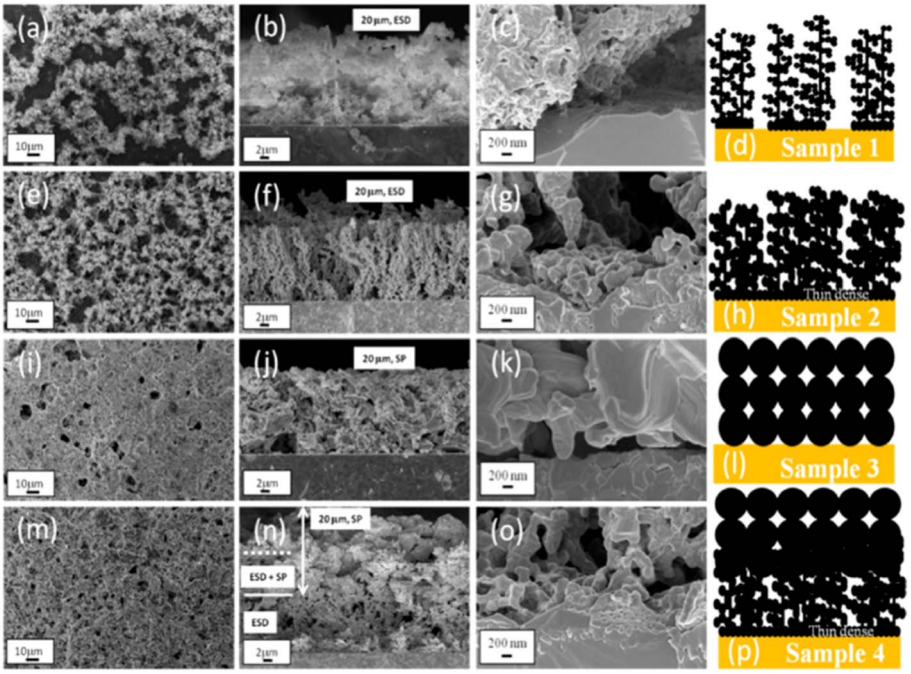

Fig. 13 Schematic and SEM micrographs of calcined films showing the surface, cross sections, and scheme of the samples. Sample 1 and sample 2 were obtained by electrostatic spray deposition (ESD). Sample 3 was prepared by screen printing (SP). Sample 4 was prepared using a combination of SP and ESD. For the individual figures labelling please refer to the original publication. Reprinted from ref. 266 with permission from Elsevier.

oxygen evolution reaction (OER) has affected the widespread adoption of solid oxide electrolysis cells. Interface evolution is considered one of the most critical factors determining the stability and performance of solid oxide electrolysis cells. The typical changes at the electrode/electrolyte interface are considered detrimental to the cell performance and include microstructural changes, interfacial reactions, micropore formation, element segregation/diffusion, and delamination.

In addition, the segregation of electrode components at the surface leads to the deterioration of surface functionality.[274] Surface segregation is influenced by, for example, lattice structure, operating temperature, ion mobility, polarization, and composition/stoichiometry. The difference in ion size is one main factor that leads to enrichment or depletion compared to the bulk phase.[275] Perovskites are typically comprised of large A-site (lanthanide and/or alkaline-earth cation) and smaller, catalytically active B-site (transition metal) cations. The segregation of the larger A-site cation to the surface forms insulating AO islands or RP layers,[276] which obstruct contact of the B-site cation with reactants and hinder oxygen and charge transfer.[277] Recent studies on A-cation segregation suggest that a suitable choice of A-site cations can minimize surface segregation in perovskites.[275]

The investigation of LSM chemical stability with the typical electrolyte YSZ has shown that cation (Sr and Mn) migration plays a key role in electrode deactivation. Depending on the stoichiometric composition of LSM, a high Sr content leads to Sr depletion and the interfacial formation of $SrZrO_3$. However, it was suggested that a deficiency at the A-site in perovskites leads to Mn diffusion into YSZ and chemical reactivity to La_2O_3 and of $La_2Zr_2O_7$ at the electrolyte/electrode interface.[278–280] This phase is detrimental to the electrochemical activity and performance of the LSM electrode.[281,282] A recent characterization of the YSZ/LSM electrolyte/electrode interface with transmission electron microscopy (TEM) and DFT clarified the interfacial nanostructure, which is essential to improving cell performance and stability.[283] After much discussion on the nature of the interface,[284–289] an interlayer of self-limited width with partial amorphization and strong compositional gradient was found, which exhibited characteristics of a complexion stabilized between two bulk phases. Images taken with high-magnification EDS are provided in Fig. 14. The dark field STEM (DF-STEM) electron micrograph in Fig. 14a shows the LSM phase on top of the YSZ. The elemental mappings in Fig. 14b for Y and Zr (blueish colors), as well as for La, Sr, and Mn (reddish colors), present the intermixing of elements with YSZ at the grain boundary in a compositionally unique region (white dashed). Monte Carlo simulations and corresponding elemental line profiles are taken across the interface to verify these results and give an average interdiffusion width of 1.25 nm (Fig. 14d). Based on these findings, the origin of Sr surface nucleation after thermal aging was localized by combining force field-based simulations, energy dispersive X-ray spectroscopy (EDS), and multi-variate statistical analysis.[290] The graph on the left in Fig. 14 displays the validation through surface-sensitive XPS measurements, showing interfacial Sr enrichment occurring at the LSM/YSZ side of SOEC after aging. The aged sample was sintered at 1200 °C for 1 h and exhibited a slight accumulation of Sr at the surface and an increase in the Sr/La ratio by 11.5%. This corresponds to an increase of 9.7% in the nominal A site occupancy by Sr, which might result from the segregation of strontium oxide.

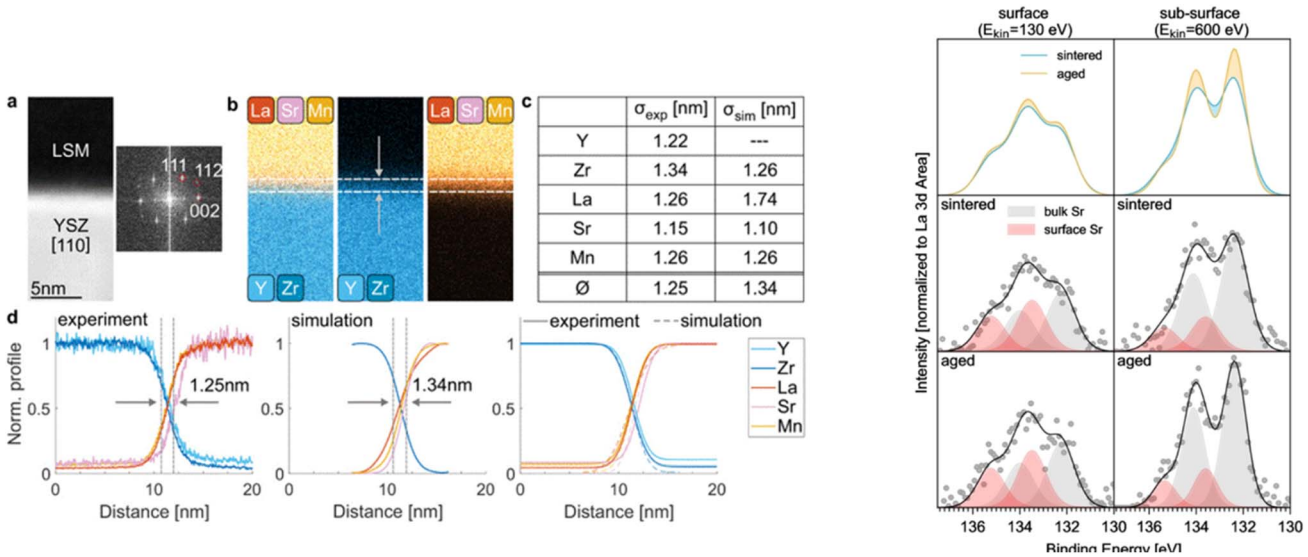

Fig. 14 Right: interdiffusion region at the YSZ/LSM interface visualized in (a) DF-STEM imaging of the YSZ/LSM interface and (b) EDS elemental mapping with dashed lines highlighting the interdiffusion region with (c) intergranular layer width derived from experiments and simulations. Experimental and theoretical average interdiffusion widths indicated in (d) are qualitatively close. Reproduced from ref. 283, which is licensed under the terms of the Creative Commons Attribution 4.0 License (CC BY, https://creativecommons.org/licenses/by/4.0/), © 2021 by the authors. Left: Sr 3d photoelectron spectra underline the change in Sr/La ratio upon aging at the surface, including the accumulation of Sr. Reproduced from ref. 290, which is licensed under the terms of the Creative Commons Attribution 4.0 License (CC BY, https://creativecommons.org/licenses/by/4.0/), © 2022 by the authors.

Experimental investigations showed that microstructural changes in the oxygen electrode could also lead to oxygen electrode delamination. This electrode delamination was related to the disintegration of the $La_{0.8}Sr_{0.2}MnO_3$ (LSM) particles and the formation of nanoparticles at the electrode/electrolyte interface.[291] The nanoparticle formation resulted from the shrinkage of the LSM lattice due to the migration of oxygen ions from the YSZ electrolyte into the LSM grain, thus oxidizing Mn^{3+}/Mn^{4+} into Mn^{4+} and creating local tensile stresses. The delamination at the electrode/electrolyte interface is a common failure mechanism attributed to the build-up of high internal oxygen partial pressure close to the interface.[292,293] The bubbles evolve under anodic overpotential and penetrate the porous electrode/electrolyte interface, which leads to pressure buildup.[294–296] Studies of Ni-YSZ/YSZ/LSM-YSZ electrolysis cells under high current densities exhibited hole/pore formation in the grain boundaries near the oxygen electrode, leading to very high grain boundary resistivity and thus increasing the ohmic resistance of YSZ.[297] Densification and delamination of the LSM-YSZ oxygen electrode were attributed to cation migration under a high anodic current (−1.5 A cm^{-2} at 750 °C).[298] Interdiffusion between the two phases was observed as well as an intergranular fracture along YSZ grain boundaries. La, Sr, and Mn cations are reported to segregate along the grain boundary of the electrolyte, thus facilitating the generation of oxygen gas bubbles, which in turn led to electrode delamination. The formation of the second phase $La_2Zr_2O_7$ is suggested to be the cause of LSM electrode delamination, as shown in eqn (9).[299]

$$LaMnO_{3+\delta} + ZrO_2 + 1/4O_2 \leftrightarrow 1/2La_2Zr_2O_7 + MnO_2 \quad (9)$$

Due to their high chemical reactivity with zirconia-based electrolytes, cobaltite-based electrodes such as LSC and LSCF are only used with a ceria-based barrier layer. Otherwise, the formation of the electronically insulating phases $SrZrO_3$ and $La_2Zr_2O_7$ can be observed as a result of Sr segregation.[137] This phenomenon was observed at the oxygen electrode/electrolyte interface after the operation of an electrolysis cell for 6100 h at −0.75 A cm^{-2} between 777 °C and 780 °C.[42] The authors theorized from the microscopic results that oxygen electrode demixing, the transport of gaseous Sr species, and Zr mass transport through the grain boundary to the 8YSZ electrolyte are contributing to the degradation of the LSCF electrode. This is driven by the chemical potential gradient of $SrZrO_3$ formation. The relationship between the material destabilization and operating conditions was characterized by comparison of

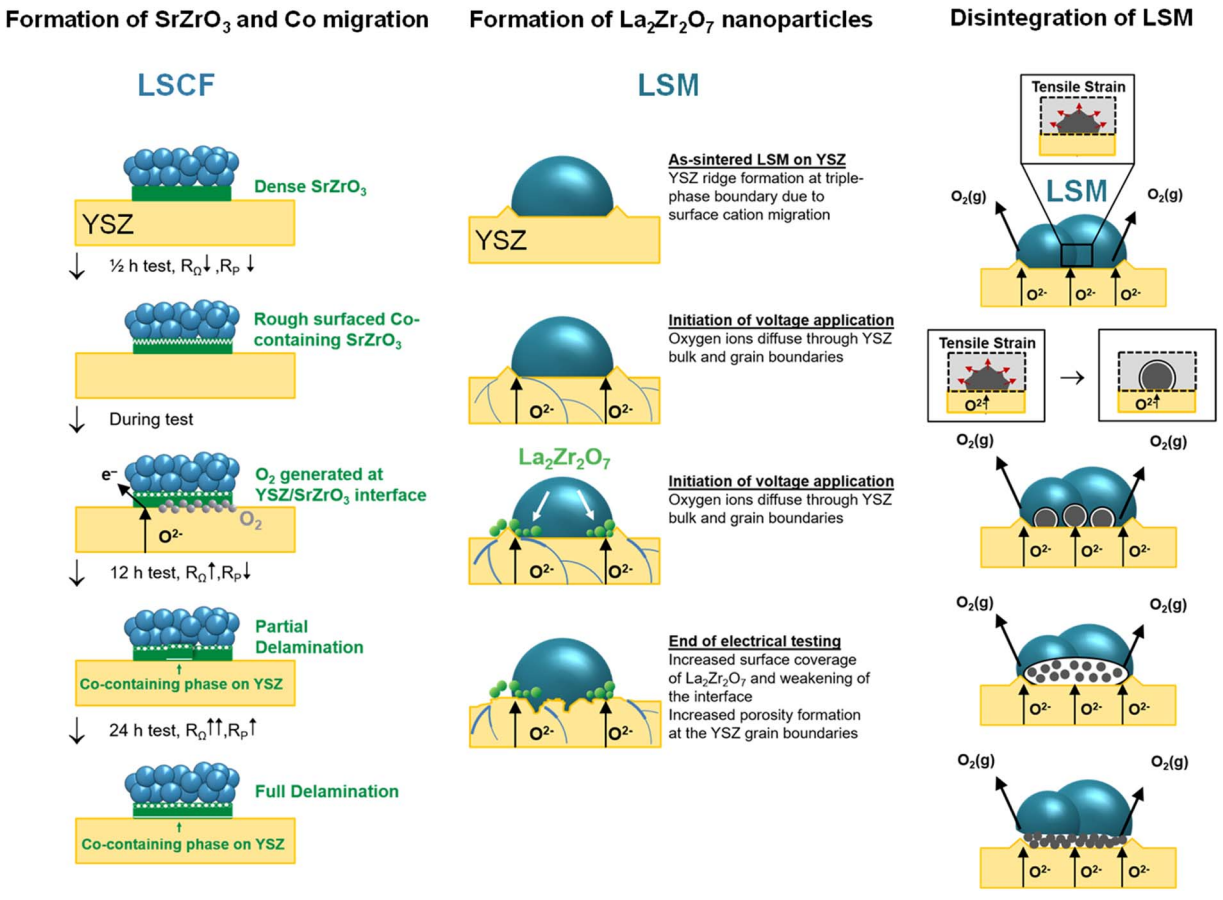

Fig. 15 Proposed delamination mechanisms due to microstructural change: Co migration and formation of $SrZrO_3$. Adapted and reprinted from ref. 302, copyright 2018, with permission from Elsevier. Formation of $La_2Zr_2O_7$ nanoparticles. Adapted and reprinted from ref. 299, copyright 2012, with permission from Elsevier. The disintegration of LSM due to tensile stress. Adapted and reprinted from ref. 291, copyright 2011, with permission from Elsevier.

reference samples and cells tested under both fuel cell and electrolysis mode through synchrotron X-ray microdiffraction and micro-fluorescence.[43] While pristine samples exhibited strontium zirconate and a Gd-rich interdiffusional layer pre-test/post-manufacturing, the accumulation of $SrZrO_3$ at the interface between the barrier layer and the interdiffusional layer was found for the aged samples. Additionally, the LSCF cell volume evolved due to strontium segregation. Both phenomena were found to be enhanced in electrolysis mode and thermally activated. Ni-YSZ-supported SOEC cells with an LSC-GDC oxygen electrode were tested at -1 A cm^{-2} in co-electrolysis conditions for 2700 h at 800 °C. The authors observed Sr and Co depletion at the LSC-GDC boundary of the tested cell around 3–5 μm from the electrode interface. As this depletion was not observed in the reference cell, the depletion was attributed to long-term testing.[300] The performance and stability were tested of the LSCF electrode for 50 h with and without a GDC interlayer in a Ni-YSZ/YSZ-supported full cell at 800 °C and -0.8 A cm^{-2}.[301] The cell without an interlayer showed a large increase in area-specific resistance (ASR) and more severe delamination compared to the measured cell with a GDC interlayer. The degradation of the cells was associated with the phase change of LSCF from rhombohedral to cubic. Half-cells measured in a three-electrode configuration at 800 °C after polarization with an electrolysis current of -1 A cm^{-2} for 24 h showed relatively stable ohmic resistance R_Ω for 18 h, with the resistance increasing abruptly thereafter.[302] The YSZ surface characterization showed the formation of an insulating $SrZrO_3$ layer at the LSCF/YSZ interface during the sintering of fresh samples. Post-test analysis suggested that the $SrZrO_3$ interlayer delaminated from the YSZ electrolyte rather than the LSCF electrode from the interlayer. Co diffusion into the $SrZrO_3$ layer and the YSZ electrolyte was confirmed by EDS analysis. The diffusion process enabled the formation of O_2 at the interlayer/electrolyte interface, which led to the delamination of the $SrZrO_3$ layer and the LSCF electrode.

Based on the proposed delamination mechanisms as described in Fig. 15, several studies have focused on counter-measures. To minimize the formation of $La_2Zr_2O_7$,[299] manganese-modified yttria-stabilized zirconia (Mn-YSZ) interlayer was utilized on the electrolyte.[303] The symmetrical cells were tested at 840 °C at a constant voltage of 0.8 V for 200 h in electrolysis mode. No delamination was observed post-test for Mn-modified cells. Compared to unmodified cells, less Mn migrated from the LSM electrode to the YSZ electrolyte. The authors hypothesized that the porous sol–gel coating averts high oxygen pressure build-up, thus diminishing the electrode delamination. Based on previous investigations about nanoparticle formation in LSM,[291] the LSM-infiltrated YSZ (LSM-YSZ) composite electrodes were prepared to prevent reactivity between LSM and the YSZ electrolyte.[304] The infiltrated LSM-YSZ oxygen electrodes exhibited high electrocatalytic activity and good stability under SOEC conditions compared to non-composite electrodes. The results underlined that the microstructural stability of the LSM nanoparticles is impacted by two opposing parameters: (a) LSM lattice shrinkage under the anodic polarization and (b) grain growth by thermal sintering. Inserting a $Ce_{0.43}Zr_{0.43}Gd_{0.1}Y_{0.04}O_{2-\delta}$ (CZGY) contact layer between the YSZ and GDC led to an increased interface stability and prevented GDC delamination. The CZGY contact layer improved the stability with the neighboring layers and prevented delamination during the short-term (100 h) electrolysis tests (800 °C, -0.8 A cm^{-2}). Cation surface segregation and phase instability also occur on various perovskite oxides for example, layered perovskite oxides and Ruddlesden–Popper oxides except for LSM and LSC/LSCF.

Chemical reactivity was also found between double perovskites, for example, $Sr_2Fe_{1.5}Mo_{0.5}O_{6-\delta}$ and derivatives with commonly used YSZ. This limits the selection of compatible

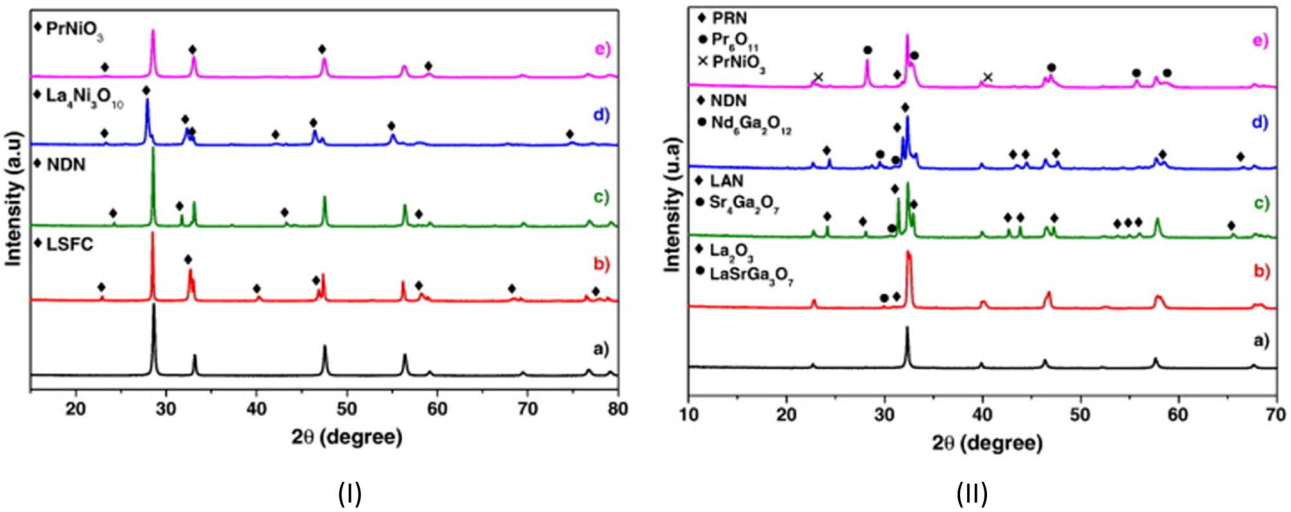

Fig. 16 Left: XRD patterns after heating at 1150 °C for 1 h: (a) GDC, (b) GDC/LSFC, (c) GDC/NNO, (d) GDC/LNO and XRD pattern after heating at 800 °C for 5 days for (e) GDC/PNO. Right: XRD patterns after heating at 1150 °C for 1 h: (a) LSGM, (b) LSGM/LSFC, (c) LSGM/LNO, (d) LSGM/NNO and XRD pattern after heating at 800 °C for 5 days for (e) LSGM/PNO. Reprinted from ref. 310, copyright 2013, with permission from Elsevier.

electrolyte materials or necessitates a protective layer of $Ce_{0.8}Gd_{0.2}O_{2-\delta}$ or $La_{0.6}Ce_{0.4}O_{2-\delta}$ deposited between the electrolyte and the electrode material. Stoichiometric composition is a crucial factor that affects the extent of SrO surface segregation. In addition to the amount of Sr dopant, thermodynamic calculations indicate that the B-site cation type impacts SrO activity in $(La,Sr)MO_3$ (M = Fe, Co, Mn), which decreases in the order of Co > Fe > Mn.[305] The surface chemistry of double perovskites $PrBaCo_2O_{5+\delta}$ (PBC) and $GdBaCo_2O_{5+\delta}$ (GBC) was investigated using low-energy ion scattering (LEIS) after annealing (400–800 °C).[306–308] The results showed segregation and surface domination of the larger A-site cation with B-cation-enriched regions below the surface. Similar observations were made when observing Ba and Co segregation out of the lattice after annealing at high temperatures (>800 °C).[309]

The chemical reactivity between Ruddlesden–Popper nickelates and commonly used electrolyte materials is an important factor in long-term SOEC application. The formation of an insulating phase can result from excessive chemical reactivity and lead to increased polarization resistance. The stability under operating conditions of lower-order RP is therefore the main issue in the long-term application of nickelates such as LNO, PNO, and NNO. Studies on chemical reactivity with the GDC electrolyte have shown that it has good chemical compatibility with $Nd_2NiO_{4+\delta}$.[310] With the electrolyte material YSZ, Nd_2NiO_4 has shown good stability from 700 °C to 900 °C and only a minor formation of $Nd_2Zr_2O_7$ at 1000 °C.[311] Compatibility tests with LSGM electrolytes have shown partial reactivity after 1 h in air at 1150 °C through the formation of $Nd_4Ga_2O_9$ due to Ga vaporization at high temperatures.[310]

$La_2NiO_{4+\delta}$ and $Pr_2NiO_{4+\delta}$ have been known to react with both YSZ and GDC.[311–313] The reactivity test of $La_2NiO_{4+\delta}$ (LNO) with YSZ shows the formation of an insulating pyrochlore $La_2Zr_2O_7$ phase at 900 °C after 72 h, which led to increased ASR values over 700 °C.[312] For the electrolyte material LSGM, the reactivity test shows good chemical compatibility with LNO, although small traces of decomposed LSGM (≈3%) were observed[310] (Fig. 16). Despite the relative stability of LSGM, the authors argued that the very low electrical conductivity of the small impurities could infringe on cell performance. The secondary phases NiO, La_2O_3, and $La_3Ni_2O_7$ were observed after performing a reactivity test using GDC as an electrolyte.[312]

Pr-based lower-order Ruddlesden–Popper phases were observed decomposing, while the studies of higher order RP such as $Pr_4Ni_3O_{4+\delta}$ showed good structural stability up to 1000 °C.[243,314] PNO decomposition in air was observed for example after 24 h at 900 °C and the decomposition product reacted subsequently with YSZ to $Pr_2Zr_2O_7$ and Pr_6O_{11}.[311] The formation of the insulating phases was attributed to the thermodynamic instability of PNO above 700 °C and not the chemical reactivity.

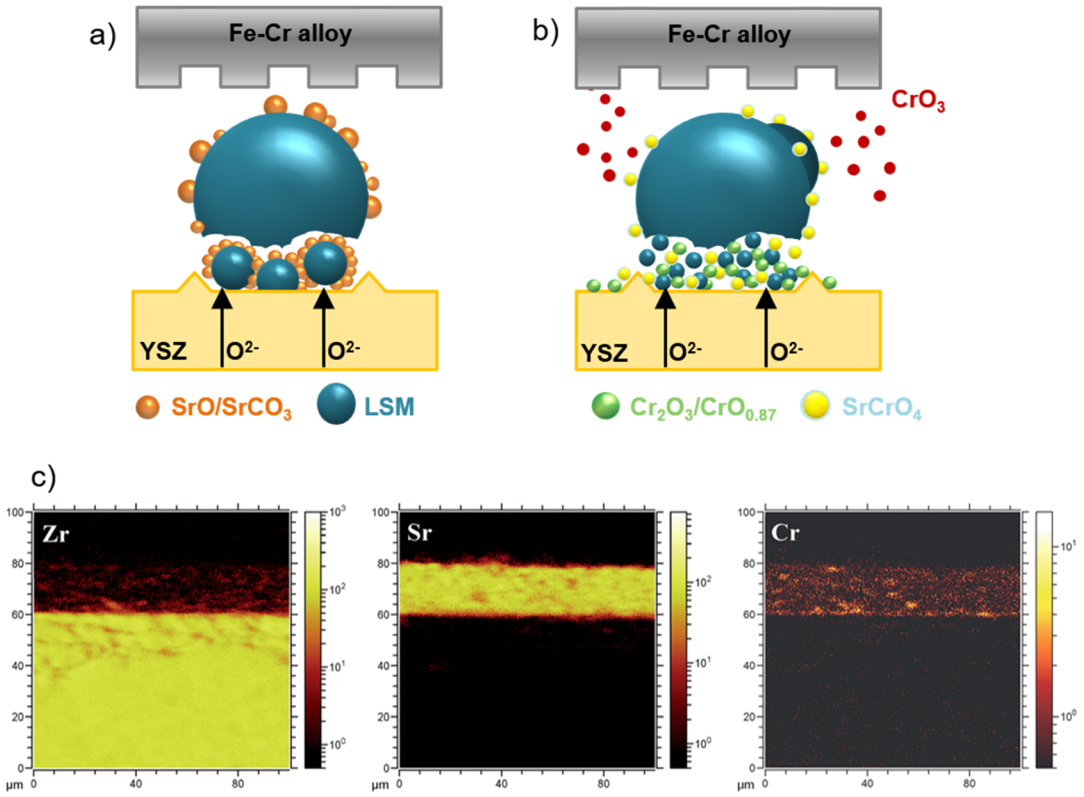

Fig. 17 Cr deposition and subsequent poisoning of the LSM oxygen electrodes under SOEC operating conditions. (a) LSM nanoparticle formation at the electrolyte/electrode interface. Under anodic polarization, SrO segregates from the bulk of the electrode to the surface. (b) Formation of $SrCrO_4$ on the LSM surface and Cr deposition on the electrolyte surface and at the electrolyte/electrode interface. (c) SIMS image of the LSM electrode taken under the rib of the Fe–Cr interconnects after 1 h at 800 °C and −0.8 A cm^{-2}. Reproduced and adapted from ref. 326 with permission from the Royal Society of Chemistry.

$Pr_2NiO_{4+\delta}$ also showed no stability with GDC, decomposing to the higher order RP $Pr_4Ni_3O_{10}$ and Pr_6O_{11}, although the results did not clarify whether PNO only decomposes above 700 °C or a chemical reaction between PNO and the electrolyte material occurred. Similar results were reported for an 8% PNO phase after sintering a PNO/LSGM sample for five days.[310] Higher order RP phases have relatively high total conductivity and are oxygen under-stoichiometric in contrast to the $n = 1$ phases.[229] In addition, the Ni^{3+} content is increased, which leads to higher chemical stability. Up to 1000 °C, the $Pr_4Ni_3O_{10+\delta}$ phase is fully stable under oxygen and decomposes into $Pr_2NiO_{4+\delta}$ and NiO at higher temperatures.[314]

3.2.4.2. Cr poisoning. An additional issue to consider is the interaction of oxygen electrodes and the Cr-forming alloys (*i.e.*, stainless steel), which are used as metallic interconnects in SOEC stacks similar to SOFC. They are inexpensive and easy to produce and exhibit high thermal and electrical conductivity. At high temperatures, volatile chromium species are generated under oxidizing conditions, which can react electrochemically with the LSM electrode and lead to fast material degradation.[315–317] The Cr deposition and poisoning of oxygen electrodes by the volatile species CrO_3 and $CrO_2(OH)_2$ from the protective Cr_2O_3 scale have been extensively studied under SOFC operation conditions.[318–323] It is known that under cathodic polarization, Cr deposition at the LSM/electrolyte interface and on the surface leads to the formation of Cr_2O_3 and the $(Cr,Mn)_3O_4$ spinel, which have a detrimental effect on cell performance.[315,324,325] Although Fe–Cr alloys are commonly used as interconnect materials for SOEC, little work has been carried out on electrode poisoning under SOEC conditions. The Cr poisoning of an LSM oxygen electrode under SOEC condition[313] is shown in Fig. 17.

The LSM electrode partially disintegrates to form LSM nanoparticles at the electrode/electrolyte interface. Under anodic polarization, $SrO/SrCO_3$ species segregate to the electrode surface, which is enhanced by the inhibition of Mn^{2+} generation. Cr deposition and high activity between Cr and Sr, in turn, lead to the dominant $SrCrO_4$ product on the electrolyte surface and the electrode/electrolyte interface, rather than the $(Cr,Mn)_3O_4$ spinels under SOFC conditions. Based on the nucleation theory,[327] the reaction of SrO segregation to the surface and the subsequent reaction with the gaseous Cr species is given by eqn (10)–(13).

Sr segregation:

$$La_{0.8}Sr_{0.2}MnO_{3+\delta} \rightarrow La_{0.8}Sr_{0.2-x}MnO_{3+\delta} + xSrO \quad (10)$$

Cr deposition *via* nucleation and grain growth route:

$$SrO + CrO_3 \rightarrow Cr\text{–}Sr\text{–}O_x \text{ (nuclei)} \quad (11)$$

$$Cr\text{–}Sr\text{–}O_x + CrO_3 \rightarrow CrO_y + Cr_2O_3 \quad (12)$$

$$Cr\text{–}Sr\text{–}O + SrO + CrO_3 \rightarrow SrCrO_4 \quad (13)$$

Chromium deposition of $SrCrO_4$, $CrO_{2.5}$, and Cr_2O_3 phases at the $La_{0.6}Sr_{0.4}Co_{0.2}Fe_{0.8}O_{3-\delta}$ (LSCF) oxygen electrode increased the overpotential of the O_2 evolution reaction (OER). The hindered electrocatalytic activity was linked to the significant deficiency of catalytically active Sr in the electrode bulk segregating to the electrode surface. The areas near the rib of the interconnect (Fig. 18) showed significantly higher Cr enrichment compared to the regions of the interconnect channels.[328] The dissociation of $La_{0.8}Sr_{0.2}CoO_{3-\delta}$ (LSC) was the reason to conclude that Cr-containing phases from the stainless steel interconnects are driven into the contact layer microstructure,

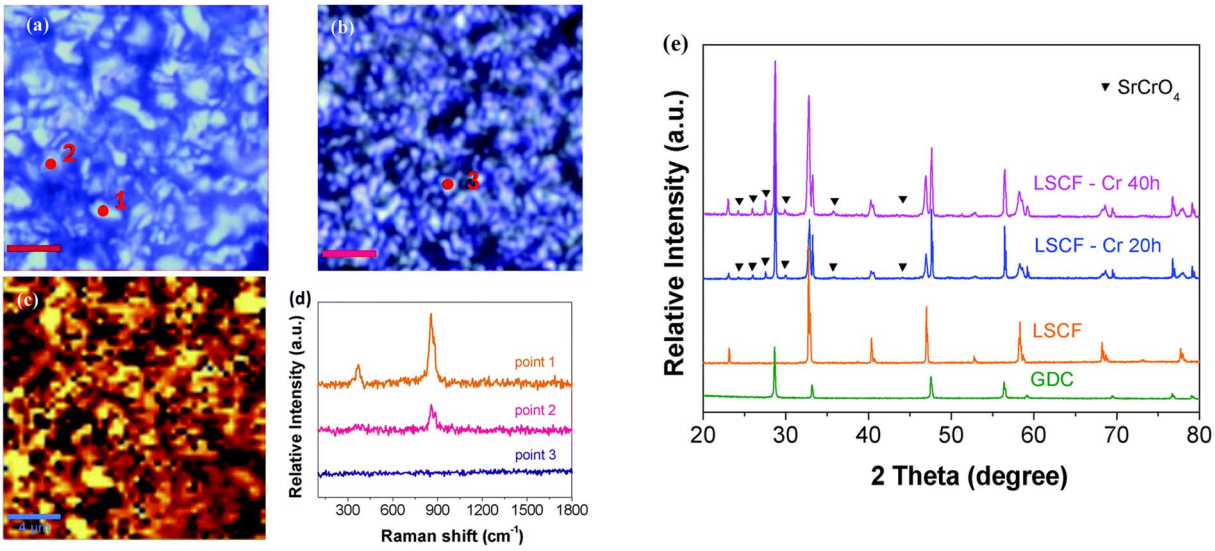

Fig. 18 Post-test analysis of an electrode before and after polarization at 900 °C and −0.2 A cm^{-2} in the presence of Fe–Cr interconnects: (a) optical images of the LSCF electrode surface under the Fe–Cr interconnect after 40 h treatment. (b) As-prepared cell before testing. (c) Raman spectroscopy mapping at $\nu = 860$ cm^{-1}, corresponding to $SrCrO_4$. (d) Raman profiles collected at points 1, 2, and 3. (e) XRD pattern before and after testing of the GDC electrolyte and the LSCF oxygen electrode for 20 h and 40 h at 900 °C and −0.2 A cm^{-2} in the presence of Fe–Cr interconnects. Reproduced from ref. 328 with permission from the PCCP Owner Societies.

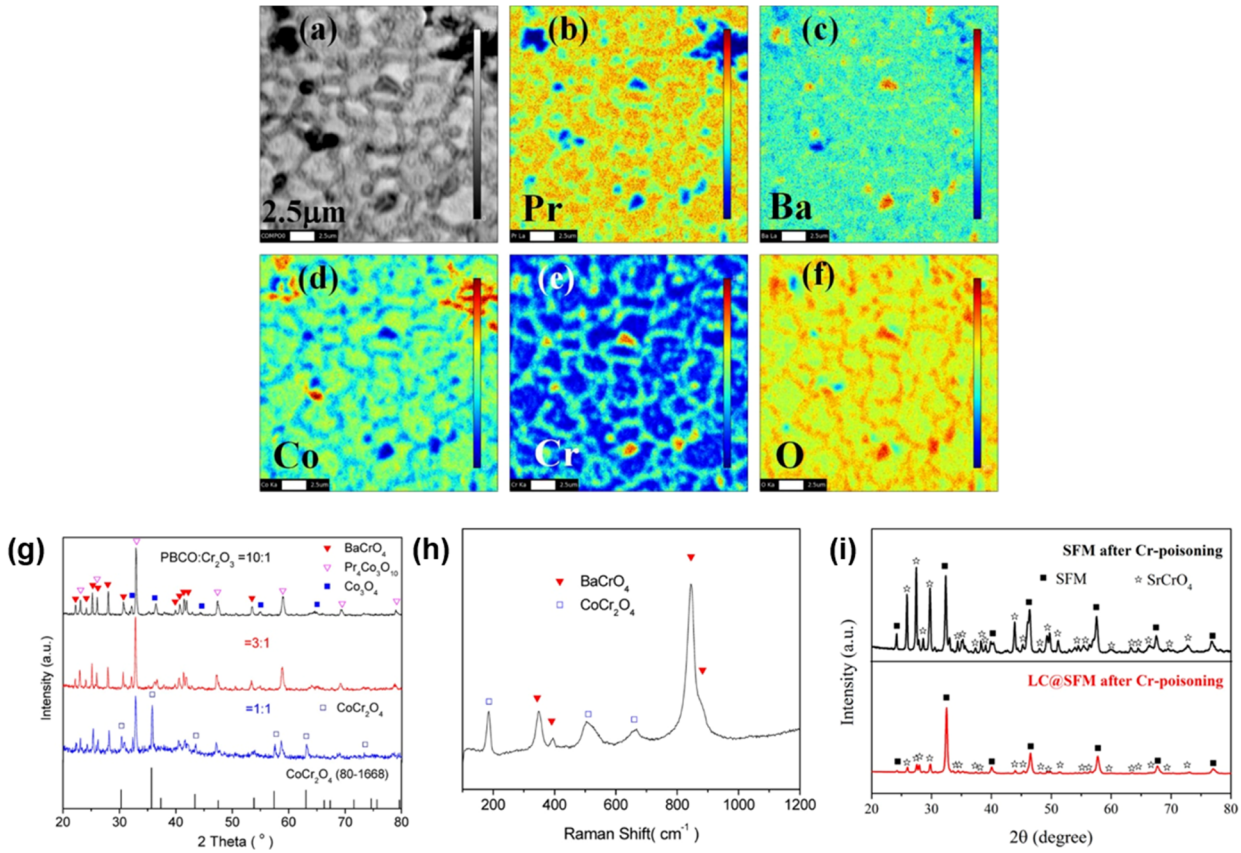

Fig. 19 (a) Backscattered electron (BSE) imaging of segregated PBCO surface at 900 °C in 100% O_2. Electron microprobe analyzer (EPMA) elemental mappings for (b) Pr, (c) Ba, (d) Co, (e) Cr, and (f) O. Higher concentrations are indicated in red, while lower concentrations with scale bars of 2.5 μm are highlighted in blue. (g) XRD patterns for PBCO–Cr_2O_3 mixtures after reacting for 5 h in air at 1000 °C, and (h) Raman profile of the PBCO–Cr_2O_3. Reprinted in part with permission from ref. 309. Copyright 2018 American Chemical Society. (i) XRD patterns after Cr poisoning tests for SFM and LSC@SFM surfaces. Reprinted with permission from ref. 330. Copyright 2019 American Chemical Society.

thus causing the long-range transport of Sr and Co cations and, consequently, La–Cr–O phases.[329]

The effects of Cr poisoning upon LSM and LSC(F)-based electrodes have received the highest level of research interest. Although other oxygen electrode materials have also been investigated, the current literature is mostly focused on Cr effects in SOFC, and degradation studies are often not conducted for an extended period (<500 h). Few studies consider double perovskite materials in terms of their chromium poisoning resistance. The durability of strontium iron-molybdenum oxygen (SFM) electrodes was reported to be affected by Cr poisoning (Fig. 19i). Short-term Cr-poisoning tests of around 160 h on symmetrical cells with SFM oxygen electrodes showed Cr species poisoning the electrode surface, resulting in the formation of $SrCrO_4$ after the direct reaction of the Sr with Cr_2O_3 and gaseous CrO_3.[330] The reactivity with chromium was studied by looking at $SmBaCo_2O_{5+\delta}$ (SBC)[331] and later $PrBaCo_2O_{5+\delta}$ (PBC)[309] (Fig. 19a–h). At high temperatures, Ba and Co cation diffusion was observed for PBC, forming BaO and Co_3O_4 precipitates on the surface, mainly located at the grain boundaries. In the presence of Cr, $BaCrO_4$ was formed and had an impact on electrochemical performance.[309]

The electrochemical activity of $SmBaCo_2O_{5+\delta}$ (SBC) also degraded quickly in the presence of a chromium-forming metallic interconnect. The authors concluded that the Cr deposition was induced by the segregated BaO on the SBCO surface, leading to the formation of $BaCrO_4$.[331] Similar results were observed for $NdBaCo_2O_{5+\delta}$ (NBC) and $PrBa_{0.5}Sr_{0.5}Co_{1.5}Fe_{0.5}O_{5+\delta}$ (BSCF), although the authors found that LNO ($La_2NiO_{4+\delta}$)-infiltrated PBSCF improved tolerance to Cr poisoning. This result highlights the possibility of Cr-poisoning-resistive oxygen electrodes in the absence of nucleating agents (Sr, Ba, Mn). Long-term measurements over 1000 h revealed that $La_2NiO_{4+\delta}$ oxygen electrodes exhibited good stability under dry conditions in the presence of Cr.[332] However, the oxygen activity declined as soon as humidity was introduced into the system, and the LNO surface layer decomposed. Similar results were found for PNO.[333] Although LNO electrodes react readily with Cr_2O_3 to form $LaCrO_3$ and $LaNiO_3$ reaction products, their chromium tolerance was found to be higher than for LSCF oxygen electrodes.[334] $Nd_2NiO_{4+\delta}$ (NNO) is a potential alternative to standard perovskite materials due to its high catalytic activity and chromium poisoning tolerance.[335] No chromium-related compound was observed in either the $Nd_2NiO_{4+\delta}$ cathode or the NNO/YSZ interface. However, Nd depletion of the nickelate

was identified as a result of secondary phase formation with the Cr contaminants.[336] The changes in NNO due to Cr poisoning only had a minor influence on the surface exchange properties.[183]

3.2.5. Summary of oxygen electrode materials. The state-of-the-art oxygen electrode materials lanthanum strontium cobalt ferrite ($La_{1-x}Sr_xCo_{1-y}Fe_yO_{3-\delta}$ and (LSCF)) lanthanum strontium cobaltite ($La_{1-x}Sr_xCoO_{3-\delta}$ (LSC)) exhibit good performance and durability for long-term application (>5000 h) in solid oxide electrolysis stacks in operating conditions around 700 °C to 850 °C. New perovskite-based materials for the oxygen side compromise of double perovskites *e.g.*, $Sr_2Fe_{1.5}Mo_{0.5}O_{6-\delta}$ (SFM), $PrBaCo_2O_{5+\delta}$ (PBC) and $GdBaCo_2O_{5+\delta}$ (GBC) as well as Ruddlesden–Popper phases such as $La_2NiO_{4+\delta}$ (LNO), $Nd_2NiO_{4+\delta}$ (NNO), and $Pr_2NiO_{4+\delta}$ (PNO). They show sufficient performance in short-term measurements up to ~200 h. However, the stability of these materials has not been investigated yet in stack systems under industrial operating conditions for longer periods. Known stability issues include segregation reactions in double perovskites and chemical reactivity with currently used electrolyte materials like yttria-stabilized zirconia (YSZ) and gadolinium-doped ceria (GDC). For lower-order Ruddlesden–Popper phases $Ln_{n+1}Ni_nO_{3n+1}$ ($n = 1$) the main issue in a long-term application is the decomposition above 600 °C, for example, $Pr_2NiO_{4+\delta}$ decomposes into Pr_6O_{11}, $PrNiO_{3-\delta}$, and $Pr_4Ni_3O_{10+\delta}$ phases. Despite this phase instability, good catalytic activity of these decomposition products has been observed.

3.3. Fuel electrode

3.3.1. Requirements. The fuel electrode of an SOEC (cathode) must fulfill several requirements to achieve sufficient performance. First of all, the electrode must be made of a catalytically active material with regard to the electrolysis of varied inlet fuels. In the case of steam electrolysis, see Fig. 20a, the fuel electrode catalyzes the dissociation of gaseous water molecules (water splitting reaction (WSR)) into oxygen ions and gaseous hydrogen at the catalytically active sites of the fuel electrode (hydrogen evolution reaction (HER)).[337–339] The reduction of CO_2 to CO plus oxygen ions during CO_2 electrolysis (CO_2RR) at the electrode interface is schematically shown in Fig. 20b.

The main advantage of SOECs is the combination of steam and CO_2 electrolysis, referred to as co-electrolysis, resulting in the production of industrially crucial syngas (H_2 + CO). Here, both the dissociation of water molecules and the reduction of CO_2 take place at the active sites of the fuel electrode for the respective reaction. However, depending on the gas composition, the conversion of CO_2 into CO takes place mainly due to the reverse water–gas shift reaction (RWGS) between the produced H_2 and CO_2, and is not electrocatalytically, but catalytically activated.[340,341]

The fuel electrode also requires long-term chemical stability in humid reducing atmospheres as well as in mixed gases. In particular, the respective gas composition can have a strong influence on the performance and durability of the fuel electrode. The gas mixture, which is partly dependent on the electrolysis mode, can consist of different fractions of reducing agents (*e.g.*, H_2), water molecules, carbon-containing molecules (CO_2, CO), and possibly carrier gas. The optimization of the electrode material is dependent on the gas mixtures occurring during the electrolysis operation.

An example of how the complexity of the gas composition influences the electrode material has been fairly well investigated for the commonly used Ni-YSZ fuel electrode. The selection of Ni-YSZ as a fuel electrode material for SOECs is based on the fact that the materials used in SOECs were initially adapted from the solid oxide fuel cell. However, the gas mixture at the fuel electrode for SOFCs differs from the composition used for electrolysis cells. For instance, there is a variation in fuel gas properties such as oxygen partial pressure, humidity, and the amount of reducing gases. In the case of Ni-YSZ being used as a fuel electrode in steam electrolysis, an increase in humidity in the fuel gas initially leads to a higher conversion of H_2O into H_2 and $1/2O_2$. While at the same time, material degradation and reduced electrode performance are accelerated over time.[342,343] Additionally, the observed cell voltage in SOEC operation is higher at 1.1–1.4 V compared to SOFCs (0.6–1.0 V), which leads to a decrease in the local oxygen partial pressure at the fuel electrode side.[42]

The fuel electrode material also requires preferably high electronic and ionic conduction to extend the electrochemical reaction area (triple-phase boundary (TPB)) as well as matching

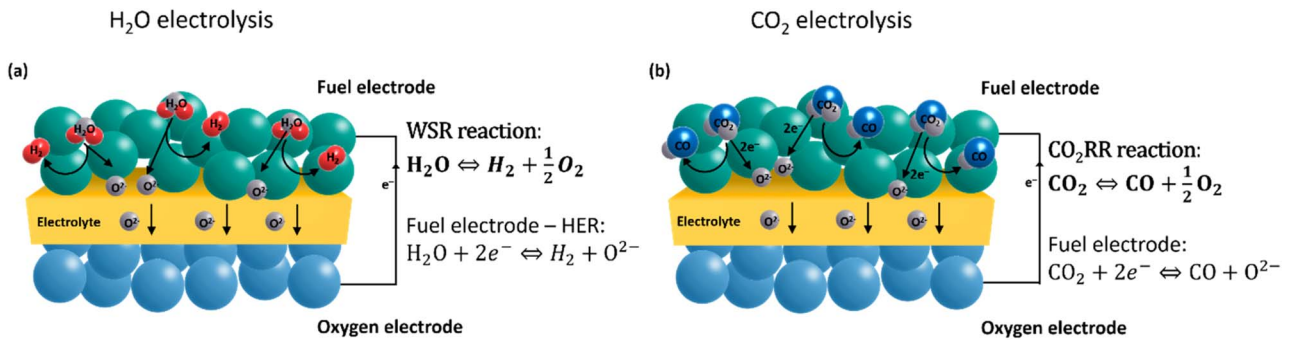

Fig. 20 Schematic description of the reactions at the fuel electrode/electrolyte interface during different electrolysis operations: (a) steam electrolysis: water splitting reaction (WSR) including the hydrogen evolution reaction (HER). (b) Carbon dioxide electrolysis: carbon dioxide reduction reaction (CO_2RR).

thermomechanical properties of the electrode material with the other components of the solid oxide cell, especially the electrolyte. A sufficient electrical conductivity for the fuel electrode, which should be achieved throughout the whole operation time, is in the scale of 100 S cm^{-1}.[344] The relative expansion depending on temperature given by the thermal expansion coefficient (TEC) is typically considered the first indicator of the thermomechanical compatibility between the electrode and the electrolyte. The TEC values for commonly applied electrolytes such as YSZ or GDC are around 10–13 $\times$ 10^{-6} K^{-1}.[114,193] A mismatch between the TECs of the electrode and the electrolyte heightens the possibility of cracks or delamination during the heating and/or cooling of the cell. Adaption or optimization of the thermal expansion coefficient can be achieved by doping the electrode material or by mixing it with other materials, for example, electrolyte material. The microstructure of the respective fuel electrode has a strong impact on its properties and, therefore, on the performance and degradation behavior of the electrode. Microstructure parameters such as grain size, grain size distribution, tortuosity, percolation, and porosity define the resulting electrode properties/performance. For instance, grain size or its distribution affects the percolation paths of the electrode. A specific porosity is required to ensure unimpeded gas diffusion throughout the electrode toward the electrode/electrolyte interface.[345,346] On the microstructural level, a well-performing electrode exhibits a triple-connecting network of pores as well as electronic and ionic paths.

3.3.2. Electrode materials

3.3.2.1. Ni cermet electrodes. The most commonly used materials for fuel electrodes in SOCs are currently Ni cermets. Adopted from use in SOFCs, the composites of Ni metal and YSZ or GDC are also mainly used as fuel electrodes in high-temperature electrolysis operations. These materials feature a high catalytic activity for electrochemical water reduction and high electronic conductivity, resulting in a good initial performance of Ni-cermet-based fuel electrode SOECs.[347] Properties of the Ni cermets such as the thermal expansion coefficient or electrical conductivity depend on the material fabrication process and its resulting microstructure.[348,349] For the Ni-GDC cermet, first, a TEC of 14.3 $\times$ 10^{-6} K^{-1} was approximated.[350] The measured TEC for a NiO-GDC (50 : 50 wt%) composite in air resulted in 13.5 $\times$ 10^{-6} K^{-1} for a temperature range of 25–1000 °C.[351] The TEC also changes with different amounts of Ni inside the composite material. An increase of Ni from 15 vol% to 30 vol% caused an increase in the TEC from 10.4 $\times$ 10^{-6} K^{-1} to 13.2 $\times$ 10^{-6} K^{-1} at 900 °C.[352] An investigation regarding the influence of porosity and sintering temperature on the resulting TECs and the electrical conductivity of Ni-YSZ (50 : 50 wt%) showed that the thermal expansion of Ni-YSZ changes with the addition of pore former.[349] The initial value of 11.88 $\times$ 10^{-6} K^{-1} increased to 12.23 $\times$ 10^{-6} K^{-1} using 15 wt% of pore former.[349] For a 50% Ni-YSZ material fabricated by citric method TEC of 9.1 $\times$ 10^{-6} K^{-1} was obtained in 5% H_2 + 95% Ar atmosphere.[353]

The electrical conductivity is partly influenced by the particle size of the material, the porosity, the volume fraction of Ni, the distribution of Ni and YSZ or GDC inside the material, and the percolation threshold of Ni (see Section 3.3.2).[348]

For Ni-YSZ prepared by solid-state reaction, the electrical conductivity in air at 25 °C increased with increasing sintering temperature (3936 S cm^{-1} at 1250 °C and 9203 S cm^{-1} at 1450 °C) and decreased with an increasing amount of pore former.[349] The conductivities of Ni-YSZ increased to 25 S cm^{-1} and 4094 S cm^{-1} using 15 wt% of pore former at the respective sintering temperature. The influence of the Ni content in the electrode material on electrical conductivity showed an increase in conductivity from 0.103 S cm^{-1} to 989 S cm^{-1} in hydrogen at 900 °C with a Ni volume change from 15 vol% to 30 vol%.[352] Electrical conductivity stability for Ni-YSZ composites (cermets) in dry and wet reducing atmospheres (combinations of H_2 + diluting gas) could be confirmed for conductivities of 1100–1200 S cm^{-1} at 600 °C.[344] However, a significant conductivity loss was observed in wet atmospheres for temperatures of 800 °C and above and in dry atmospheres for temperatures ≥850 °C.[344] For the electrical conductivity of Ni-GDC composite consisting of 65 wt% NiO and 35 wt% GDC a conductivity of 0.28 $\times$ 10^{-3} S cm^{-1} was seen at 700 °C. This is slightly higher than the conductivity of a NiO-YSZ (50 : 50 wt%) composite (0.17 $\times$ 10^{-5} S cm^{-1}).[354] The electrical conductivity of NiO-GDC cermets in hydrogen at 610 °C could be increased with Cu doping from 2.4 $\times$ 10^{-3} S cm^{-1} (pure NiO-GDC) to 4.5 $\times$ 10^{-3} S cm^{-1} (Cu-doped NiO-GDC).[355] The performance of Ni-YSZ and Ni-GDC fuel electrodes in different SOEC operation modes was tested in several studies. The performance of a Ni-YSZ/YSZ/LSM cell has been investigated with a variation of absolute humidity (AH) in steam electrolysis for 800 °C and 900 °C.[356] A current density of −1.1 A cm^{-2} was achieved under thermoneutral voltage with 82 vol% AH at 800 °C. The authors observed decreasing ASR from 0.69 Ω cm^2 to 0.42 Ω cm^2 with an increase in the absolute humidity from 30 vol% to 82 vol%. The ASR also decreased when increasing temperature up to 900 °C, resulting in values of 0.32–0.20 Ω cm^2 for 30–82 vol% AH. At 900 °C and below thermoneutral voltage with 1.1 V, a current density of −1.4 A cm^{-2} was achieved. The analysis of operating temperature and fuel gas composition on the performance of a Ni-YSZ/YSZ/GDC/LSCF-GDC cell showed an increase in current density at a set voltage of 1.3 V from −0.352 A cm^{-2} to −0.674 A cm^{-2} when the temperature was increased from 700 °C to 800 °C. Moreover, a change in the volume ratio of the gas composition at 750 °C (H_2 + H_2O + CO_2) from 20% H_2 + 0% H_2O + 80% CO_2 to 20% H_2 + 80% H_2O + 0% CO_2 led to an increase in the current density of the cell from −0.445 A cm^{-2} to −0.598 A cm^{-2}.[357] The performance of the Ni-YSZ/YSZ/LSCF-GDC cells in dependence of gas composition resulted ASR values of 0.21 Ω cm^2, 0.22 Ω cm^2, and 0.27 Ω cm^2 when operating the cells at 800 °C in 50% H_2 + 50% H_2O, 25% H_2 + 75% CO_2, and 25% H_2 + 25% CO_2 + 50% H_2O, respectively.[358] For the operation under 25% H_2 + 25% CO_2 + 50% H_2O at 800 °C using a set voltage of around 1.3 V, the authors achieved syngas production rates of ~7 sccm cm^{-2}. Ni-YSZ/YSZ/LSM-YSZ cells exhibited initial cell voltages of 1.42 V and 1.5 V for current densities of −1.5 A cm^{-2} and −2.0 A cm^{-2} at 865–875 °C during co-electrolysis in a 45% H_2O + 45% CO_2 + 10% H_2 atmosphere.[359] The syngas conversion was 45% and 60% for −1.5 A cm^{-2} and −2.0 A cm^{-2}. The effect of Ba infiltration in Ni-YSZ (50 : 50 wt%) on electrode performance was

studied during steam electrolysis, co-electrolysis, and CO_2 electrolysis at 800 °C.[360] The pure Ni-YSZ electrode at a set voltage of 1.3 V achieved current densities of −0.45 A cm^{-2}, −0.27 A cm^{-2}, and −0.36 A cm^{-2} for H_2O electrolysis, co-electrolysis, and CO_2 electrolysis. For the $BaCO_3$-infiltrated Ni-YSZ fuel electrodes, increased current densities of −0.69 A cm^{-2}, −0.55 A cm^{-2}, and −0.62 A cm^{-2} are observed. Moreover, the interfacial polarization resistance between the electrolyte and the electrode was decreased due to the infiltration of Ba in the Ni-YSZ electrode from 1.01 Ω cm^2, 1.59 Ω cm^2, and 1.18 Ω cm^2 to 0.64 Ω cm^2, 0.82 Ω cm^2, and 0.70 Ω cm^2 for H_2O electrolysis, co-electrolysis, and CO_2 electrolysis. The difference between using a Ni-YSZ fuel electrode and a Ni-SDC fuel electrode for CO_2 electrolysis was tested with cells made of Ni-YSZ/YSZ/LSM and Ni-SDC/YSZ/LSM at a set voltage of 1.6 V at 1000 °C.[361] The cells achieved current densities of −1.13 A cm^{-2} and −0.87 A cm^{-2} for Ni-SDC and Ni-YSZ electrodes, respectively, in a 45% CO_2 + 10% H_2 + 45% N_2 atmosphere. Analysis of the polarization resistance in gas atmospheres with 25% and 45% CO_2 resulted in R_P values for Ni-SDC for both gas mixtures around 0.17 Ω cm^2, whereas the R_P values for Ni-YSZ were 0.46 Ω cm^2 and 0.53 Ω cm^2 in 25% and 45% CO_2 respectively. The performance of a Ni-GDC (65 : 35 wt%)/YSZ/GDC/LSCF cell configuration under steam and co-electrolysis operation was examined at a set voltage of 1.5 V.[362] Current densities in steam electrolysis reached −1.31 A cm^{-2} at 900 °C and −0.41 A cm^{-2} at 750 °C, while the corresponding R_P increased from 0.061 Ω cm^2 to 0.31 Ω cm^2 with decreasing temperature. The current density value for co-electrolysis at 900 °C was −1.37 A cm^{-2}, corresponding to an R_P of 0.089 Ω cm^2. The influence of Mo and Au doping on the electrochemical performance of a Ni-GDC (65 : 35 wt%) fuel electrode, a YSZ electrolyte, a GDC barrier layer between the electrolyte and the oxygen electrode, and an LSCF oxygen electrode was analyzed in steam electrolysis. The fuel electrode doped with 3 wt% Mo and Au was tested regarding its performance with a pre-reduced fuel electrode in different pH_2O/pH_2 ratios. The resulting polarization resistances at 900 °C for a pH_2O/pH_2 of 1, 2.3, and 9 for a pure Ni-GDC fuel electrode were 1.36 Ω cm^2, 1.53 Ω cm^2, and 1.64 Ω cm^2, respectively. Doping with 3 wt% Mo and 3 wt% Au led to a decrease of R_P to values of 0.34 Ω cm^2, 0.34 Ω cm^2, and 0.36 Ω cm^2. The authors concluded that for H_2O electrolysis, the 3Au–3Mo–Ni-GDC fuel electrode exhibits better performance compared to the undoped material.[347] In addition to cell performance, the performance in a long-term test with the use of an applied NiO contact layer was examined. At a set voltage of 1.3 V at 800 °C, the cells without a NiO contact layer achieved a current density of −0.076 A cm^{-2} in a 50% H_2O + 50% H_2 atmosphere. Using a NiO contact layer for the same cell configuration and under the same experimental conditions, a current density of −0.361 A cm^{-2} was reached. A higher current density of −0.780 A cm^{-2} at 1.3 V and 900 °C was achieved under steam electrolysis with a gas composition of 7% H_2 + 30% N_2 + 63% H_2O.[363]

3.3.2.2. Perovskite-based electrodes. As materials exhibiting MIEC properties, perovskite oxides have received increased attention in recent years with regard to their use in various components of an SOEC, such as the fuel electrode. The reasons for this increased attention as well as their respective crystal structures are outlined in Section 3.2.1. To optimize and enhance the properties with respect to their respective application, the influence of adding dopants, mixing different phases, and infiltration processes is investigated for all of these possible fuel electrodes.

LSCM exhibits a simple perovskite structure with A- and B-site doping of the lattice. It is reported to have excellent redox stability as well as catalytic activity for fuel gases, thus leading to its consideration as a fuel electrode material in SOECs.[364–367] Investigations of $La_{0.75}Sr_{0.25}Cr_{0.5}Mn_{0.5}O_{3-\delta}$ (LSCM) as a fuel electrode material in H_2O electrolysis[366,368] and co-electrolysis[365] have already been carried out.

The average thermal expansion coefficient of LSCM in a temperature range of 64–956 °C is 9.3 × 10^{-6} K^{-1}.[369] The investigation of the electrical conductivity in air and 5% H_2 at different temperatures showed an electrical conductivity of LSCM is 7.7 S cm^{-1} in air at 320 °C, and 1.4 S cm^{-1} in 5% H_2/Ar.[369] With an increased temperature of 900 °C, the values increased to 38.6 S cm^{-1} in air and 1.49 S cm^{-1} in 5% H_2. In a wet 5% H_2 atmosphere at 900 °C, an electrical conductivity of 0.95 S cm^{-1} was measured for LSCM.[370] The authors achieved an increase in conductivity in wet 5% H_2 to 1.66 S cm^{-1} by doping the LSCM electrode with Ce. Work on Sc doping in LSCM ($La_{0.75}Sr_{0.125}Ce_{0.125}Cr_{0.5}Mn_{0.5}O_{3-\delta}$ – LSCMS) and its impact on the electrical conductivity in 5% H_2 + 95% Ar at 700 °C showed that doping with Sc leads to a decrease in electrical conductivity from 0.639 S cm^{-1} to 0.185 S cm^{-1}.[368] Additionally, doping LSCM with Sc influences the polarization resistance R_P of the electrode, which was tested at 700 °C and 1.8 V in a mixture of 5% H_2O + 95% Ar. Adding Sc to the material reduces the R_P from 9 Ω cm^2 (LSCM) to 6.5 Ω cm^2 (LSCMS). Performance analysis of LSCM electrodes in co-electrolysis mode at 800 °C and OCV in different ratios of H_2O and CO_2 revealed that the polarization resistance increases with increasing steam content from 21.49 Ω cm^2 (20% H_2O + 80% CO_2) to 22.17 Ω cm^2 (60% H_2O + 40% CO_2).[365] The same observation was made while testing the material at 800 °C with a constant current of −0.12 A cm^{-2} using different steam concentrations.[366] In addition, the study results underline that alongside the polarization resistance, the maximum current density is also dependent on the respective steam content. The steam electrolysis experiments at 850 °C under ~1.6 V showed that an increase in the steam content from 20 vol% AH to 80 vol% AH leads to a change in the current densities from −0.431 A cm^{-2} to −0.593 A cm^{-2}.[366,367] The maximum current densities of LSCM fuel electrodes for CO_2 electrolysis and co-electrolysis (60% H_2O + 40% CO_2) at 800 °C under a voltage of 2 V achieved were −0.18 A cm^{-2} and −0.23 A cm^{-2} for CO_2 electrolysis and co-electrolysis, respectively.[365] A comparison of the maximum current density for LSCM and Sc-doped LSCM electrodes at 700 °C and 2 V for steam electrolysis (5% H_2O + 5% H_2 + 90% Ar) showed current densities of −0.4 A cm^{-2} and −0.75 A cm^{-2} for LSCM and LSCMS.[368] The authors also investigated the hydrogen production rate using the same temperature and voltage, only varying the gas composition. They obtained hydrogen production rates of 0.28 ml min^{-1} for LSCM and 1.2 ml min^{-1} for LSCMS in a 5% H_2O + 95% Ar

atmosphere and similar results for 5% H_2O + 5% H_2 + 90% Ar.[368] For the LSCM electrode, a hydrogen production rate of 561 ml cm^{-2} h^{-1} at 850 °C and a voltage of 1.6 V with 80 vol% AH were achieved.[367]

Fuel electrodes based on $LaFeO_{3-\delta}$ perovskite oxide are particularly investigated with regard to their application in SOECs for electrolysis using CO_2-containing fuels. LSFM-based fuel gas electrodes are particularly suitable for CO_2 electrolysis or co-electrolysis and exhibit a high CO_2 selectivity and resistance to C deposition during electrolysis operation.[371,372] Pure LSFM electrodes of different stoichiometries were investigated and the authors concluded that the performance of $LaFeO_{3-\delta}$ perovskite-based electrodes could be optimized by doping with Sr and Mn.[372] LSFM exhibits a TEC of 10.9–12.3 × 10^{-6} K^{-1} between 30 °C and 1000 °C in air[373] and 18.7 × 10^{-6} K^{-1} in H_2.[374] The maximum conductivity of $La_{0.6}Sr_{0.4}Fe_{0.8}Mn_{0.2}O_{3-\delta}$ observed in air at 800 °C was in the range of 35.24 S cm^{-1} (ref. 375) to 50.3 S cm^{-1}.[374] The performance of LSFM fuel electrodes in CO_2 electrolysis and co-electrolysis operation was analyzed in several publications.

The cell composed of LSFM/LSGM/BLC ($Ba_{0.6}La_{0.4}CoO_{3-\delta}$) at 1.6 V in 50% CO_2 + 1% CO + 49% Ar showed the best performance so far for $La_{0.6}Sr_{0.4}Fe_{0.8}Mn_{0.2}O_{3-\delta}$. With this material, current densities of −0.28 A cm^{-2} and −0.52 A cm^{-2} were achieved at 800 °C and 900 °C. The CO_2 reduction rate at 900 °C was 153 μmol cm^{-2} min^{-1}.[372] The performance of a composite fuel electrode consisting of $La_{0.6}Sr_{0.4}Fe_{0.8}Mn_{0.2}O_{3-\delta}$ and $CuFe_2O_4$ (CuF) in a ratio of 1 : 1 in co-electrolysis was analyzed using the cell configuration of LSFM-CuF/LSGM/BLC.[371] At a temperature of 800 °C and a voltage of 1.6 V, the authors achieved a maximum current density of around −1.43 A cm^{-2} in 30% CO_2 + 30% H_2O + 40% Ar. The cell performance of an LSFM-GDC (60 : 40 wt%) composite fuel electrode for CO_2 electrolysis was investigated with the LSFM stoichiometry $La_{0.6}Sr_{0.4}Fe_{0.9}Mn_{0.1}O_{3-\delta}$.[376] The authors used symmetrical, YSZ electrolyte-supported cells with a GDC barrier layer and achieved current densities of −1.1 A cm^{-2} at 800 °C and −1.74 A cm^{-2} at 900 °C using a voltage of 2.0 V. The respective polarization resistances were R_P = 0.85 Ω cm^2 (800 °C) and R_P = 0.48 Ω cm^2 (850 °C). At a temperature of 800 °C, they observed a CO production rate of 6.438 ml min^{-1} cm^{-2}.[376,377] Further experiments were conducted in pure CO_2 on the $La_{0.6}Sr_{0.4}Fe_{0.9}Mn_{0.1}O_{3-\delta}$ fuel electrode side at temperatures of 800 °C and 900 °C and a voltage of 1.6 V. In the operating conditions, current densities of −0.335 A cm^{-2} at 800 °C and −0.76 A cm^{-2} at 900 °C could be achieved.[378]

LST has been categorized as a redox-stable perovskite with great potential as an electrode material in SOECs.[379] The material exhibits TEC values of 11–12 × 10^{-6} K^{-1} between 30 °C and 1000 °C.[380,381]

Investigations with regard to the thermal expansion behavior of reduced and non-reduced $La_{0.4}Sr_{0.4}TiO_3$ in different atmospheres between 50 °C and 1000 °C found that the TEC of the material in a 5% H_2 + 95% Ar atmosphere with 11.89 × 10^{-6} K^{-1} is higher compared to the expansion in air of 10.35 × 10^{-6} K^{-1}.[382] Additionally, the authors observed that reducing the material after sintering could reduce the resulting TEC to 11.60 × 10^{-6} K^{-1}.[382] The conductivity of LST also depends on whether the material is in the pre-reduced or oxidized state. Non-reduced LST ($La_{0.2}Sr_{0.8}TiO_{3+\delta}$) reached a conductivity of 0.001 S cm^{-1} in air at 800 °C.[383] The conductivity of reduced LST and iron-doped LST in air and 5% H_2 + 95% Ar at 800 °C achieved conductivities of 0.7 S cm^{-1} and 0.5–0.6 S cm^{-1} in air and 1.1 S cm^{-1} and 1.5 S cm^{-1} in a reducing atmosphere for LST and Fe-LST.[379] In hydrogen, sintered LST has conductivities of 100–500 S cm^{-1} between 700 °C and 1000 °C under 10^{-15} < pO_2 < 10^{-20}.[380] Measured in wet H_2, reduced LSTO reached a conductivity of 30 S cm^{-1} at 700 °C.[384]

To improve the conductivity and the catalytic activity, LST was doped with Ca and Fe.[385] The authors theorized that doping LST on the A-site with Ca should enhance the electrical conductivity of the perovskite oxide. In addition, substituting Ti ions with Fe on the B-site of the crystal lattice of strontium titanate should lead to high mixed ionic–electronic conductivity and high catalytic activity. The investigations revealed a dependency of the conductivity on the Ca amount within the $La_{0.2}Sr_{0.25}Ca_xTi_{0.95}Fe_{0.05}O_{3-\delta}$ material. They determined a maximum conductivity of 5.5 S cm^{-1} at 850 °C under 97% H_2 + 3% H_2O with an optimum calcium content of x = 0.45 mol%.[385]

The combination of titanate and ceria ($La_{0.35}Sr_{0.65}TiO_{3-\delta}$–$Ce_{0.5}La_{0.5}O_{2-\delta}$) was examined as a fuel electrode material in a reversible SOC concerning the material's conductivity.[386] The authors discovered that the electrode's conductivity and, in turn, its performance is strongly dependent on the prevailing oxygen partial pressure as well as on the H_2O/H_2 ratio of the respective gas composition.[386] ASRs of 0.2–0.28 Ω cm^2 were achieved under a constant polarization loss of 0.1 V in pH_2O = 0.5–0.9 using a mixture of LST with $Ce_{0.5}La_{0.5}O_{2-\delta}$ as a fuel electrode.[386] A composite electrode of LST ($La_{0.2}Sr_{0.8}TiO_{3+\delta}$)-SDC in CO_2 electrolysis operation was investigated using a symmetrical cell with a YSZ electrolyte.[387] To enhance CO_2 selectivity and electrode performance, the LST was doped with Mn ($La_{0.2}Sr_{0.8}Ti_{0.9}Mn_{0.1}O_{3+\delta}$). They observed a decrease in the polarization resistance R_P of the fuel electrode with increasing pH_2 (10% to 100%). The R_P is reduced from 28 Ω cm^2 to 9 Ω cm^2 for the LST-SDC composite and from 4 Ω cm^2 to 2 Ω cm^2 for the manganese-doped LSTM-SDC fuel electrode. The authors achieved current densities of −0.12 A cm^{-2} and −0.25 A cm^{-2} for LST- and LSTM-based fuel electrodes during operation at 800 °C under 2.0 V. The resulting CO production rates were 0.1–0.2 ml cm^{-2} min^{-1} and 1.1 ml cm^{-2} min^{-1},[387] respectively. Similar experiments using a cell configuration of LST-SDC/YSZ/LSM-SDC achieved a current density of −0.125 A cm^{-2} during CO_2 electrolysis at 700 °C under 2.0 V.[384] The CO production rate of 1.23 ml cm^{-2} min^{-1} achieved in this work was higher than the LSTO-based fuel electrode results.

SFM, $Sr_2Fe_{1.5}Mo_{0.5}O_{6-\delta}$, is a double perovskite, the properties of which are described in detail in chapter 3.2.1.2. It is a mixed ionic–electronic conductor, which also has high catalytic activity.[388] The electrical conductivity of SFM ($Sr_2Fe_{1.5}Mo_{0.5}O_{6-\delta}$) measured at 800 °C was 32 S cm^{-1} in H_2 and 14.90 S cm^{-1} at 750 °C in air,[180] which is higher than the conductivity of other ceramics such as LSCM or LSTO. Under

a 50% CO_2 + 50% CO atmosphere at 750 °C, SFM shows an electrical conductivity of 19 S cm^{-1}.[182] The conductivity measured at 800 °C decreased from 15.9 S cm^{-1} to 8.3 S cm^{-1} by doping with antimony in 5% H_2 + 95% Ar.[389] Adding Mn to SFM, on the other hand, leads to a decrease in conductivity in air at 800 °C and an increase from 16 S cm^{-1} to 25 S cm^{-1} in a 5% H_2 + 95% Ar atmosphere for $Sr_2Fe_{1.4}Mn_{0.1}Mo_{0.5}O_{6-\delta}$.[390] The TEC value of SFMO was found to be around 14.5 × 10^{-6} K^{-1} in the temperature range of 200–760 °C in air.[174] Regarding the use of SFM fuel electrodes in steam electrolysis, several experiments were conducted using symmetrical SFM/LSGM/SFM cells.[179] At 1.3 V and with 40 vol% absolute humidity (AH), current densities of −0.48 A cm^{-2} and −0.59 A cm^{-2} were achieved at 800 °C and 900 °C, respectively. Changing the AH from 20 vol% to 60 vol% leads to an improvement in current density from −0.38 A cm^{-2} to −0.88 A cm^{-2} at 900 °C. The polarization resistance under OCV conditions with 60 vol% AH R_P decreases from 0.83 Ω cm^2 to 0.26 Ω cm^2 going from 800 °C to 900 °C. The authors reached a hydrogen production rate of 380 ml cm^{-2} h^{-1} at 900 °C using a set voltage of 1.3 V and 60 vol% AH.[179] The performance of a symmetrical electrolyte (YbScSZ)-supported cell with an SFM electrode tested in steam (90% H_2O + 10% Ar) and co-electrolysis (75% H_2O + 25% CO_2) at 900 °C with a set voltage of 1.3 V resulted in current densities of −1.4 A cm^{-2} and −1.1 A cm^{-2}, respectively.[182]

Because the electrical conductivity of pure, single-phase SFM at 800 °C in hydrogen is only 10 S cm^{-1}, the necessity of an enhanced SFM fuel electrode for steam electrolysis was proposed.[391] Likewise, the performance in terms of the electrode polarization resistance and current densities achieved at 800 °C and 1.3 V with values of 0.65 Ω cm^2 and −0.48 A cm^{-2} indicate the need for electrode material optimization. The authors suggest that one way of increasing the current density and reducing the polarization resistance of the electrode is to introduce nanocatalysts through infiltration processes or *in situ* exsolution into the material. Doping the B-site of the perovskite oxide with transition metal elements is one example. After *in situ* reduction, those elements form exsolved metal catalysts on the surface of the base perovskite grains and also lead to a change in the oxygen vacancy concentration. Using the exsolution process to enhance the performance of SFM-based fuel electrodes is more frequently investigated under fuel cell mode. In the case of SFM-based fuel electrodes in electrolysis operation, only a few publications are available. Here, doping SFM with Ni and/or additional Fe sources such as cobalt was studied concerning the effect of exsolution.[181,392–394] In one study, the SFM double perovskite was doped with nickel to obtain the stoichiometry $Sr_2Fe_{1.3}Ni_{0.2}Mo_{0.5}O_{6-\delta}$.[391] The authors subsequently examined the performance and degradation behavior of cells with two different fuel electrodes: one consisting of pure SFM-SDC and one of the SFMNi-SDC composite in an atmosphere of 42% H_2O + 58% H_2. In both cases, the ratio between the perovskite oxide and SDC was 60 : 40 wt%. At 850 °C and a set voltage of 1.3 V, a current density of −0.64 A cm^{-2} was achieved for the pure SFM-based electrode. For $Sr_2Fe_{1.3}Ni_{0.2}Mo_{0.5}O_6$, the current density increased to −1.26 A cm^{-2} and the resistance at the OCV was reduced from 0.44 Ω cm^2 to 0.21 Ω cm^2.[391] Another study investigated the performance of a $Sr_{1.9}Fe_{1.5}Ni_{0.1}Mo_{0.4}O_{6-\delta}$ (SFMN) based fuel electrode for CO_2-electrolysis in electrolyte-supported cells composed of SFMN-SDC ($Sm_{0.2}Ce_{0.8}O_{1.9}$)/SDC/YSZ/LSM-YSZ.[392] After annealing at 800 °C in hydrogen, the exsolution of Ni–Fe nanoparticles in the SFMN-SDC composite electrode was observed, which enhanced the chemical adsorption and surface reaction kinetics of the fuel electrode. Moreover, a stability test of the cell for 500 h in CO_2-electrolysis mode at 800 °C and 1.3 V showed a relatively stable current density of −1.1 A cm^{-2}. Only a slight current loss at the beginning of the measurement was detected, which the authors ascribe to an initial oxidation of the Ni–Fe particles.[392] The use of SFM perovskites with exsolved nanoparticles can therefore improve the catalytic activity of the fuel electrode material. However, the lack of experimental data regarding the long-term stability in electrolysis operation and reversibility of the exsolution process needs to be addressed to evaluate this modification process in more detail. SFM was also doped with Ba to obtain a double perovskite electrode material with improved electrochemical properties.[395] As a result of doping the A-site cations with the larger Ba cations, the authors expected an enhanced oxide ion migration due to the expansion of the unit cell. In this publication, electrochemical measurements were performed on half-cells with 0.2 mol% barium-doped SFM as an electrode ($Ba_{0.2}Sr_{1.8}Fe_{1.5}Mo_{0.5}O_{6-\delta}$). The amount of 2 wt% Ba agrees with the results of previous experiments, indicating that this Ba content is advantageous in terms of electrical conductivity and power density.[396,397] To prevent a reaction between the YSZ electrolyte and the electrode, a protective SDC layer was applied between the electrolyte and electrode. From their experiments, the authors conclude that the optimal calcination temperature for Ba-doped SFM is 1100 °C, thus avoiding the formation of secondary phases like $SrMoO_4$ during calcination. Furthermore, the authors reported that SOEC operation with a gas composition containing 20% H_2O + 80% H_2 led to a maximum current density of −0.18 A cm^{-2} at a set voltage of 0.2 V and −0.36 A cm^{-2} for 0.4 V.[395]

SFM-SDC fuel electrodes in a symmetrical LSGM electrolyte-supported cell in co-electrolysis operation were investigated at 850 °C using a set voltage of 1.3 V.[180] A current density of −0.734 A cm^{-2} and a polarization resistance of 0.48 Ω cm^2 at OCV and 850 °C were achieved in a 16% H_2O + 16% CO_2 + 20% H_2 + 48% N_2 atmosphere. The authors produced syngas with a corresponding CO_2 conversion rate of 0.58 and an ideal H_2/CO ratio of approx. 2.[180] The electrochemical performances of a pure SFM, an Mn-doped SFM, and an SFM-SDC composite fuel electrode were compared in an atmosphere of 50% CO + 50% CO_2 at 800 °C.[390] The authors obtained polarization resistances of 1.12 Ω cm^2, 0.60 Ω cm^2, and 0.50 Ω cm^2 for SFM, SFMMn, and SFMMn-SDC. Further investigations were conducted using an SFMMn-SDC fuel electrode combined with an LSCF-SDC oxygen electrode and an LSGM electrolyte. Current densities of −1.80 A cm^{-2} and −1.35 A cm^{-2} were achieved at 850 °C and 800 °C, respectively, using a set voltage of 1.5 V in pure CO_2.[390]

The double perovskite SFN ($Sr_2FeNbO_{6-\delta}$) and the simple perovskite $SrFe_{0.9}Nb_{0.1}O_{3-\delta}$ have been investigated several times as an electrode material for SOFCs.[398,399] The electrical

conductivity of an SFN double perovskite at 850 °C in air is low with 0.05 S cm^{-1}.[400,401] The conductivity increases to 2.39 S cm^{-1} (@900 °C)[402] and 2.215 S cm^{-1} (@850 °C)[400] when the atmosphere is changed to the reducing conditions of 5% H_2 + 95% Ar and 80% H_2O + 20% H_2. The effect of Mn doping into the SFN double perovskite on the conductivity in air and in 80% H_2O + 20% H_2 atmosphere was investigated.[401] Substituting 50% Fe with Mn leads to an electrical conductivity value of 0.5 S cm^{-1} in oxidizing and reducing atmospheres. With an increasing amount of Mn, a maximum conductivity of 1.37 S cm^{-1} in air was reached for $Sr_2MnNbO_{6-\delta}$. The authors concluded that through doping Mn in the B-site of the SFN double perovskite the conductivity increases in air but decreases under reducing atmospheres.[401] The observed increase in conductivity in air through doping the B-site of SFN was confirmed by other authors as well.[398] They achieved a maximum conductivity of 5.7 S cm^{-1} at 800 °C for a Co-doped $Sr_2Fe_{0.1}Co_{0.9}NbO_6$. The electrical conductivity of the simple SFN perovskite $SrFe_{0.9}Nb_{0.1}O_{3-\delta}$ was found to be around 30 S cm^{-1} (ref. 399) in a reducing atmosphere. Cu doping of SFN in a 5% H_2 + 95% Ar atmosphere achieved the highest conductivity of 30–60 S cm^{-1} between 300 °C and 700 °C for $SrFe_{0.8}Cu_{0.1}Nb_{0.1}O_{3-\delta}$.[399] The thermal expansion of pure SFN and a Mo-doped SFN double perovskite in air and in 5% H_2 + 95% Ar was investigated in the temperature range of 30–1000 °C.[403] The authors obtained average TEC values for SFN and SFNMo of 11.3 × 10^{-6} K^{-1} and 12.5 × 10^{-6} K^{-1} in air and 12.6 × 10^{-6} K^{-1} and 13.5 × 10^{-6} K^{-1} in 5% H_2 + 95% Ar. The doping of Mo into the SFN double perovskite lattice leads to an increase in thermal expansion in air as well as in a reducing atmosphere.[403] The polarization resistances of the electrode at 800 °C in air for pure SFN and Mo-doped SFN using an LSGM electrolyte in air were 1.72 Ω cm^2 and 0.469 Ω cm^2 for SFN and SFNMo, respectively. The R_P values measured in reducing atmospheres (5% H_2 + 95% Ar) were 2.97 Ω cm^2 and 0.353 Ω cm^2 for SFN and SFNMo. Independent of the atmosphere, lower R_P values were measured for SFN doped with Mo.[403]

Only a limited number of studies deal with the use of SFN double perovskite-based fuel electrodes in SOECs.[400] The electrochemical performance of an SFN-YSZ (80 : 20 wt%) composite fuel electrode was compared to a state-of-the-art Ni-YSZ fuel electrode in steam electrolysis operation in a cell composed further of a YSZ electrolyte and an LSM-YSZ oxygen electrode. Applying a set voltage of 1 V at 850 °C in an 80% H_2O + 20% H_2 atmosphere, a total resistance of 2.84 Ω cm^2 was obtained for the SFN-YSZ fuel electrode, which is significantly lower compared to the resistance of the Ni-YSZ fuel electrode (21.42 Ω cm^2). The authors concluded that the SFN-YSZ fuel electrode showed a better electrochemical performance compared to the Ni-YSZ electrode in SOEC operation under the same conditions. In addition, they observed the high catalytic activity of SFN for H_2O dissociation. Through chemical absorption on the SFN surface, the reaction process was accelerated and the energy barrier for charge transfer was lowered.[400]

PBFM ($(PrBa)_{0.95}(Fe_{0.9}Mo_{0.1})_2O_{5+\delta}$) is an A-site layered double perovskite with the general stoichiometry of $LnBaM_2O_{5+\delta}$ (Ln = lanthanides, M = transition metals) and has great potential as a fuel electrode material in SOECs for steam electrolysis.[404] The crystal structure can be described as the stacking of transition metal oxide layers in between Ba oxide and lanthanide oxide layers: (BaO)-(MO_x)-(LnO_δ)-(MO_x)-(BaO).[405–407] Through this lattice structure, two-dimensional oxygen diffusion *via* oxygen vacancies formed inside the three inside layers can be observed.[405] In most literature studies, praseodymium is used as the lanthanide dopant. Here, the Pr^{3+} and Ba^{2+} ions are ordered in alternating layers in the (001) direction.[407] This stacking of layers results from the difference in the ion sizes of barium (135 pm) and praseodymium (109 pm). Most of the oxygen vacancies inside the layered structure are located at the lanthanide oxide layer, leading to a high tendency to form ordered structures under changing atmospheres (pO_2 decrease).[407] Due to this structure, higher conductivities and better electrochemical performance can be obtained compared to simple perovskites.[405,407] PBFM reaches high electrical conductivities of 217 S cm^{-1} and 59.2 S cm^{-1} in air and 5% H_2 + 95% Ar at 800 °C.[407] A TEC of 11.96 × 10^{-6} K^{-1} was measured for PBFM.[407] The performance of a composite PBFM-SDC (70 : 30 wt%) fuel electrode was also tested in steam electrolysis.[404] The authors investigated the dependence of the resulting current density and the electrode polarization resistance on the operating temperature at a set voltage of 1.3 V in a 3% H_2O + 97% H_2 atmosphere. They observed an increase in current density from −0.28 A cm^{-2} to −0.82 A cm^{-2} with a simultaneous decrease in R_P from 3.34 Ω cm^2 to 0.73 Ω cm^2 as the temperature increased from 750 °C to 850 °C.[404]

3.3.3. Microstructure. To obtain the best possible electrochemical performance over a long period, the microstructure of the electrode (including porosity, pore shape, pore size distribution, grain size, and percolation) must be optimized concerning the application of the cell (SOFC/SOEC). The percolation threshold of Ni inside the Ni cermet electrode is required to ensure its electrical conduction. The percolation threshold, and therefore the electrical conductivity, can be affected by porosity and the microstructure of the composite. The threshold is described by the minimum Ni content required in the cermet to obtain a continuous Ni network leading to a sufficiently high conductivity. In general, the conductivity of the Ni cermet increases with increasing Ni content inside the material. The percolation limit for a Ni-YSZ composite electrode was observed to be approximately 30 vol% of Ni.[408] The authors report that cermets with a Ni content below 25 vol% have low electrical conductivities.[408] The percolation limit for Ni-YSZ cermets prepared by solid-state reaction and liquid dispersion methods with 30 vol% Ni was reduced to a value of 10–20 vol% if an electroless coating technique was used to fabricate the Ni cermet.[409] Good adhesion between the Ni and the YSZ ceramic is necessary to provide sufficient mechanical strength as well as sufficient charge transfer.

The electrode porosity must ensure good gas diffusion in addition to sufficient percolation for conductivity and mechanical stability. Compared to the gas diffusion through the fuel electrode in SOFC operation, the transport of a larger amount of steam through the electrode material during steam electrolysis is more complex.[410] The values considered to offer

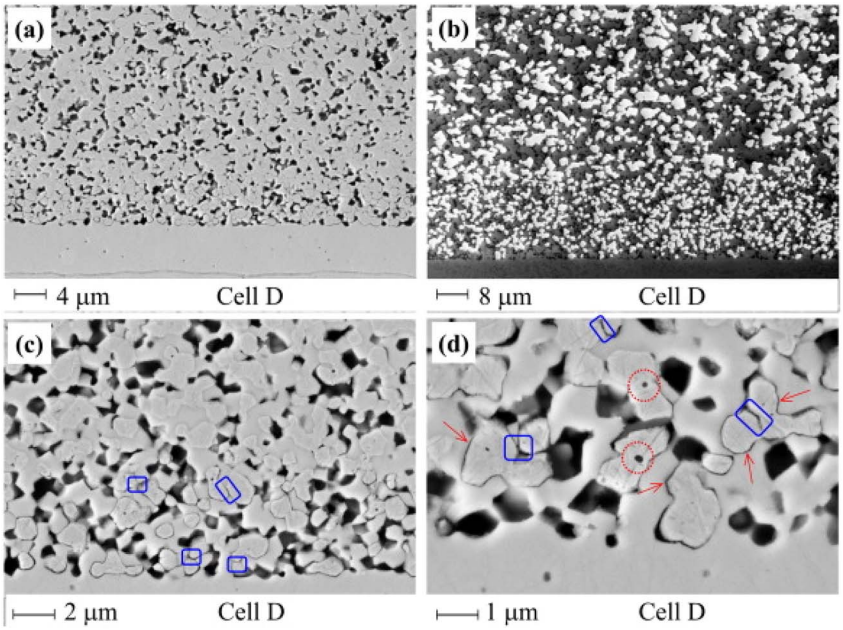

Fig. 21 SEM images of the electrode/electrolyte interface of a Ni-YSZ fuel electrode-supported cell with a fine microstructure tested under electrolysis for 1000 h at −1.25 A cm^{-2} (ref. 413) (a) SEM image of the tested cell, (b) in-lens low-voltage image, (c) and (d) microstructure changes denoted by blue squares for Ni–Ni contact loss, red arrows for Ni-YSZ loss, and red circles for impurities. Reprinted from ref. 413, copyright 2016, with permission from Elsevier.

optimal porosity for fuel electrodes, therefore, vary depending on the operation: 35 vol% for SOFCs and 45 vol% for SOECs.[345,346,411–413]

To increase the porosity, pore formers such as polymethyl methacrylate (PMMA), corn/potato starch, graphite, and carbon black can be introduced into the electrode material. The resulting porosity and performance (electrical conductivity, ohmic resistance) are highly dependent on the pore former used, its particle size, and its shape. Large pores tend to lead to a reduction of the TPB length and a decrease in performance, while very small pores hinder fuel gas diffusion. PMMA used as a pore-forming agent was found to be the most promising in terms of SOEC application.[345] This is due to the uniform pore size distribution, the accelerated charge transfer in the active area due to the generally smaller pores, and the simultaneously sufficient porosity compared to other pore-forming agents.[345,346] Grain size and microstructure changes impact the degradation behavior and electrode performance in the case of Ni-YSZ fuel electrodes.[412,413] The coarser initial microstructure led to Ni loss during SOEC operation at the electrocatalytically active layer. This, in turn, led to a significant decrease in electrode performance. In contrast, electrodes with a finer microstructure exhibit electrode degradation dominated by Ni agglomeration or coarsening. Long-term tests with cells supported by a Ni-YSZ fuel electrode indicate that the Ni loss during SOEC operation is relatively low after 10 700 h for the cells with finely structured electrodes.[412,413] Fig. 21 displays a cross-section of the Ni/YSZ fuel electrode/electrolyte interface using a finer structured electrode after 1000 h operation in electrolysis mode with an applied current density of −1.25 A cm^{-2} in 90% H_2O + 10% H_2. The SEM images show the degradation of the electrode/electrolyte interface only in the form of Ni–Ni and Ni-YSZ contact losses and the segregation of impurities inside the nickel particles.

In contrast, for the electrode with a coarse microstructure, a clear Ni loss at the electrolyte/electrode interface can already be seen after an operating time of 1000 h.[412] These results indicate that the number of TPBs and a higher specific surface

Table 4 Results of cell tests of SOECs with different fuel electrode microstructures (with and without modification) compared with SOFCs under specific operating parameters[413]

Operation mode	Fuel electrode	Degradation rate	Current density	Temperature	Gas composition	Ref.
SOEC	Microstructure modified Ni-YSZ	0.3–0.4% kh^{-1}	−1 A cm^{-2}	800 °C	pH_2O/pH_2 = 0.9/0.1	413
SOEC	Ni-YSZ	2% kh^{-1}	−0.5 A cm^{-2}	850 °C	pH_2O/pH_2 = 0.5/0.5	414
SOFC	Ni-YSZ	<1% kh^{-1}	1 A cm^{-2}	850 °C	—	415
SOEC	Ni-YSZ	6% kh^{-1}	−1 A cm^{-2}	950 °C	pH_2O/pH_2 = 0.9/0.1	414
SOFC	Ni-YSZ	2% kh^{-1}	1.7 A cm^{-2}	950 °C	—	415

area between the two phases for a finer microstructure have a decisive influence. An electrode with a finer microstructure thus mitigates Ni migration by limiting the overpotential at a given current density.[412,413] Matching particle size distributions of the individual electrode components improves the mixing and dispersion of nickel, YSZ, and porosity. Well-mixed and homogeneously distributed phases in the fuel gas electrode can restrict Ni migration through the YSZ backbone.[413] Another possibility for optimizing certain microstructural properties of the Ni-YSZ fuel electrode in terms of long-term stability is to design the electrode with the highest possible density. The densification of the Ni-YSZ electrode enhances the tortuosity of the Ni particles percolation, increases the number of percolating paths, and benefits the Ni-YSZ interface.[413] It was suggested that a suitable choice of the above-mentioned parameters can prevent irreversible degradation during long-term application under a high current and high pH_2O. By optimizing the microstructure and the operating parameters, the authors achieved a significant improvement in the degradation rate. Table 4 shows the results of cell tests for SOECs with and without a modified fuel electrode microstructure as well as results for SOFCs together with their respective operating parameters. Due to the obtained low degradation rate of 0.3–0.4% kh^{-1}, the authors expect a prolonged lifetime of an SOEC with such a modified Ni-YSZ fuel electrode microstructure of more than five years under cell operation near the thermoneutral point.[413] The design of the electrode microstructure is expected to depend highly on the desired application. For fuel electrodes applied in SOECs at high current densities, a finer particle size and a denser structure are most suitable. If, however, only low current densities are required or the operation takes place at very high temperatures, an electrode with a coarser microstructure is sufficient and more cost-effective.[413]

3.3.4. Degradation. The degradation behavior of fuel electrodes depends on the electrode's microstructure and operating parameters, such as current density, polarization/overpotential, gas humidity, temperature, and the local redox potential of the respective gas composition.[52,411,412,416,417] Depending on the applied temperature, particle growth, agglomeration and cation interdiffusion between electrode and electrolyte already occur through the sintering step during cell manufacturing and influence the electrode's initial microstructure and therefore the performance.[418] It has been found that the degradation rates in SOEC operation, especially at higher current densities, are higher compared to the degradation of the same cells operated in fuel cell mode if a state-of-the-art Ni cermet is used as a fuel electrode.[419] Besides the different operating conditions in SOEC compared to SOFC mode, the different polarization of the fuel electrode also affects the degradation of the fuel electrode. The altered polarization leads to changes in the interface's microstructure, active site length, and local composition. Depending on the applied current, a different degree of degradation and diffusion at the electrode/electrolyte interface can be observed.[418] Taking into account the fact that SOECs need to be operated at high temperatures and combined with different gas compositions and high current densities, the development of alternative fuel electrodes is necessary.[343] Despite their good initial performance for high-temperature electrolysis, Ni cermets used as fuel electrodes exhibit relatively poor stability in long-term operation. Further investigations of Ni-YSZ fuel electrodes in SOECs confirm this conclusion, describing the high degradation of this electrode and its resulting low level of long-term stability in electrolysis operation.[52,343,417,420–423] The mechanisms behind the degradation of the Ni-YSZ fuel electrode are highly complex and yet to have been fully understood.[411] There is therefore a need for alternative materials and/or microstructures[413] which are better suited for the respective electrolysis.

3.3.5. Ni cermets. Previous studies on the degradation behavior of the Ni-YSZ fuel electrode revealed two predominant degradation mechanisms during electrolysis that lead to microstructural changes: coarsening/agglomeration of the Ni particles, and the migration of nickel.[52,412,417,424] Nickel serves as both a catalyst and an electron conductor in the electrode, but it also exhibits high mobility in the temperature range of 650–950 °C. Changes in local Ni concentrations or the dislocation of nickel particles within the electrode layer, therefore, have a strong influence on electrode performance. The coarsening or agglomeration of Ni particles takes place independently of the operating mode and polarization.[412,417] Particle agglomeration is attributed to an Ostwald ripening process at high gas humidity.[52] This process aims at minimizing the surface free energy, with larger particles consequently growing at the expense of smaller ones. This is caused by a concentration gradient resulting from the higher equilibrium vapor pressure on the smaller particle. When a small particle is located near a larger particle, a diffusion of mass can develop toward the bigger one. The mass transport here can take place either through surface diffusion or *via* the gas phase. Another mechanism leading to the coarsening of Ni particles is their high mobility based on the formation of $Ni(OH)_x$. Due to the particle growth, there is a loss of contact between the Ni particles. Therefore, the percolating network of nickel particles is reduced, resulting in a decrease in conductivity if the percolation threshold is reached. An initially rapid decrease of conductivity can be observed followed by a more gradual reduction until it reaches a plateau.[344] In addition, the increasing particle size and, therefore, the decreasing number of particles results in a reduction of the three-phase boundary length and of the porosity at the electrode/electrolyte interface.[52,344,411] The migration of nickel by different processes is suggested to occur only at current densities greater than 0.5–1 A cm^{-2}.[411] At low current densities of −0.25–0.25 A cm^{-2} (≡low overpotential), no displacement processes of the Ni particles are observed. Ni migration occurs irrespective of Ni growth and the loss of contact between Ni particles. At present, there are two different hypotheses discussed in the literature to describe the migration of nickel particles during electrolysis and their underlying mechanisms.[52,411,412,417,424] The irreversible loss of nickel at the catalytically active electrolyte/electrode interface is one of the main processes leading to the degradation of the fuel gas electrode and, therefore, to a degradation in the performance of the SOEC.[52,417] It was found that the migration of nickel particles in an SOEC is favored compared to an SOFC.[412]

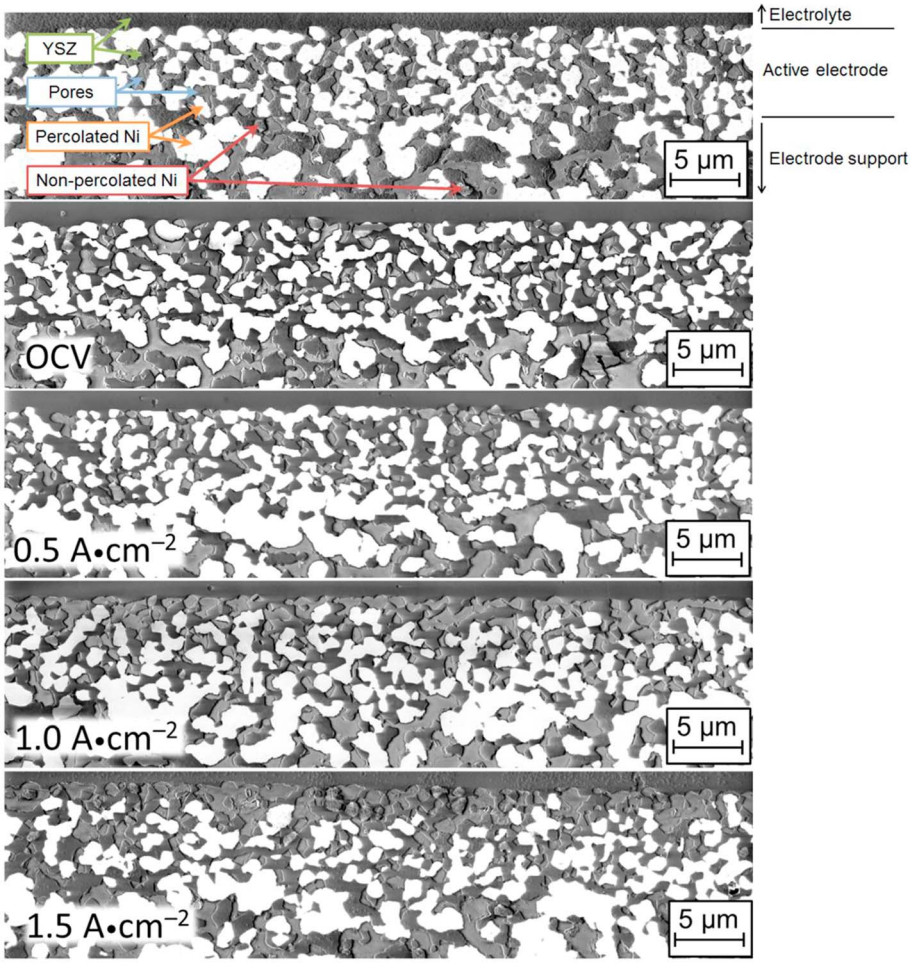

Fig. 22 SEM images of fuel electrode/electrolyte interfaces of fuel electrode-supported cells: pristine (as-reduced) and after operation at 800 °C for 1000 h in 80% H_2O + 20% H_2 at OCV and three different current densities (−0.5 A cm^{-2}, −1.0 A cm^{-2}, and −1.5 A cm^{-2}).[52] Reprinted from ref. 52, copyright 2018, with permission from Elsevier.

At operating temperatures of 800–900 °C, the Ni particles migrate from the electrolyte/electrode interface toward the electrode substrate, resulting in a loss of nickel in the active layer near the electrolyte. The Ni particles move against the H_2O gradient (pO_2).[411,412] This relocalization of the Ni particles leads to a reduction of percolating nickel and an increase in the porosity of the active layer of the electrode.[417] Consequently, a shift and reduction of the reaction zone/TPB and, therefore, an increase of electrolyte thickness occurs, which ultimately leads to higher ohmic resistances of the cell.[52,425] The decline of the active area of the electrode and its dependency on the applied current density is shown in Fig. 22. The number of non-percolating Ni particles and the porosity at the electrode/electrolyte interface increase with higher current densities.[52]

Ni migration toward the fuel electrode substrate is only observed at gas humidities of ≥80% and temperatures of ≥800 °C.[52] If the operating temperature of the SOEC is 950 °C, the direction of Ni migration changes and the particles migrate toward the electrolyte. The migration of the particles takes place along the H_2O gradient (pO_2).[411] This also leads to a loss of electrode performance, since the porosity near the electrolyte/electrode interface is clogged and the TPB is therefore reduced.[52] The displacement of Ni particles toward the electrolyte at a temperature of 950 °C during electrolysis operation corresponds with observations of Ni migration of an SOFC stack operated at 700 °C for a long period (>10 years).[411]

The theories presented below are intended to explain and reconcile the above observations. However, the underlying mechanisms of Ni migration are not yet fully resolved.[52,411,412] The various literature sources at least agree that the locally prevailing polarization, or the local overvoltage/overpotential, plays a major role in this process.[52,412,417,424] Sun *et al.*[424] found that the degradation rate of an SOEC generally increases with increasing polarization of the fuel electrode. There are different hypotheses as to how the particles detach from the composite material and thus migrate. Trini *et al.*[417] suggest that the contact angle, which changes under different polarization, is the driving force for the release of the Ni particles from the composite. According to their hypothesis, the strongly polarized zone close to the electrolyte leads to a high contact angle between Ni/YSZ and a de-wetting of the material occurs. The nickel particles then move from the area at the electrolyte/

electrode interface with a low pO_2 towards higher pO_2 values at the outer and less strongly polarized areas of the electrode. The less strong polarization in these areas results in a lower contact angle between Ni and YSZ, and there is better wetting of the material between them.[417] Sun *et al.* also describe the tendency of Ni to detach from YSZ during strong (cathodic) polarization due to de-wetting processes and to migrate toward the less polarized regions of the electrode substrate.[424] High cathodic polarization results in an accumulation of vacancies, which in turn leads to a decomposition of the Ni/YSZ interface and thus to a dissolution of Ni particles from the composite. The migration of nickel is explained here by the formation of gaseous $Ni(OH)_x$ species due to the influence of the partial vapor pressure.[412] Hoerlein *et al.* suggest that volatile nickel hydroxides under cathodic polarization follow the gradient of $Ni(OH)_x$ activity from non-percolating to percolating nickel.[52] Mogensen *et al.* suggest that Ni migration is driven by electric polarization by the surface diffusion of $Ni(OH)_x$ species below 800 °C and by gaseous nickel hydroxides at temperatures ≥900 °C. The main parameters affecting migration are the local overpotential of the Ni particles, the local pH_2O, and the activity of the $Ni(OH)_x$ species. In the case of an SOEC with an operating temperature of 800–900 °C, a strong cathodic overpotential leads to a loss of contact between polarized Ni particles and YSZ. In the case of simultaneous contact loss among Ni particles, the isolated Ni particles adopt the potential of the local gas composition.[411] The local pH_2O around the particles becomes higher, as more H_2O molecules migrate towards the electrolyte without coming into contact with the polarized Ni particles at the TPB. The pH_2O at the active TPB is minimized. The activity of the $Ni(OH)_x$ species is proportionate to the potential and is lowest where the potential is also lowest. The dissolved Ni particles thus migrate locally towards the region with a lower pH_2O (the new active TPB) and deposit on the polarized nickel at the displaced TPB. The nickel hydroxides thus seem to migrate against the electrochemical potential or the global pH_2O/pO_2 gradient of the fuel gas electrode.[411]

Degradation processes also occur due to the segregation of impurities at the TPB. Ni-YSZ composites almost always have thin monolayers of impurities or segregated components at YSZ surfaces, Ni-YSZ interfaces, or grain boundaries.[411] Impurities can be introduced into the system by raw materials, the gas flow, or evaporating species from the interconnects and sealings. As an example of an observed process, the precipitation of SiO_2 at the TPB was reported. A possible source of Si-containing fuel gas impurities are the vaporizers made of glass containers for water vapor generation. Carbon deposition has also been observed when carbon-containing reactant gases were used.[52,411]

Several stability studies on Ni cermet fuel electrodes used in SOEC operation have been carried out.[79,426–428] The degradation of a Ni-YSZ/YSZ/GDC/LSCF cell in steam electrolysis was carried out at a temperature of around 780 °C.[426] The authors used a reducing atmosphere with an AH of 80 vol% and operated the cell for 9000 h at a current density of −1.0 A cm^{-2}. During operation, they observed a voltage degradation rate of 3.8% kh^{-1}. After cell operation, the microstructure was analyzed by SEM images. The authors detected a weakened contact between the electrolyte and the hydrogen electrode and varying surface roughness of the Ni particles. No impurity segregation was observed at the interface. An SOEC stack consisting of Ni-YSZ/YSZ/GDC/LSCF cells was tested under 50% humidified H_2 at a current density of −0.5 A cm^{-2} at 800 °C for 2300 h, followed by 1800 h at 700 °C.[79] A voltage and an ASR degradation rate of 0.7% kh^{-1} and 10.1% kh^{-1} were observed during the first 2300 h of operation at 800 °C. At 700 °C, a voltage and ASR degradation of 1.9% kh^{-1} and 9.0% kh^{-1} were detected. The authors also conducted a long-term electrolysis test of an SOEC stack using the cell configuration mentioned above and the same conditions for around 20 000 h. At 800 °C, they achieved an average voltage degradation rate of 0.6% kh^{-1} after 18 000 h of electrolysis operation.[419] The same cell configuration was galvanostatically tested for 9300 h at a set current density of −1.0 A cm^{-2}, which resulted in an overall voltage degradation rate of 3.8% kh^{-1}.[135] The long-term stability test of a Ni-YSZ/YSZ/GDC/LSCF-GDC cell configuration at 750 °C with a current density of −0.3 A cm^{-2} in a 20% H_2 + 40% H_2O + 40% CO_2 atmosphere was conducted for 1000 h.[357] A voltage increase led to a degradation rate of 10.69% kh^{-1}. The stability of a Ni-YSZ/YSZ/LSM-YSZ cell configuration at current densities of −2.0 A cm^{-2} and −1.5 A cm^{-2} in 45% H_2O + 45% CO_2 + 10% H_2 for 700 h exhibited voltage degradation rates of 0.452 V kh^{-1} and 0.275 V kh^{-1} respectively for the period between 400 h and 700 h.[359] Post-test analysis showed severe changes in the microstructure of the fuel electrodes, such as the loss of Ni percolation, contact loss between YSZ and Ni, and the decomposition of YSZ. Additionally, the formation of nano-zirconia inside the Ni-YSZ electrode was detected.[359]

The chemical stability of a Ni-YSZ fuel electrode in CO_2 electrolysis tested in pure CO_2 at 700 °C and a set voltage of 1.5 V for 60 h achieved a relatively stable current density of −0.330 A cm^{-2} throughout the testing period.[429] XRD measurements of the fuel electrode subsequently showed only slight changes in the patterns and no NiO peak. In addition to the XRD, the authors analyzed the post-test microstructure using SEM images. They observed the agglomeration of Ni particles inside the fuel electrode but no carbon deposition on the surface or cross-section of the fuel electrode.[429] The stability of a Ni-GDC fuel electrode operated for 80 000 current on/off cycles was investigated under steam electrolysis for one year at a temperature of 856–860 °C.[430] The authors used the following ESC with a configuration of Ni-GDC/GDC/YSZ/GDC/LSCF. The set current densities were −0.7 A cm^{-2} (ON) and −0.07 A cm^{-2} (OFF) in an atmosphere of 75% humidified H_2. The resulting voltage degradation rate over the whole period of operation was 0.4% kh^{-1}, with an ASR degradation of 7.3 mΩ cm^2 kh^{-1}.

Ni-GDC fuel electrodes were tested with the same cell composition in co-electrolysis and steam electrolysis operation at 900 °C with a current of −0.5 A cm^{-2} for 500 h.[362] In co-electrolysis conditions, the resulting degradation rate of 308 mV kh^{-1} was lower than the degradation observed for steam electrolysis (499 mV kh^{-1}). The polarization resistance over time also increased from 0.07 Ω cm^2 to 0.28 Ω cm^2 in steam electrolysis, and from 0.10 Ω cm^2 to 0.16 Ω m^2 in co-electrolysis

operation. In the microstructural post-test analysis, the authors compared the average Ni particle size of the as-reduced cell with the operated cell and observed an increase in the Ni particle size. The as-reduced cell featured a Ni particle size of 1.37 μm, whereas the Ni particle sizes increased to 2.19 μm (62%) and 2.86 μm (109%) during steam and co-electrolysis. Besides the Ni agglomeration/particle growth, Ni depletion, and a loss of GDC percolation with GDC-covered Ni particles were found.[362] A long-term stability test of a 3Mo-3Au-Ni-GDC/YSZ/GDC/LSCF cell configuration was conducted for 1700 h at a temperature of 900 °C and in a 7% H_2 + 30% N_2 + 63% H_2O atmosphere with a set current density of −0.3 A cm^{-2}.[363] During the 1700 h of operation, an increase in cell voltage from 0.99 V to 1.05 V was observed with an overall degradation rate of 33 mV kh^{-1}. Post-test analysis showed no delamination or cracks occurring, but Ni particle coarsening and Ni depletion at the fuel electrode/electrolyte interface were detected. In this study, a comparison between an as-reduced cell and an operated cell led to the conclusion that the operation in electrolysis mode increases the tendency to coalesce and build clusters. Furthermore, a loss of GDC percolation and the coverage of Ni particles by GDC was discovered as well as an increase in pore size and pore fraction.[345]

3.3.5.1. Perovskite-based fuel electrode materials. Perovskites have a high potential for application as fuel electrode materials in high-temperature electrolysis cells. A prerequisite for successful application in SOECs is the long-term stability of the electrode under the applied operating conditions.

The chemical stability of LSCM-based fuel electrodes for SOECs has been tested in different reducing atmospheres.[364,366,367] After exposing pure LSCM powder to 40 sccm H_2 (ref. 366) and 30 sccm H_2 (ref. 367) with an absolute humidity (AH) of 80 vol% at 900 °C for 24 h, the subsequent XRD analysis did not show secondary phases or peak splitting. The authors conclude that LSCM is chemically stable in a reducing atmosphere combined with a high AH.[366,367]

The chemical stability of an LSCM-GDC composite (ratio 1 : 1) electrode in a humid CO_2 atmosphere (50% H_2O + 50% CO_2) at 850 °C for 20 h has been confirmed.[364] The LSCM-YSZ composite electrode material was tested in terms of its chemical stability during heat treatment at 1400 °C in air for 4 h and under a reducing atmosphere (30 sccm H_2, 80 vol% AH, 900 °C, 24 h).[367] No secondary phases or peak splitting were detected for both samples, which is in agreement with the results for pure LSCM. Furthermore, changes to the electrode microstructure of a fuel electrode-supported cell, which occurred during electrolysis operation for 103 h at 850 °C with a current density of −0.33 A cm^{-2} in 45 vol% AH and a 30 sccm H_2 atmosphere were analyzed. Coarsening of the interface and a minor crack between the LSCM-YSZ electrode and the YSZ electrolyte were observed. The authors attributed this to the increasing loss of lattice oxygen in the LSCM crystal throughout the operation, leading to an alteration in the thermal expansion behavior of the LSCM electrode and, therefore, mechanical stresses at the electrode/electrolyte interface.[367] Initial short-term durability tests for LSCM fuel electrodes in steam electrolysis operations have been already conducted. Cells tested at 850 °C for 35 h under galvanostatic operation using a current density of −0.2 A cm^{-2}, a gas mixture of 60 vol% AH, and 40 sccm H_2 as a carrier gas exhibited a relatively stable voltage of 1.22 V throughout the test.[366]

At a higher current density of −0.6 A cm^{-2} and a lower temperature of 800 °C in the gas mixture of 13% H_2O + 6.5% H_2 + 80.5% N_2, the cell reached a voltage of 1.7–1.75 V during 25 h with a degradation rate of 0.022% h^{-1}.[431] In co-electrolysis mode, short-term stability tests with LSCM fuel electrodes showed a decrease of the current density from −0.1031 A cm^{-2} to −0.09761 A cm^{-2} during a test period of 24 h at 800 °C under a set voltage of 1.5 V in 60% H_2O + 40% CO_2.[365] An LSCM-GDC composite electrode with a set current density of −0.3 A cm^{-2} at 800 °C using 50% H_2O + 50% CO_2 exhibited an initial voltage increase during the first 8 h, and a stable voltage of 1.5 V was achieved during the following 100 h of operation.[364]

The chemical compatibility of LSFM ($La_{0.6}Sr_{0.4}Fe_{0.8}Mn_{0.2}O_{3-\delta}$) and YSZ has been investigated for a heat-treated mixture of LSFM and YSZ (50 : 50 wt%) for one week in a temperature range of 600–950 °C.[375] No chemical reaction was detected for temperatures of 600–850 °C, whereas secondary phase formation in the form of $SrZrO_3$ was identified for temperatures of 900–950 °C. The authors concluded that LSFM and YSZ show good compatibility in an intermediate temperature range. The compatibility between LSFM and GDC was also investigated at 800 °C in air and CO_2 with respective heat treatment, and no impurity phases were observed in both tested atmospheres.[376]

The stability of an LSFM ($La_{0.6}Sr_{0.4}Fe_{0.9}Mn_{0.1}O_{3-\delta}$) electrode was investigated in CO_2 electrolysis with 50% CO_2 + 1% CO + 49% Ar.[378] Post-test analysis of the fuel electrode microstructure with SEM and XRD was performed. No significant changes in the electrode microstructure and only small peaks of secondary phases in the XRD pattern were found. The short-term stability of an LSFM-GDC fuel electrode during CO_2 electrolysis was tested at 800 °C under a constant current of −0.4 A cm^{-2}. The authors observed a voltage increase from 1.30 V to 1.37 V after 40 h of operation. However, the post-test analysis showed no impurities in the electrode material and no significant structural changes in the microstructure of the electrode.[376] The short-term stability of a fuel electrode consisting of LSFM ($La_{0.6}Sr_{0.4}Fe_{0.8}Mn_{0.2}O_{3-\delta}$)-CuF (1 : 1) was analyzed using an LSGM electrolyte and a BLC ($Ba_{0.6}La_{0.4}CoO_{3-\delta}$) oxygen electrode. After 100 h at a constant current density of −0.765 A cm^{-2} in an atmosphere with 50% CO_2 + 10% H_2O + 40% Ar at 800 °C, the cell exhibited a voltage of approx. 1.3 V with a corresponding degradation rate of 0.038% h^{-1}.[371]

The chemical stability in reducing atmospheres and structural changes of pure and doped LST ($La_{0.2}Sr_{0.8}TiO_{3+d}$) electrode material has been characterized by several studies.[379,384,385,387]

Partly chemical reduction of the Ti^{4+} ions to Ti^{3+} due to heat treatment at 800 °C for three hours in 5% H_2 + 95% Ar followed by an increase in the lattice parameters was observed.[379] No phase changes through reduction were detected. Additionally, the authors examined the stability of iron-doped LST in reducing atmospheres. Here, a partial change from Ti^{4+} to Ti^{3+} is also observed as well as a reduction from iron oxide to metallic Fe. Redox cycling experiments (800 °C, 5% H_2 + 95% Ar/

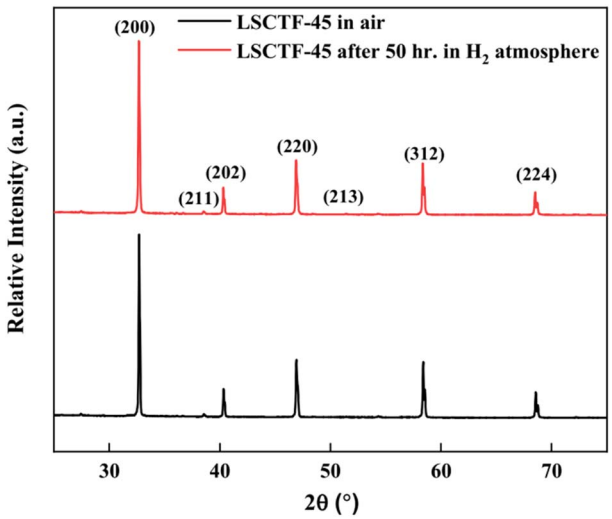

Fig. 23 LSCTF-45 diffraction patterns: black: as-prepared LSCTF-45 powder, red: reduced LSCTF-45 powder (1000 °C, 50 h, 100% H_2).[385] Reprinted from, ©The Electrochemical Society. Reproduced by permission of IOP Publishing Ltd. All rights reserved.

pure air, for 10 h) regarding the conductivity of the respective material confirmed the chemical stability of LST and iron-doped LST in operation in alternating oxidizing and reducing atmospheres.[379] The stability of LST ($La_{0.2}Sr_{0.8}TiO_{3-\delta}$) in wet H_2 at 1400 °C for 10 h was investigated and XRD results confirmed the preservation of the crystal structure of LSTO during the reduction.[384] The authors detected a minimal decrease in the cell parameters after the reduction process. This was attributed to the fact that only a small amount of Ti^{4+} was reduced to Ti^{3+} and, therefore, the loss of oxygen likely prevents an increase of the average radii of Ti.[384] After heat treatment of LSTO and Mn-doped LSTO ($La_{0.2}Sr_{0.8}Ti_{0.9}Mn_{0.1}O_{3+\delta}$) at 1300 °C for 10 h in 5% H_2 + 95% Ar to analyze chemical stability, the unit cell parameters increased due to the reduction of Ti^{4+} and, in the case of the Mn-doped LSTO, a partial Ti^{4+} reduction as well as a reduction of Mn^{4+} to Mn^{3+}.[387] Post-test characterization confirmed no phase transition had occurred.[387] A Ca- and Fe-doped LSTO ($La_{0.2}Sr_{0.35}Ca_{0.45}Ti_{0.95}Fe_{0.05}O_{3-\delta}$ (LSCTF-45)) is chemically stable under a 100% H_2 atmosphere for 50 h at 1000 °C.[385] The XRD patterns in Fig. 23 show no apparent differences between the as-prepared LSCTF-45 and the reduced LSCTF-45 powder. Furthermore, the authors observed lattice parameter decrease of LSCTF with a higher Ca ratio.[385]

Several studies were conducted to investigate the stability of the LST-based fuel electrode during electrolysis operation. A composite electrode of LST ($La_{0.2}Sr_{0.8}TiO_{3+\delta}$)-$Ce_{0.8}Sm_{0.2}O_{2-\delta}$ (SDC) (ratio 65 : 35 wt%) has been investigated in very short experiments of 21 min each in SOEC CO_2 electrolysis with a YSZ electrolyte and an LSM-SDC oxygen electrode.[387] The cells were characterized at three different voltages (1.2 V, 1.6 V, and 2.0 V) at 800 °C in pure CO_2 atmosphere and exhibited a decrease in current density above 1.2 V. The short-term stability of a composite LST-SDC fuel electrode, using a ratio of 50 : 50 wt%, was investigated for 0.5 h at 700 °C using a constant voltage of 2 V with cells composed of LST-SDC/YSZ/LSM-SDC.[384] The authors tested the stability of the fuel electrode material under CO_2 electrolysis operation and achieved a constant current density of −0.125 A cm^{-2}.[384] In steam and CO_2 electrolysis, a composite LST ($La_{0.2}Sr_{0.8}TiO_{3+\delta}$)-GDC (50 : 50 wt%) fuel electrode was tested at 700 °C with a voltage of 2 V in different atmospheres (3% H_2O + 97% N_2 and CO_2 = 100%) on a YSZ electrolyte-supported cells with an LSM-GDC oxygen electrode. During steam electrolysis of around 20 h, they achieved a relatively stable current density of −0.090 A cm^{-2} as well as a current density of −0.080 A cm^{-2} for 0.7 h CO_2 electrolysis.[383]

Pure SFM ($Sr_2Fe_{1.5}Mo_{0.5}O_{6-\delta}$) and Sb-doped SFM ($Sr_2Fe_{1.5}Mo_{0.5}Sb_{0.1}O_{6-\delta}$) electrode material were examined at 800 °C in a humidified H_2 atmosphere for 5 h.[389] The results are shown in Fig. 24 and indicate that both SFM and Sb-SFM preserved the cubic crystal structure under these conditions. Despite a slight shift of some diffraction peaks (Fig. 24b) to lower angles, there are no significant XRD pattern changes. The peak shift is attributed to an increased cell volume correlating with a decrease in Fe and Mo valences. A subsequent microstructure analysis of the Sb-SFM using TEM-EDS (Fig. 24c) confirmed the stability of this electrode material in humidified reducing atmospheres. Similar results were obtained by studying the structural stability of Mn-doped SFM ($Sr_2Fe_{1.4}Mn_{0.1}Mo_{0.5}O_{6-\delta}$) at 850 °C for 12 h in a 5% H_2 + 95% Ar atmosphere.[390] To obtain information about the stability of an SFM fuel electrode in a symmetrical cell with LSGM electrolyte in steam electrolysis, short-term experiments at 850 °C with a set voltage of 1.2 V for 100 h in a 60 vol% AH atmosphere were conducted.[179] Throughout the 100 h test, the current density was between −0.5 A cm and −0.7 A cm^{-2}, and only a slight decrease in the current density was detected during the first 10 h. Furthermore, the short-term co-electrolysis stability of a symmetrical cell, consisting of SFM electrodes and a ytterbium scandium stabilized zirconia (YbScSZ) electrolyte, was investigated at 900 °C and a constant current density of −0.5 A cm^{-2}.[182] The fuel gas composition consisted of 75% H_2O + 25% CO_2. After 24 h of, the gas composition of the symmetrical cell was reversed at the two electrodes and the electrolysis was operated for a further 18 h. A slight increase of 1 mV h^{-1} in voltage over the first 24 h was observed, indicating degradation processes inside the material.[182] The stability of an SFM-SDC composite electrode (60 : 40 wt%) was characterized in co-electrolysis mode and a symmetrical, LSGM electrolyte-supported cell.[180] The authors conducted galvanostatic experiments at a current density of −0.12 A cm^{-2} and a temperature of 800 °C in a 16% H_2O + 16% CO_2 + 20% H_2 + 48% N_2 atmosphere. They observed a degradation rate of 0.00013 V h^{-1} over 103 h of testing. The microstructural analysis of the SFM-SDC electrode before and after electrolysis operation using SEM and EDX analysis subsequently showed no obvious grain growth, new phase formations, or carbon deposition.[180] The stability of an Mn-doped SFM-SDC composite electrode in CO_2 electrolysis was examined using cells consisting of SFMMn-SDC/LSGM/LSCF-SDC. At 750 °C and a constant voltage of 1.3 V, the authors achieved a stable current density of −0.6 A cm^{-2} for 50 h.[390] Post-test analysis with SEM and Raman spectroscopy confirmed good adherence between the electrode and the electrolyte, the

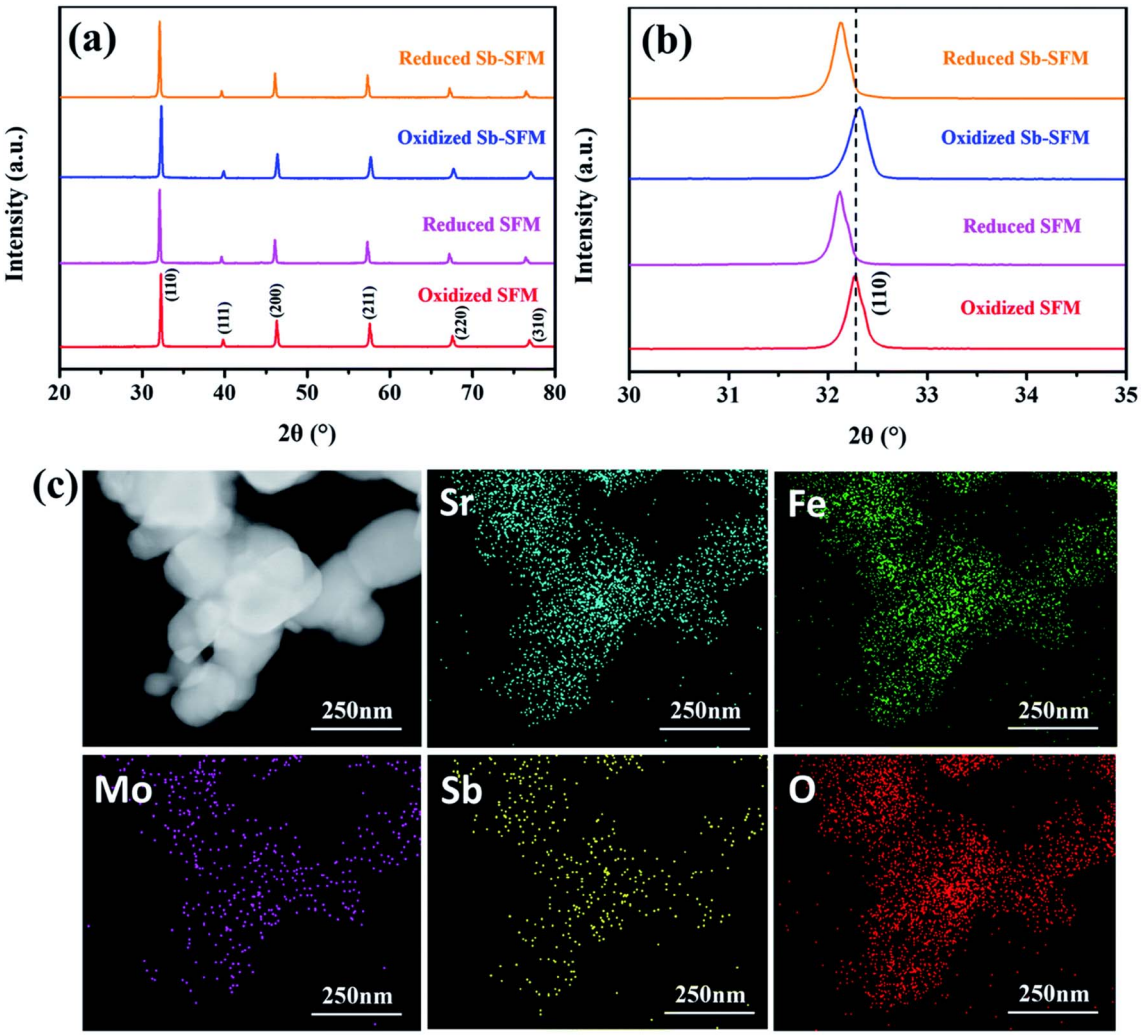

Fig. 24 Chemical stability analysis for SFM-based material: (a) and (b): XRD analysis of pure SFM and Sb-SFM in an oxidized and reduced state, (c): TEM-EDS of Sb-SFM after reduction; reduction parameters: humidified H_2, 5 h, 800 °C. Reprinted with permission from ref. 389 with permission from the Royal Society of Chemistry.

stability of the fuel electrode under the tested conditions, and the fact that there was no carbon deposition on the Mn-doped SFM fuel electrode during pure CO_2 electrolysis.[390]

The chemical stability of Mn-doped SFN double perovskites after heat treatment in a reducing atmosphere (80% H_2O + 20% H_2/air, 900 °C, 24 h) was analyzed by XRD measurements.[401] The oxidized and reduced Mn-SFN powders showed no apparent differences in the XRD patterns for a low doping content of $0 \leq x \leq 0.2$. Nevertheless, a shift from high-angle peaks to smaller angles was observed with increasing Mn content. According to the authors, this shift correlates to an expansion of the crystal lattice.[401] The reactivity of Co-doped SFN ($Sr_2Fe_{0.1}Co_{0.9}NbO_6$) with YSZ and GDC using powder mixtures with a weight ratio of 1 : 1 was tested by sintering at 1200 °C for 24 h.[398] The authors were not able to detect any new, additional peaks or peak shifting in the resulting XRD patterns.[398] For the simple perovskite $SrFe_{0.9}Nb_{0.1}O_{3-\delta}$, its chemical stability in reducing atmospheres was confirmed after reducing the powder in 5H_2 + 95% Ar at 700 °C for 10 h.[399] After the reduction of $SrFe_{0.9}Nb_{0.1}O_{3-\delta}$ doped with Cu ($x = 0.1$), the perovskite main phase in addition to a peak of metallic iron was detected in the XRD pattern. With increasing Cu content, Cu-rich and Fe-rich alloys were formed. Cycling tests to establish the reversibility of this exsolution process showed that the exsolved metal ions dissolved back into the crystal lattice during re-oxidation and exsolved again during reduction.[399]

The stability of $(PrBa)_{0.95}(Fe_{0.9}Mo_{0.1})_2O_{5+\delta}$ under reducing conditions after heat treatment for 200 h at 1000 °C was investigated *via* XRD.[407] Besides a slight shift in the diffraction peaks, the authors were unable to detect secondary phase formation in the XRD pattern. The chemical compatibility between the PBFM and LSGM at 1000 °C for 100 h was also studied and no chemical reactions were observed.[407] The short-term stability of a PBFM-SDC fuel electrode (70 : 30 wt%) was tested under steam electrolysis conditions with a cell composed of PBFM-SDC/LSGM/SDC-PBFM. The cells achieved a current density of −0.51 A cm^{-2} at 1.3 V and 800 °C in a 3% H_2O + 97% H_2 atmosphere for 6 h.[404]

3.3.5.2. Summary of fuel electrode materials. The state-of-the-art fuel electrode materials for SOECs are the cermets electrodes composed of Ni-YSZ and Ni-GDC. These materials exhibit sufficient performance and stability in electrolysis operation and are currently used in commercially available SOECs. Nevertheless, especially in the case of fuel electrode-supported SOECs, severe degradation of these fuel electrode materials during electrolysis operation occurs. The main degradation processes inside the Ni cermet fuel electrode are Ni particle agglomeration/coarsening and Ni migration. These mechanisms change the microstructure of electrode and lead to a reduction of active sites and a thicker electrolyte layer during electrolysis operation. Subsequently, this leads to a severe performance loss with increasing duration and operating time.

To overcome the challenges regarding cell longevity and costs, new fuel electrode materials and/or microstructures must be developed. Currently, many materials, including $La_{0.75}Sr_{0.25}Cr_{0.5}Mn_{0.5}O_{3-\delta}$ (LSCM), $La_{0.6}Sr_{0.4}Fe_{0.8}Mn_{0.2}O_{3-\delta}$ (LSFM), $La_{0.2}Sr_{0.8}TiO_{3+\delta}$ (LST) or double perovskites as $Sr_2Fe_{1.5}Mo_{0.5}O_{6-\delta}$ (SFM) or $Sr_2FeNbO_{6-\delta}$ (SFN) are investigated as alternative fuel electrode materials. These alternative electrodes still have certain limitations regarding their catalytic activity and/or ionic and electronic conductivity or stability under operating conditions. These limitations lead to insufficient performance and durability of the cells. Therefore, studies are carried out to improve the properties and enhance the material's stability using composite materials, infiltration of active catalysts in perovskite-based electrode scaffolds, and/or exsolution processes on the electrode's surface. However, none of these alternative materials reached the technological maturity for commercialization, and no long-term (>5000 h) durability tests have been carried out yet.

3.4. Further stack components

Other stack components such as interconnects, sealants, contact layers, and Cr retention layers are also crucial to the development of high-performance and durable SOECs. However, in current SOEC research, the components used and their related materials have been adapted from extensively studied and optimized SOFC research. They have already been proven to fulfill all the requirements of SOEC stacks for high and stable performance during medium-term operation.[31,35,73,80,432,433] The longest example of operation amounts to ~20 000 h.[37] In this section, a brief overview of these additional components and the materials used will be presented.

3.4.1. Interconnects. Solid oxide cells are operated in cell repeat units referred to as stacks, as shown in Fig. 3, in which interconnects act as an electrical connector between the fuel and the oxygen electrode of adjacent cells, thus separating the oxidizing and reducing atmospheres on both sides. This necessitates gas tightness and excellent electrical conductivity (area-specific resistance (ASR) less than 0.1 Ω cm^2) in addition to good chemical stability (phase and microstructure stability in both oxidizing and reducing atmospheres) at operating conditions for the targeted stack lifetime.[434,435] The relative thermal expansion, given by the thermal expansion coefficient (TEC), is matched to the electrodes and the electrolyte material (~10–13 $\times$ 10^{-6} K^{-1}) to minimize thermal stresses when heating up and cooling down the stack. Criteria for the material selection of interconnects include mechanical stability (creep resistance, strength), ease of fabrication, and material costs.[435]

3.4.1.1. Ceramic interconnects. The most common ceramic interconnect material is perovskite-based lanthanum chromite $LaCrO_3$. It is a p-type semiconductor material, which was previously used due to its sufficient electrical conductivity (~1 S cm^{-1} at 1000 °C),[434] good material stability, and its average thermal expansion coefficient of 9.5 $\times$ 10^{-6} K^{-1} near YSZ (10.5 $\times$ 10^{-6} K^{-1}). However, it is difficult to obtain dense $LaCrO_3$ layers during fabrication and processing, which limits the attainable geometries. Additionally, lanthanum is considered an expensive rare-earth material for large-scale production. The most prominent use of doped $LaCrO_3$ as an interconnect is the old tubular-type Westinghouse/Siemens SOFC.[436] In recent years, the use of $LaCrO_3$ as a ceramic interconnect material has declined with typical operating temperatures decreasing from ~1000 °C to 600–900 °C, with the focus of research thus shifting to metallic interconnect materials.

3.4.1.2. Metallic interconnects. Due to their superior characteristics, metallic alloys have replaced $LaCrO_3$ as the preferred interconnect material. Their mechanical strength supports all ceramic components in the stack and the easy, low-cost processing enables the construction of gas channels with innovative flow configurations (*e.g.*, counter-flow, cross-flow, and/or co-flow). The interconnects are commonly comprised of high electronic and thermal conductive metal alloys containing Cr and/or Cr and Fe, which grow electrically conducting oxide layers (Cr_2O_3) during operation. However, excessive pure Cr-oxide layer growth is certain for higher chromium contents (compared to *e.g.*, Cr-containing spinel layers) and results in electrode poisoning and an undesirable high ASR. A Cr content of 20–25% is necessary for a continuous oxide layer in operation.[437] Fe–Cr alloys such as Crofer22APU, Crofer22H, SUS 430, and similar metals are more ductile than nearly pure Cr-based alloys like $Cr5FeY_2O_3$, but both types show great promise as interconnect materials in stacks due to their optimized thermal expansion coefficient (Fe–Cr alloys for FESCs and Cr alloys for ESCs) and easy processing methods.[438] While the Cr alloys form pure Cr_2O_3 scales under both oxidizing and reducing conditions, Fe–Cr alloys – developed especially for SOFC use – form an oxide double layer (*e.g.*, Crofer types). This double layer consists of an inner pure chromia scale and an outer Cr–Mn spinel layer. Mn thus has to be added as an alloying element for the build-up of this double layer. The formation of an outer spinel layer reduces the evaporation of volatile Cr species from the oxide scale, thus reducing the number of available molecules which can interact with the oxygen electrode materials and, in turn, leading to reduced Cr-induced degradation. However, even these double layers evaporate too much Cr for long-term SOC operation and additional Cr retention layers therefore have to be added (see Section 3.4.2).[439–442]

3.4.2. Contact and Cr retention layers. In addition to special interconnect materials (see Chapter 3.4.1), possible mitigation solutions for Cr poisoning of the oxygen electrodes

Table 5 Linear thermal expansion coefficients between 30 °C and 800 °C and between 30 °C and 1000 °C for solid oxide electrolyzer components

Material	Component	TEC/10^{-6} K^{-1} 30–800 °C	30–1000 °C	Ref.
$BaO–Al_2O_3–Nd_2O_3–SiO_2$	Glass sealing	13.3	13.6	193
$Al_2O_3–MgO–CaO–BaO–SiO_2–B_2O_3$	Glass sealing	12.3	13.3	193
$Al_2O_3–MgO–SiO_2–B_2O_3$	Glass sealing	11.4	12.0	193
X 10 CrAl 18	Interconnect	12.9	13.9	193
$La_{0.9}Sr_{0.1}CrO_3$	Interconnect	—	10.7	69
Cr Fe_5 Y_20_31	Interconnect	11.3	12.0	193
$La_{0.7}Ca_{0.3}Cr_{0.5}Ti_{0.5}0_3$	Interconnect	9.6	10.1	193
Ni-8YSZ (40% Ni-60%YSZ)	Cermet electrode	12.5	12.6	193
$Zr_{0.85}Y_{0.15}O_{1.93}$ (8YSZ)	Electrolyte	10.5	10.8	193
$Zr_{0.82}Y_{0.18}O_{1.91}$ (10YSZ)	Electrolyte	10.6	11.0	193
$Zr_{0.85}Sc_{0.15}O_{1.93}$ (8ScSZ)	Electrolyte	10.3	10.4	462
$Zr_{0.80}Sc_{0.19}Al_{0.02}O_{1.90}$ (10ScSZ)	Electrolyte	10.5	10.9	193
$Ce_{0.8}Gd_{0.2}O_{1.90}$ (GDC)	Electrolyte	12.5	12.7	193
$La_{0.9}Sr_{0.1}Ga_{0.8}Mg_{0.2}O_3$ (LSGM)	Electrolyte	10.9	11.4	193
$La_{0.79}Sr_{0.2}MnO_3$ (LSM)	Perovskite	10.8	11.1	463
$La_{10}Si_6O_{27}$	Electrolyte	9.0 (800 °C)	—	464
$La_{9.5}$ $(Ge_{5.5}Al_{0.5}O_{24})O_2$	Electrolyte	8.9 (500–900 °C)	—	106
$LaMn_{0.45}Co_{0.35}Cu_{0.2}O_3$ (LCC10)	Interconnect	~14	—	465 and 466
$La_{0.8}Sr_{0.2}CoO_3$ (LSC)	Electrode	—	19	373
$La_{0.58}Sr_{0.4}Co_{0.2}Fe_{0.8}O_3$ (LSCF)	Contact layer, electrode	—	13–16	146 and 373
$La_{0.8}Sr_{0.2}Co_{0.5}Mn_{0.5}O_3$ (LSMC)	Contact layer	—	12–16	373 and 467
$Mn_{1.0}Co_{1.9}Fe_{0.1}O_4$ (MCF)	Protective coating	~13	—	468 and 469
Crofer22 APU	Interconnect	11.9	—	455
$La_{0.98}Ni_{0.6}Fe_{0.4}O_3$ (LNF)	Contact layer	13.5	—	460
$La_{0.65}Sr_{0.3}MnO_3$ (LSM)	Contact layer	12.8	—	460

are protective coatings like $Mn_{1.0}Co_{1.9}Fe_{0.1}O_4$ (MCF), which are applied, for example, by atmospheric plasma spraying (APS) and can negate this effect.[443–446] Comparable results can also be achieved with other spinel coatings (Mn–Co, Mn–Cu, Ce–Co) or perovskites[447–449] and alternative coating technologies such as wet chemical coating methods (*e.g.*, wet powder spraying), screen printing, slurry dip coating, and electroplating as well as high vacuum deposition techniques such as physical vapor

Table 6 Summary of electrochemical performance for state-of-the-art materials compared to double perovskite materials such as oxygen electrode materials in solid oxide electrolysis cells

Structure	Test conditions	i@ 1.3 V/A cm^{-2}	R_P@OCV/Ω cm^2	Ref.
SFM/LSGM/SFM	40% H_2O + 60% H_2, 800 °C	−0.48	0.68	179
	40% H_2O + 60% H_2, 900 °C	−0.59	0.23	179
Ni-YSZ/YSZ/YSZ-LSM	50% H_2O + 50% H_2, 800 °C	−0.3	1.0	470
	50% H_2O + 50% H_2, 900 °C	−0.7	0.44	470
Ni-YSZ/YSZ/YSZ-LSM	60% H_2O + 40% H_2, 800 °C	−0.24	—	471
	60% H_2O + 40% H_2, 900 °C	−0.38	0.71	471
SFM-SDC/LSGM/SFM-SDC[180]	16% H_2O + 16% CO_2 + 20% H_2 + 48% N_2, 850 °C	−0.734	0.48	180
Ni-YSZ/YSZ/LSM-YSZ	45% H_2O + 10% H_2 + 45% CO_2, 850 °C	−1.000	0.42	472
SFM/YbScSZ/SFM	90% H_2O + 10% Ar, 900 °C	−1.4		182
	75% H_2O + 25% CO_2, 900 °C	−1.1		182
SFM-LSGM/LSGM/SFM-LSGM	100% CO_2, 800 °C	−0.92	0.226	473
SFM/LSGM/SFM	60% H_2O + 40% H_2, 900 °C	−0.88	0.26	179
Ni-SDC/SDC/$PrBaCo_2O_{5+\delta}$	100% H_2, 650 °C		0.05	195
Ni-GDC/LCO/LSGM/PBC-10 wt% GDC	H_2 + 3% H_2O, 850 °C		0.168	194
	H_2 + 3% H_2O, 550 °C		0.550	194
Ni-GDC/LCO/LSGM/PBC	H_2 + 3% H_2O, 850 °C		0.136	194
	H_2 + 3% H_2O, 550 °C		0.698	194
$La_{0.4}Ce_{0.6}O_2$ (LCO)				
$La_{0.8}Sr_{0.2}Ga_{0.87}Mg_{0.13}O_3$ (LSGM)				
$(ZrO_2)_{0.9}(Yb_2O_3)_{0.06}(Sc_2O_3)_{0.04}$ (6Yb4ScSZ)				
$Sm_{0.2}Ce_{0.8}O_{1.9}$ (SDC)				
$PrBaCo_2O_{5+\delta}$-$Gd_{0.1}Ce_{0.9}O_{2-\delta}$ (PBC-GDC)				

deposition (PVD) and atomic layer deposition (ALD). A dense protective layer has been shown to have a high capability of blocking Cr diffusion and thus prolonging stack durability.[40,450,451] Protective layers prepared with deposition techniques (*e.g.*, PVD, ALD) are thin and dense enough to prevent Cr evaporation and reduce contact resistance. In comparison, wet coating methods produce a more porous coating microstructure, which requires additional densification at high temperatures. Layer densification and crack healing by annealing APS-MCF in air were demonstrated to simulate operation conditions.[444,452,453] The MCF coating was deposited in reducing conditions, which led to a metastable rock-salt configuration. After annealing in air, the low-temperature stable spinel phase (T < 1050 °C) was formed due to the incorporation of oxygen, leading to densification of the coating and sealed cracks. The application of dense coatings (irrespective of the applied technology) which hinder Cr diffusion is essential for long-term SOC operation. Applying these types of layers has been proven to function up to approx. 35 000 h.[320,454]

Contact layers reduce the interfacial contact resistance between the electrode and the interconnect, act as a gas distribution element (on the fuel side), ensure proper contacting by minimizing/leveling layer surface roughnesses and manufacturing-related differences (*e.g.*, height, layer thickness), and might also act as Cr getter layers.[455] On the airside, they are typically applied on the cells or the interconnect and sintered *in situ* during stack assembly and sealing at appropriate temperatures. On the fuel electrode side, the combination of either a Ni contact paste or current collection layer (*e.g.*, for ESCs) or the Ni-containing support (FESCs) and a Ni mesh/felt/foam forms a kind of metallurgical bond with the interconnect, which lowers the electrical resistance and is therefore currently used exclusively by industry and research for state-of-the-art Ni cermet electrodes.[456–459] The contact layer for the oxygen electrode has to be chemically compatible with the Sr-doped electrode material and Cr-forming interconnects, and must therefore be oxidation-resistant. Additional challenges include the high resistance of the metal/ceramic interface and the thermal gradients across the cell, which can lead to contact layer delamination. The materials are selected according to their thermal expansion behavior, their reactivity, and conductivity at operating temperatures. Commonly used contact layer materials listed in Table 5 include $La_{0.7}Sr_{0.3}CoO_3$/$La_{0.6}Sr_{0.4}Co_{0.8}Fe_{0.2}O_3$ LSC(F), $La_{0.98}Ni_{0.6}Fe_{0.4}O_3$ (LNF), $La_{0.65}Sr_{0.3}MnO_3$ (LSM), and $La_{0.7}Sr_{0.3}FeO_3$ (LSF).[460] In many cases, the difference between the real air-side electrode and the contact layer, which might be made of the same material, is their microstructure and overall thickness. While the oxygen electrode is developed for high electrochemical performance and thus has a fine structure for the most part (high amount of triple phase boundaries and/or high available surface area) and has a thickness adapted to the resistances within the overall cell, the

Table 7 Oxygen over-stoichiometry δ calculated from TGA and iodometry measurements, average δ value, and different thermal expansion coefficients (TECs)

Nickelates	δ_{TGA}	δ_{iodo}	$\delta_{mean\ value}$	Thermal expansion coefficient/K^{-1} from Dilatometry 10^{-6}	XRD 10^{-6}	Ref.
$La_2NiO_{4+\delta}$	0.16	0.16	0.16	13.0	12.8	201, 216 and 240
	0.14, 0.11					201
$La_2Ni_{0.75}Cu_{0.25}O_{4+\delta}$	0.16, 0.13	0.13	0.14	—	—	201
$La_2Ni_{0.50}Cu_{0.50}O_{4+\delta}$	0.11, 0.09	0.09	0.10	12.8		201
$La_2Ni_{0.25}Cu_{0.75}O_{4+\delta}$	0.05	0.05	0.05			201
$La_2CuO_{4+\delta}$	—	0.01	0.01	0–250 °C: 8.6 250–900 °C: 13.8	12.8	201
$La_2Ni_{0.9}Co_{0.1}O_{4+\delta}$	0.18	—	0.18			474
$La_2Ni_{0.8}Co_{0.2}O_{4+\delta}$	0.20	—	0.20			474
$Pr_2Ni_{0.9}Co_{0.1}O_{4+\delta}$	0.27	—	0.27			474
$La_{1.5}Pr_{0.5}Ni_{0.9}Co_{0.1}O_{4+\delta}$	0.23	—	0.23			474
$La_{1.5}Pr_{0.5}Ni_{0.8}Co_{0.2}O_{4+\delta}$	0.25	—	0.25			401 and 474
$La_{1.5}Pr_{0.5}NiO_{4+\delta}$	0.16	0.17	0.17			240
$LaPrNiO_{4+\delta}$	0.19	0.19	0.19			240
$La_{0.5}Pr_{1.5}NiO_{4+\delta}$	0.22	0.20	0.21			240
	0.21	0.20	0.205			475
$Pr_2NiO_{4+\delta}$	0.25	0.25	0.25			240
	0.23, 0.19	0.21	0.21			216
	0.25	0.23	0.24			217
$Pr_4Ni_3O_{10+\delta}$	0.10	—	—	12.0	10.0	314
$Pr_2Ni_{0.9}Co_{0.1}O_{4+\delta}$	0.27	0.27	0.27			217
$Pr_2Ni_{0.8}Co_{0.2}O_{4+\delta}$	0.30	0.28	0.29			217
$Nd_2NiO_{4+\delta}$	0.23, 0.21	0.21	0.22	12.7	11.9	216
$Nd_{1.9}Ca_{0.1}NiO_{4+\delta}$	—	0.20	0.20			216
$Nd_{1.8}Ca_{0.2}NiO_{4+\delta}$	—	0.10	0.10			216
$Nd_2Ni_{0.9}Co_{0.1}O_{4+\delta}$	0.26	—	0.26			474
$Nd_2Ni_{0.8}Co_{0.2}O_{4+\delta}$	0.29	—	0.29			474

Table 8 Summary of electrochemical performance of nickelate materials as oxygen electrode materials in solid oxide electrolysis cells

Nickelates	σ_e in air/S cm^{-1}	Conditions	R_P OCV/Ω cm^2	i@ 1.5 V/A cm^{-2}	Ref.
Ni-YSZ/YSZ/GDC/$Pr_2Ni_{0.8}Co_{0.2}O_{4+\delta}$	60 (700 °C)	50% H_2 + 50% H_2O, 800 °C	0.118	−1.90	474 and 476
		50% H_2 + 50% H_2O, 900 °C		−3.00	234 and 476
Ni-YSZ/YSZ/GDC/$Pr_2Ni_{0.9}Co_{0.1}O_{4+\delta}$		50% H_2 + 50% H_2O, 800 °C		−1.75	474
		50% H_2 + 50% H_2O, 900 °C		−2.37	234 and 474
Ni-YSZ/YSZ/GDC/$Pr_2NiO_{4+\delta}$	93 (850 °C)	50% H_2 + 50% H_2O, 800 °C	0.128	−1.62	474 and 476
		50% H_2 + 50% H_2O, 900 °C		−2.09	234 and 476
Ni-YSZ/YSZ/GDC/$La_2Ni_{0.8}Co_{0.2}O_{4+\delta}$	51 (850 °C)	50% H_2 + 50% H_2O, 800 °C		−1.60	474 and 476
Ni-YSZ/YSZ/GDC/$La_2NiO_{4+\delta}$	43 (850 °C)	50% H_2 + 50% H_2O, 800 °C		−1.51	474 and 476
Ni-YSZ/YSZ/GDC/LSCF		50% H_2 + 50% H_2O, 800 °C		−1.50	476
		50% H_2 + 50% H_2O, 900 °C		−2.37	234 and 476
Ni-YSZ/YSZ/GDC/$Nd_2NiO_{4+\delta}$		50% H_2 + 50% H_2O, 800 °C		−1.62	474
Ni-YSZ/YSZ/GDC/$Nd_2Ni_{0.8}Co_{0.2}O_{4+\delta}$		50% H_2 + 50% H_2O, 800 °C		−1.80	474
Ni-YSZ/YSZ/GDC/$La_{1.5}Pr_{0.5}NiO_{4+\delta}$		50% H_2 + 50% H_2O, 800 °C		−1.60	474
Ni-YSZ/YSZ/GDC/$La_2Ni_{0.8}Co_{0.2}O_{4+\delta}$		50% H_2 + 50% H_2O, 800 °C		−1.79	474
La_2NiO_{4+}/GDC/8YSZ/GDC/$La_2NiO_{4+\delta}$	36 (800 °C)	100% air	0.142		240
$La_2Pr_{0.5}NiO_{4+\delta}$/GDC/8YSZ/GDC/$La_2Pr_{0.5}NiO_{4+\delta}$	48 (800 °C)	100% air	0.044		240
$La_2Pr_{1.0}NiO_{4+\ \delta}$/GDC/8YSZ/GDC/$La_2Pr_{1.0}NiO_{4+\delta}$	73 (800 °C)	100% air	0.017		240
$La_2Pr_{1.5}NiO_{4+\delta}$/GDC/8YSZ/GDC/$La_2Pr_{1.5}NiO_{4+\delta}$	81 (800 °C)	100% air	0.015		240
$La_2Pr_2NiO_{4+\delta}$/GDC/8YSZ/GDC/$La_2Pr_2NiO_{4+\delta}$	88 (800 °C)	100% air	0.010		240
$Pr_2NiO_{4+\delta}$/GDC/8YSZ/GDC/$Pr_2NiO_{4+\delta}$		100% air	0.010		227
$Pr_4Ni_3O_{4+\ \delta}$/GDC/8YSZ/GDC/$Pr_4Ni_3O_{4+\delta}$	86 (800 °C)	100% air	0.16 (600 °C)		314
$La_{0.6}Sr_{0.4}Fe_{0.8}Co_{0.2}O_{3-\delta}$/8YSZ/$La_{0.6}Sr_{0.4}Fe_{0.8}Co_{0.2}O_{3-\delta}$		100% air	0.05		477
$La_2NiO_{4+\delta}$/8YSZ/$La_2NiO_{4+\delta}$		100% air	0.37		477
$Pr_2NiO_{4+\delta}$/8YSZ/$Pr_2NiO_{4+\delta}$	100 (800 °C)	100% air	0.14		477

contact layer has only one electrical task, which is an appropriately less-resistant conduction of electrodes. The grains can thus be coarser, the microstructure can be more open-pored, and the thickness is typically higher than that of the electrode.

3.4.3. Sealants

3.4.3.1. Compressive sealants. Gastight seals are essential for SOC stack operation. They are fixed at the edges of each cell, at the edges of all stack layers, and at the gas manifold, thus separating the two gas atmospheres and electrically insulating the individual stacking layers. Compressive sealants require an external compressive load and a frame for even load distribution during SOC operation. Applying load on an SOC stack composed of brittle ceramic components can lead to crack formation. The sealant frames are exposed to an oxidative atmosphere and are therefore liable to material oxidation. Commonly used compressive sealants are mica-based and composed of SiO_4 sheets and metal gaskets (*e.g.*, Au m.p. 1063 °C), which can deform easily at high temperatures under load.[25] Additionally, compressive seals can be used between the stack itself and an adapter plate that connects the stack to either the SOC housing in a system or the furnace. Those sealants must be demountable in case of stack maintenance or replacement.

3.4.3.2. Glass (-ceramic) sealants. Sealants made of glass and glass-ceramic are commonly used in high-temperature SOC applications due to their good electrical insulation, chemical stability in reducing and oxidizing atmospheres, and appropriate thermal expansion behavior. Alkaline-earth metal oxides containing silicate or borosilicate glasses, for example, BaO–SiO_2–CaO, have been considered. However, they can exhibit interdiffusion with the Cr-containing interconnector when containing more than 40 mol% alkaline-earth metal oxides. This leads to the formation of an electrical conductive $ACrO_4$ (A = Ca, Sr, Ba) phase that is detrimental to the sealing properties and can be avoided through the additional thin coating on the interconnector.[41,461] Typically, these sealants are applied as a paste on the components and de-bindered, melted, and crystallized during stack heat-up. Glass-ceramics are preferred to pure amorphous glasses, as they have a higher strength and are not prone to flowing under load (either for securing gas tightness by external load or when overpressure is applied internally).

4. Conclusion

In this paper, the current progress in SOEC technology and the development of component materials are reviewed. The results show that high-temperature SOEC operation with a suitable current density and cell resistance can now be achieved with state-of-the-art materials as well as with novel materials. Up to now, most of the cell or stack component materials, such as electrodes, electrolytes, interconnects, and sealing and coating materials, have been considered in SOFC research. Therefore, the cells containing state-of-the-art oxygen and fuel electrode materials exhibit larger degradation in electrolysis mode compared to fuel cell mode. Nevertheless, alongside huge R&D efforts, start-up companies are currently developing HT-SOEC stacks (both FESCs and ESCs) and systems containing the state-of-the-art YSZ or GDC electrolytes, LSC/LSCF oxygen electrodes with a GDC barrier layer, and Ni-GDC or Ni-GDC fuel

electrodes capable for operating at 700–900 °C with >0.5–1.0 A cm^{-2}. Systems and stacks based on MSCs operated at medium-to-low temperatures (of around 650 °C) are currently under development due to significantly lower degradation rates.

One of the major challenges during HT-SOC operation is the long-term stability of electrodes during SOEC operation. Therefore, novel electrode materials and manufacturing methods for performance optimization (*e.g.*, exsolution) are investigated concerning performance and long-term stability.

On the oxygen electrode side, perovskite-type LSCF is currently used but exhibits Sr segregation due to the migration of the volatile SrO from the LSCF electrode to the GDC/electrolyte interface. There it forms an insulating $SrZrO_3$ phase, which in turn leads to cell degradation and performance loss. Alternative oxygen electrodes with layered perovskites (Ruddlesden–Popper nickelates, *e.g.*, $Ln_2NiO_{4+\delta}$, Ln = La, Pr or Nd) and a double perovskite structure ($Sr_2Fe_{2-x}Mo_xO_{6-\delta}$ and $LnBaCo_2O_{5+\delta}$ where Ln = La, Pr, Nd, Gd, Sm) have attracted a lot of scientific attention mainly due to their higher oxide ion diffusivity and surface exchange activity compared to conventional perovskite-based materials. For example, the performance of single cells containing $Pr_2NiO_{4+\delta}$ and co-doped $Pr_2NiO_{4+\delta}$ oxygen electrodes exhibit a higher current density compared to the LSCF electrode. In particular, the $Pr_2Ni_{0.8}Co_{0.2}O_{4+\delta}$ electrode shows a lower degradation rate of 22 mV kh^{-1} compared to the LSCF cell (88 mV kh^{-1}). Moreover, the microstructure of the oxygen electrode strongly affects the performance of the cell, for example, the $La_2NiO_{4+\delta}$ electrode with a coral microstructure prepared by the electrostatic spray deposition technique shows a lower polarization resistance (0.42 Ω cm^2) than the conventional screen-printed electrodes (0.93 Ω cm^2) at 600 °C. In addition, further improvement of cell performance can be achieved by using nanofibers and nanostructured electrodes. However, reproducibility tests, scale-up to stack-relevant sizes, and stack tests are still lacking.

With respect to the fuel electrode, Ni migration and agglomeration are the major concerns for the state-of-the-art Ni-YSZ electrode as well as the Ni-GDC electrode, during SOEC operation. These mechanisms detrimentally impact the electrode's microstructure and subsequently, lead to severe performance loss with increasing duration and operating time.

To avoid such concerns, several alternative perovskite electrode materials based on mixed ionic and electronic conductivity are proposed, such as lanthanum strontium chromium manganite (LSCM), lanthanum strontium iron manganite (LSFM), lanthanum strontium titanate (LST), strontium iron molybdate (SFM), strontium iron niobate (SFN), and praseodymium-doped barium iron molybdate (PBFM). These materials show good thermal expansion behavior, chemical and redox stability, and conductivity at high operating temperatures and under reducing conditions. However, these new materials still exhibit limitations in catalytic activity, therefore material development and initial cell performance testing have to be conducted further. Regardless of promising initial tests of the cell performance for selected materials, their long-term stability is still unknown, which is the focus point for their large-scale and system-level implementation.

Despite the sufficient performance for state-of-the-art materials in industrial high-temperature SOEC stacks, the aspect of the materials' lifetime and stability remains a challenge, especially with regard to future widespread applications and increased market interest. Therefore, to achieve improved SOEC system lifetime, existing materials need to be modified and highly active materials need to be developed. This review of alternative electrode materials underlined the lack of long-term (>5000 h) durability tests, which will be necessary to assess their technology readiness level for future commercialization.

Conflicts of interest

The authors declare no conflicts of interest.

Acknowledgements

The authors gratefully acknowledge funding provided by the German Federal Ministry of Education and Research (BMBF) within the SOC-Degradation 2.0 project: transfer of knowledge into products for a “green hydrogen” vector—impedance analysis of intrinsic and extrinsic degradation mechanisms in SOC cells and repeat units (FKZ 03SF0621A). The authors would also like to thank S. B. C. Lehmann for the graphical support.

References

1 *Global Hydrogen Review 2021*, Paris, 2020.
2 Clean Hydrogen Partnership, *Annual Work Programme for 2023*, 2023.
3 M. Wappler, D. Unguder, X. Lu, H. Ohlmeyer, H. Teschke and W. Lueke, *Int. J. Hydrogen Energy*, 2022, **47**, 33551–33570.
4 M. Carmo, D. L. Fritz, J. Mergel and D. Stolten, *Int. J. Hydrogen Energy*, 2013, **38**, 4901–4934.
5 F. M. Sapountzi, J. M. Gracia, C. J. Weststrate, H. O. Fredriksson and J. W. Niemantsverdriet, *Prog. Energy Combust. Sci.*, 2017, **58**, 1–35.
6 S. Slade, S. A. Campbell, T. R. Ralph and F. C. Walsh, *J. Electrochem. Soc.*, 2002, **149**, A1556.
7 I. Vincent and D. Bessarabov, *Renewable Sustainable Energy Rev.*, 2018, **81**, 1690–1704.
8 H. A. Miller, K. Bouzek, J. Hnat, S. Loos, C. I. Bernäcker, T. Weißgärber, L. Röntzsch and J. Meier-Haack, *Sustainable Energy Fuels*, 2020, **4**, 2114–2133.
9 M. Nasser, T. F. Megahed, S. Ookawara and H. Hassan, *Environ. Sci. Pollut. Res. Int.*, 2022, **29**, 86994–87018.
10 H. Lange, A. Klose, W. Lippmann and L. Urbas, *Int. J. Hydrogen Energy*, 2023, **48**, 15771–15783.
11 M. E. Ivanova, R. Peters, M. Müller, S. Haas, M. F. Seidler, G. Mutschke, K. Eckert, P. Röse, S. Calnan, R. Bagacki, R. Schlatmann, C. Grosselindemann, L.-A. Schäfer, N. H. Menzler, A. Weber, R. van de Krol, F. Liang, F. F. Abdi, S. Brendelberger, N. Neumann, J. Grobbel, M. Roeb, C. Sattler, I. Duran, B. Dietrich, M. E. C. Hofberger, L. Stoppel, N. Uhlenbruck, T. Wetzel,

D. Rauner, A. Hecimovic, U. Fantz, N. Kulyk, J. Harting and O. Guillon, *Angew. Chem., Int. Ed.*, 2023, e202218850.
12 J. Cao, Y. Ji and Z. Shao, *Energy Environ. Sci.*, 2022, **15**, 2200–2232.
13 S. R. Foit, I. C. Vinke, L. G. J. de Haart and R.-A. Eichel, *Angew. Chem., Int. Ed.*, 2017, **56**, 5402–5411.
14 Y. Zheng, J. Wang, B. Yu, W. Zhang, J. Chen, J. Qiao and J. Zhang, *Chem. Soc. Rev.*, 2017, **46**, 1427–1463.
15 S. E. Wolf, L. Dittrich, M. Nohl, T. Duyster, I. C. Vinke, R.-A. Eichel and L. de Haart, *J. Electrochem. Soc.*, 2022, **169**, 034531.
16 S. Foit, L. Dittrich, T. Duyster, I. Vinke, R.-A. Eichel and L. G. J. de Haart, *Process*, 2020, **8**, 1390.
17 L. Dittrich, M. Nohl, E. E. Jaekel, S. Foit, L. de Haart and R.-A. Eichel, *J. Electrochem. Soc.*, 2019, **166**, F971–F975.
18 J. Artz, T. E. Müller, K. Thenert, J. Kleinekorte, R. Meys, A. Sternberg, A. Bardow and W. Leitner, *Chem. Rev.*, 2018, **118**, 434–504.
19 R. Schlögl, *ChemSusChem*, 2010, **3**, 209–222.
20 R. Franke, D. Selent and A. Börner, *Chem. Rev.*, 2012, **112**, 5675–5732.
21 S. H. Jensen, P. H. Larsen and M. Mogensen, *Int. J. Hydrogen Energy*, 2007, **32**, 3253–3257.
22 C. Graves, S. D. Ebbesen, M. Mogensen and K. S. Lackner, *Renewable Sustainable Energy Rev.*, 2011, **15**, 1–23.
23 GrInHy – Green Industrial Hydrogen via Reversible High-Temperature Electrolysis, 2016–2019.
24 GrInHy2.0 – Green Industrial Hydrogen via steam electrolysis. Erzeugung von erneuerbarem Wasserstoff in einem Stahlwerk, 2019–2022.
25 R. Peters, M. Frank, W. Tiedemann, I. Hoven, R. Deja, N. Kruse, Q. Fang, L. Blum and R. Peters, *J. Electrochem. Soc.*, 2021, **168**, 14508.
26 M. Frank, R. Deja, R. Peters, L. Blum and D. Stolten, *Appl. Energy*, 2018, **217**, 101–112.
27 R. Peters, R. Deja, M. Engelbracht, M. Frank, N. van Nguyen, L. Blum and D. Stolten, *J. Power Sources*, 2016, **328**, 105–113.
28 R. Peters, W. Tiedemann, I. Hoven, R. Deja, N. Kruse, Q. Fang, L. Blum and R. Peters, *ECS Trans.*, 2021, **103**, 289–297.
29 N. Kruse, W. Tiedemann, I. Hoven, R. Deja, R. Peters, L. Blum and R. Peters, *ECS Trans.*, 2021, **103**, 555–560.
30 Q. Fang, L. Blum and D. Stolten, *J. Electrochem. Soc.*, 2019, **166**, F1320–F1325.
31 V. N. Nguyen, Q. Fang, U. Packbier and L. Blum, *Int. J. Hydrogen Energy*, 2013, **38**, 4281–4290.
32 J. Schefold, A. Brisse, M. Zahid, J. P. Ouweltjes and J. U. Nielsen, *ECS Trans.*, 2011, **35**, 2915–2927.
33 X. Zhang, J. E. O'Brien, R. C. O'Brien, J. J. Hartvigsen, G. Tao and G. K. Housley, *Int. J. Hydrogen Energy*, 2013, **38**, 20–28.
34 S. Megel, C. Dosch, S. Rothe, C. Folgner, N. Trofimenko, A. Rost, M. Kusnezoff, E. Reichelt, M. Jahn, A. Michaelis, C. Bienert and M. Brandner, *ECS Trans.*, 2017, **78**, 3089–3102.
35 A. Léon, A. Micero, B. Ludwig and A. Brisse, *J. Power Sources*, 2021, **510**, 230346.
36 M. Lang, S. Raab, M. S. Lemcke, C. Bohn and M. Pysik, *ECS Trans.*, 2019, **91**, 2713–2725.
37 Q. Fang, C. E. Frey, N. H. Menzler and L. Blum, *J. Electrochem. Soc.*, 2018, **165**, F38–F45.
38 G. Rinaldi, S. Diethelm, E. Oveisi, P. Burdet, J. van Herle, D. Montinaro, Q. Fu and A. Brisse, *Fuel Cells*, 2017, **17**, 541–549.
39 M. Bianco, J. P. Ouweltjes and J. van Herle, *Int. J. Hydrogen Energy*, 2019, **44**, 31406–31422.
40 A. Beez, K. Schiemann, N. H. Menzler and M. Bram, *Front. Energy Res.*, 2018, **6**, 70.
41 K. Singh and T. Walia, *Int. J. Energy Res.*, 2021, **45**, 20559–20582.
42 D. The, S. Grieshammer, M. Schroeder, M. Martin, M. Al Daroukh, F. Tietz, J. Schefold and A. Brisse, *J. Power Sources*, 2015, **275**, 901–911.
43 F. Monaco, D. Ferreira-Sanchez, M. Hubert, B. Morel, D. Montinaro, D. Grolimund and J. Laurencin, *Int. J. Hydrogen Energy*, 2021, **46**, 31533–31549.
44 Z. Li, M. Peng, Y. Zhu, Z. Hu, C.-W. Pao, Y.-C. Chang, Y. Zhang, Y. Zhao, J. Li and Y. Sun, *J. Mater. Chem. A*, 2022, **10**, 20350–20364.
45 S. Zarabi Golkhatmi, M. I. Asghar and P. D. Lund, *Renewable Sustainable Energy Rev.*, 2022, **161**, 112339.
46 S. K. Sahu, D. Panthi, I. Soliman, H. Feng and Y. Du, *Energies*, 2022, **15**, 3536.
47 N. Q. Minh, in *High-Temperature Solid Oxide Fuel Cells for the 21st Century*, Elsevier, 2016, pp. 255–282.
48 N. M. Sammes, Y. Du and R. Bove, *J. Power Sources*, 2005, **145**, 428–434.
49 M. Ni, M. Leung and D. Leung, *Int. J. Hydrogen Energy*, 2008, **33**, 2337–2354.
50 C. Lenser, D. Udomsilp, N. H. Menzler, P. Holtappels, T. Fujisaki, L. Kwati, H. Matsumoto, A. G. Sabato, F. Smeacetto, A. Chrysanthou and S. Molin, in *Advanced Ceramics for Energy Conversion and Storage*, Elsevier, 2020, pp. 387–547.
51 F. Grimm, PhD thesis, Schriften des Forschungszentrums Jülich, Reihe Energie & Umwelt/Energy & Environment, RWTH Aachen University, 2020,vol. 498.
52 M. P. Hoerlein, M. Riegraf, R. Costa, G. Schiller and K. A. Friedrich, *Electrochim. Acta*, 2018, **276**, 162–175.
53 L. Wehrle, D. Schmider, J. Dailly, A. Banerjee and O. Deutschmann, *Appl. Energy*, 2022, **317**, 119143.
54 D. Sarantaridis and A. Atkinson, *Fuel Cells*, 2007, **7**, 246–258.
55 C. Walter, O. Posdziech and M. Boltze, in *EFCF 2022 Proceedings of the Conference. A Sessions*, ed. O. Bucheli, G. Geisser, F. Moore and M. Spirig, 2022, p. A0501.
56 M. C. Tucker, *J. Power Sources*, 2010, **195**, 4570–4582.
57 M. Noponen, H. Granö-Fabritius, S. Pylypko and E. Õunpuu, in *EFCF 2022 Proceedings of the Conference. A Sessions*, ed. O. Bucheli, G. Geisser, F. Moore and M. Spirig, 2022, p. A0503.
58 A. Hagen, R. Caldogno, F. Capotondo and X. Sun, *Energies*, 2022, **15**, 2045.

59 M. Zhang, E. Wang, J. Mao, H. Wang, M. Ouyang and H. Hu, *Front. Energy Res.*, 2022, **10**, 888787.
60 G. Schiller, R. Costa and K. A. Friedrich, in *Ceramics for Energy Conversion, Storage, and Distribution Systems*, ed. T. Pfeifer, J. Matyáš, P. Balaya, D. Singh and J. Wei, John Wiley & Sons, Inc, Hoboken, NJ, USA, 2016, pp. 19–27.
61 D. Udomsilp, J. Rechberger, R. Neubauer, C. Bischof, F. Thaler, W. Schafbauer, N. H. Menzler, L. G. de Haart, A. Nenning, A. K. Opitz, O. Guillon and M. Bram, *Cell Rep. Phys. Sci.*, 2020, **1**, 100072.
62 F. Grimm, N. H. Menzler and O. Guillon, *J. Power Sources*, 2020, **451**, 227607.
63 M. C. Tucker, *Int. J. Hydrogen Energy*, 2020, **45**, 24203–24218.
64 J. Harman, P. Hjalmarsson, J. Mermelstein, J. Ryley, H. Sadler and M. Selby, *ECS Trans.*, 2021, **103**, 383–392.
65 B. Zhu, I. Albinsson, C. Andersson, K. Borsand, M. Nilsson and B.-E. Mellander, *Electrochem. Commun.*, 2006, **8**, 495–498.
66 N. Mahato, A. Banerjee, A. Gupta, S. Omar and K. Balani, *Prog. Mater. Sci.*, 2015, **72**, 141–337.
67 A. J. Jacobson, *Chem. Mater.*, 2010, **22**, 660–674.
68 J. Zhang, C. Lenser, N. H. Menzler and O. Guillon, *Solid State Ionics*, 2020, **344**, 115138.
69 N. Q. Minh, *J. Am. Ceram. Soc.*, 1993, **76**, 563–588.
70 Y. Arachi, *Solid State Ionics*, 1999, **121**, 133–139.
71 O. Posdziech, K. Schwarze and J. Brabandt, *Int. J. Hydrogen Energy*, 2019, **44**, 19089–19101.
72 C. Geipel, K. Hauptmeier, K. Herbrig, F. Mittmann, M. Münch, M. Pötschke, L. Reichel, T. Strohbach, T. Seidel, A. Surrey and C. Walter, *ECS Trans.*, 2019, **91**, 123–132.
73 M. Lang, M. Braig, N. Alqubati and P. Szabo, *ECS Trans.*, 2021, **103**, 2041–2051.
74 M. Ghatee, M. H. Shariat and J. Irvine, *Solid State Ionics*, 2009, **180**, 57–62.
75 T. Politova, *Solid State Ionics*, 2004, **168**, 153–165.
76 S. Hussain and L. Yangping, *Energy Transition*, 2020, **4**, 113–126.
77 X. Guan, H. Zhou, Y. Wang and J. Zhang, *J. Alloys Compd.*, 2008, **464**, 310–316.
78 V. V. Kharton, F. M. Figueiredo, L. Navarro, E. N. Naumovich, A. V. Kovalevsky, A. A. Yaremchenko, A. P. Viskup, A. Carneiro, F. M. B. Marques and J. R. Frade, *J. Mater. Sci.*, 2001, **36**, 1105–1117.
79 Q. Fang, L. Blum and N. H. Menzler, *J. Electrochem. Soc.*, 2015, **162**, F907–F912.
80 D. Schäfer, Q. Fang, L. Blum and D. Stolten, *J. Power Sources*, 2019, **433**, 126666.
81 Q. Fu, J. Schefold, A. Brisse and J. U. Nielsen, *Fuel Cells*, 2014, **14**, 395–402.
82 S. D. Ebbesen, J. Høgh, K. A. Nielsen, J. U. Nielsen and M. Mogensen, *Int. J. Hydrogen Energy*, 2011, **36**, 7363–7373.
83 J. Mougin, A. Mansuy, A. Chatroux, G. Gousseau, M. Petitjean, M. Reytier and F. Mauvy, *Fuel Cells*, 2013, **13**, 623–630.
84 M. Petitjean, M. Reytier, A. Chatroux, L. Bruguière, A. Mansuy, H. Sassoulas, S. Di Iorio, B. Morel and J. Mougin, *ECS Trans.*, 2011, **35**, 2905–2913.
85 M. Reytier, S. Di Iorio, A. Chatroux, M. Petitjean, J. Cren, M. de Saint Jean, J. Aicart and J. Mougin, *Int. J. Hydrogen Energy*, 2015, **40**, 11370–11377.
86 S. H. Jensen, H. Langnickel, N. Hintzen, M. Chen, X. Sun, A. Hauch, G. Butera and L. R. Clausen, *J. Energy Storage*, 2019, **22**, 106–115.
87 M. Riedel, M. P. Heddrich, A. Ansar, Q. Fang, L. Blum and K. A. Friedrich, *J. Power Sources*, 2020, **475**, 228682.
88 M. Riedel, M. P. Heddrich and K. A. Friedrich, *Fuel Cells*, 2020, **20**, 592–607.
89 G. Corre and A. Brisse, *ECS Trans.*, 2015, **68**, 3481–3490.
90 L. León-Reina, E. R. Losilla, M. Martínez-Lara, S. Bruque and M. A. G. Aranda, *J. Mater. Chem.*, 2004, **14**, 1142–1149.
91 T. K. Schultze, J. P. Arnold and S. Grieshammer, *ACS Appl. Energy Mater.*, 2019, **2**, 4708–4717.
92 S. Nakayama, M. Sakamoto, M. Highchi and K. Kodaira, *J. Mater. Sci. Lett.*, 2000, **19**, 91–93.
93 S. Nakayama and M. Highchi, *J. Mater. Sci. Lett.*, 2001, **20**, 913–915.
94 M. Higuchi, H. Katase, K. Kodaira and S. Nakayama, *J. Cryst. Growth*, 2000, **218**, 282–286.
95 S. Nakayama, M. Sakamoto, M. Higuchi, K. Kodaira, M. Sato, S. Kakita, T. Suzuki and K. Itoh, *J. Eur. Ceram. Soc.*, 1999, **19**, 507–510.
96 T. Liao, T. Sasaki and Z. Sun, *Phys. Chem. Chem. Phys.*, 2013, **15**, 17553–17559.
97 E. Kendrick, M. S. Islam and P. R. Slater, *J. Mater. Chem.*, 2007, **17**, 3104.
98 H. Arikawa, *Solid State Ionics*, 2000, **136–137**, 31–37.
99 J. M. Porras-Vázquez, E. R. Losilla, L. León-Reina, D. Marrero-López and M. A. Aranda, *J. Am. Ceram. Soc.*, 2009, **92**, 1062–1068.
100 N. Liu, M. Shi, C. Wang, Y. P. Yuan, P. Majewski and F. Aldinger, *J. Mater. Sci.*, 2006, **41**, 4205–4213.
101 J. W. Fergus, *J. Power Sources*, 2006, **162**, 30–40.
102 S. Badwal, *Solid State Ionics*, 2001, **143**, 39–46.
103 E. Ivers-Tiffée, A. Weber and D. Herbstritt, *J. Eur. Ceram. Soc.*, 2001, **21**, 1805–1811.
104 S. Badwal, *Solid State Ionics*, 2000, **136–137**, 91–99.
105 P. Lacorre, F. Goutenoire, O. Bohnke, R. Retoux and Y. Laligant, *Nature*, 2000, **404**, 856–858.
106 L. León-Reina, E. R. Losilla, M. Martínez-Lara, M. C. Martín-Sedeño, S. Bruque, P. Núñez, D. V. Sheptyakov and M. A. G. Aranda, *Chem. Mater.*, 2005, **17**, 596–600.
107 K. Huang, M. Feng and J. B. Goodenough, *J. Am. Ceram. Soc.*, 1998, **81**, 357–362.
108 K. Huang, R. S. Tichy and J. B. Goodenough, *J. Am. Ceram. Soc.*, 1998, **81**, 2565–2575.
109 J. Zhang, C. Lenser, N. Russner, A. Weber, N. H. Menzler and O. Guillon, *J. Am. Ceram. Soc.*, 2023, **106**, 93–99.
110 T. Jacobsen and M. Mogensen, *ECS Trans.*, 2008, **13**, 259–273.

111 H. Bouwmeester, H. Kruidhof and A. J. Burggraaf, *Solid State Ionics*, 1994, **72**, 185–194.
112 S. B. Adler, J. A. Lane and B. C. H. Steele, *J. Electrochem. Soc.*, 1996, **143**, 3554–3564.
113 A. V. Nikonov, K. A. Kuterbekov, K. Bekmyrza and N. B. Pavzderin, *Eurasian J. Phys. Funct. Mater.*, 2018, **2**, 274–292.
114 E. V. Tsipis and V. V. Kharton, *J. Solid State Electrochem.*, 2008, **12**, 1039–1060.
115 M. Al Daroukh, *Solid State Ionics*, 2003, **158**, 141–150.
116 C. Yao, J. Meng, X. Liu, X. Zhang, F. Meng, X. Wu and J. Meng, *Electrochim. Acta*, 2017, **229**, 429–437.
117 U. de Haart, Q. Fang, N. H. Menzler and R. Peters, in *EFCF 2022 Proceedings of the Conference*, vol. 15, pp. 221–230.
118 M. Yuste, J. C. Pérez-Flores, J. R. de Paz, M. T. Azcondo, F. García-Alvarado and U. Amador, *Dalton Trans.*, 2011, **40**, 7908–7915.
119 H. Kozuka, K. Ohbayashi and K. Koumoto, *Sci. Technol. Adv. Mater.*, 2015, **16**, 26001.
120 J. Sunarso, S. S. Hashim, N. Zhu and W. Zhou, *Prog. Energy Combust. Sci.*, 2017, **61**, 57–77.
121 D. Marinha, J. Hayd, L. Dessemond, E. Ivers-Tiffée and E. Djurado, *J. Power Sources*, 2011, **196**, 5084–5090.
122 K. Momma and F. Izumi, *J. Appl. Crystallogr.*, 2011, **44**, 1272–1276.
123 Y. Song, X. Zhang, K. Xie, G. Wang and X. Bao, *Adv. Mater.*, 2019, **31**, e1902033.
124 Y. Li, R. Gemmen and X. Liu, *J. Power Sources*, 2010, **195**, 3345–3358.
125 S. P. Jiang, *J. Mater. Sci.*, 2008, **43**, 6799–6833.
126 S. Carter, *Solid State Ionics*, 1992, **53–56**, 597–605.
127 I. Yasuda, *Solid State Ionics*, 1996, **86–88**, 1197–1201.
128 J.-H. Kim, R.-H. Song, J.-H. Kim, T.-H. Lim, Y.-K. Sun and D.-R. Shin, *J. Solid State Electrochem.*, 2007, **11**, 1385–1390.
129 A. Princivalle and E. Djurado, *Solid State Ionics*, 2008, **179**, 1921–1928.
130 J. R. Wilson, J. S. Cronin, A. T. Duong, S. Rukes, H.-Y. Chen, K. Thornton, D. R. Mumm and S. Barnett, *J. Power Sources*, 2010, **195**, 1829–1840.
131 Z. Liu, X. Zhang, Z. Huang, Z. Zhao, D. Cui and M. Cheng, *Int. J. Hydrogen Energy*, 2016, **41**, 21385–21393.
132 A. Barnabé, M. Gaudon, C. Bernard, C. Laberty and B. Durand, *Mater. Res. Bull.*, 2004, **39**, 725–735.
133 F. Licci, G. Turilli, P. Ferro and A. Ciccarone, *J. Am. Ceram. Soc.*, 2003, **86**, 413–419.
134 W. Wang, Y. Huang, S. Jung, J. M. Vohs and R. J. Gorte, *J. Electrochem. Soc.*, 2006, **153**, A2066.
135 J. Schefold, A. Brisse and F. Tietz, *J. Electrochem. Soc.*, 2011, **159**, A137–A144.
136 A. Petric, *Solid State Ionics*, 2000, **135**, 719–725.
137 H. Tu, Y. Takeda, N. Imanishi and O. Yamamoto, *Solid State Ionics*, 1999, **117**, 277–281.
138 H. Ullmann, N. Trofimenko, F. Tietz, D. Stöver and A. Ahmad-Khanlou, *Solid State Ionics*, 2000, **138**, 79–90.
139 F. Prado, T. Armstrong, A. Caneiro and A. Manthiram, *J. Electrochem. Soc.*, 2001, **148**, J7.
140 Y. Leng, S. Chan and Q. Liu, *Int. J. Hydrogen Energy*, 2008, **33**, 3808–3817.
141 M. Zahid, *Proc. Vol.*, 2005, **2005–2007**, 1708–1716.
142 S. Jiang, *Solid State Ionics*, 2002, **146**, 1–22.
143 R. de Souza, J. Kilner and J. Walker, *Mater. Lett.*, 2000, **43**, 43–52.
144 S. P. Jiang, *Int. J. Hydrogen Energy*, 2019, **44**, 7448–7493.
145 S. T. Aruna, M. Muthuraman and K. C. Patil, *J. Mater. Chem.*, 1997, **7**, 2499–2503.
146 F. Tietz, I. Arulraj, M. Zahid and D. Stover, *Solid State Ionics*, 2006, **177**, 1753–1756.
147 Y. Ji, J. Kilner and M. Carolan, *Solid State Ionics*, 2005, **176**, 937–943.
148 B. Steele, *Solid State Ionics*, 1996, **86–88**, 1223–1234.
149 S. Fearn, J. Rossiny, J. A. Kilner and J. Evans, *Solid State Ionics*, 2012, **211**, 51–57.
150 A. V. Berenov, A. Atkinson, J. A. Kilner, E. Bucher and W. Sitte, *Solid State Ionics*, 2010, **181**, 819–826.
151 V. V. Kharton, E. N. Naumovich, A. A. Vecher and A. V. Nikolaev, *J. Solid State Chem.*, 1995, **120**, 128–136.
152 A. Egger, E. Bucher, M. Yang and W. Sitte, *Solid State Ionics*, 2012, **225**, 55–60.
153 M. Katsuki, *Solid State Ionics*, 2003, **156**, 453–461.
154 L. Tai, *Solid State Ionics*, 1995, **76**, 273–283.
155 A. Mineshige, J. Izutsu, M. Nakamura, K. Nigaki, J. Abe, M. Kobune, S. Fujii and T. Yazawa, *Solid State Ionics*, 2005, **176**, 1145–1149.
156 B. Steele, *Solid State Ionics*, 1998, **106**, 255–261.
157 P. Woodward, R.-D. Hoffmann and A. W. Sleight, *J. Mater. Res.*, 1994, **9**, 2118–2127.
158 G. King and P. M. Woodward, *J. Mater. Chem.*, 2010, **20**, 5785.
159 C. Meneghini, S. Ray, F. Liscio, F. Bardelli, S. Mobilio and D. D. Sarma, *Phys. Rev. Lett.*, 2009, **103**, 46403.
160 D. Serrate, J. M. de Teresa and M. R. Ibarra, *J. Phys.: Condens. Matter*, 2007, **19**, 23201.
161 A. A. Markov, I. A. Leonidov, M. V. Patrakeev, V. L. Kozhevnikov, O. A. Savinskaya, U. V. Ancharova and A. P. Nemudry, *Solid State Ionics*, 2008, **179**, 1050–1053.
162 O. Savinskaya and A. P. Nemudry, *J. Solid State Electrochem.*, 2011, **15**, 269–275.
163 G. Y. Liu, G. H. Rao, X. M. Feng, H. F. Yang, Z. W. Ouyang, W. F. Liu and J. K. Liang, *J. Alloys Compd.*, 2003, **353**, 42–47.
164 G. Xiao, Q. Liu, X. Dong, K. Huang and F. Chen, *J. Power Sources*, 2010, **195**, 8071–8074.
165 L. Zhang, Q. Zhou, Q. He and T. He, *J. Power Sources*, 2010, **195**, 6356–6366.
166 Q. Liu, X. Dong, G. Xiao, F. Zhao and F. Chen, *Adv. Mater.*, 2010, **22**, 5478–5482.
167 J. Rager, M. Zipperle, A. Sharma and J. L. MacManus-Driscoll, *J. Am. Ceram. Soc.*, 2004, **87**, 1330–1335.
168 Q. Liu, D. E. Bugaris, G. Xiao, M. Chmara, S. Ma, H.-C. zur Loye, M. D. Amiridis and F. Chen, *J. Power Sources*, 2011, **196**, 9148–9153.
169 Y. Teraoka, H. M. Zhang, K. Okamoto and N. Yamazoe, *Mater. Res. Bull.*, 1988, **23**, 51–58.

170 A. B. Muñoz-García, D. E. Bugaris, M. Pavone, J. P. Hodges, A. Huq, F. Chen, H.-C. zur Loye and E. A. Carter, *J. Am. Ceram. Soc.*, 2012, **134**, 6826–6833.
171 B. He, L. Zhao, S. Song, T. Liu, F. Chen and C. Xia, *J. Electrochem. Soc.*, 2012, **159**, B619–B626.
172 C. Tian, J. Cheng and J. Yang, *J. Mater. Sci.: Mater. Electron.*, 2021, **32**, 1258–1264.
173 C. Sun, R. Hui and J. Roller, *J. Solid State Electrochem.*, 2010, **14**, 1125–1144.
174 G. Xiao, Q. Liu, F. Zhao, L. Zhang, C. Xia and F. Chen, *J. Electrochem. Soc.*, 2011, **158**, B455.
175 D. A. Osinkin, A. V. Khodimchuk, N. M. Porotnikova, N. M. Bogdanovich, A. V. Fetisov and M. V. Ananyev, *Energies*, 2020, **13**, 250.
176 M. Sahibzada, *Solid State Ionics*, 2000, **136–137**, 991–996.
177 W. Sitte, *Solid State Ionics*, 2002, **154–155**, 517–522.
178 K. Huang, M. Feng, J. B. Goodenough and C. Milliken, *J. Electrochem. Soc.*, 1997, **144**, 3620–3624.
179 Q. Liu, C. Yang, X. Dong and F. Chen, *Int. J. Hydrogen Energy*, 2010, **35**, 10039–10044.
180 Y. Wang, T. Liu, S. Fang and F. Chen, *J. Power Sources*, 2016, **305**, 240–248.
181 S. Hou and K. Xie, *Electrochim. Acta*, 2019, **301**, 63–68.
182 L. Bernadet, C. Moncasi, M. Torrell and A. Tarancón, *Int. J. Hydrogen Energy*, 2020, **45**, 14208–14217.
183 A. Maignan, C. Martin, D. Pelloquin, N. Nguyen and B. Raveau, *J. Solid State Chem.*, 1999, **142**, 247–260.
184 V. Caignaert, I. Mirebeau, F. Bourée, N. Nguyen, A. Ducouret, J.-M. Greneche and B. Raveau, *J. Solid State Chem.*, 1995, **114**, 24–35.
185 I. O. Troyanchuk, N. V. Kasper, D. D. Khalyavin, H. Szymczak, R. Szymczak and M. Baran, *Phys. Rev. B: Condens. Matter Mater. Phys.*, 1998, **58**, 2418–2421.
186 P. S. Anderson, C. A. Kirk, J. Knudsen, I. M. Reaney and A. R. West, *Solid State Sci.*, 2005, **7**, 1149–1156.
187 K. Zhang, L. Ge, R. Ran, Z. Shao and S. Liu, *Acta Mater.*, 2008, **56**, 4876–4889.
188 A. Tarancón, S. J. Skinner, R. J. Chater, F. Hernández-Ramírez and J. A. Kilner, *J. Mater. Chem.*, 2007, **17**, 3175.
189 G. Kim, S. Wang, A. J. Jacobson, L. Reimus, P. Brodersen and C. A. Mims, *J. Mater. Chem.*, 2007, **17**, 2500.
190 S. Bao, C. Ma, G. Chen, X. Xu, E. Enriquez, C. Chen, Y. Zhang, J. L. Bettis, M.-H. Whangbo, C. Dong and Q. Zhang, *Sci. Rep.*, 2014, **4**, 4726.
191 G. Kim, S. Wang, A. Jacobson, L. Reimus, P. Brodersen and C. Mims, *Meeting Abstracts*, 2006, **MA2005-02**, p. 836.
192 Y. Wan, Y. Xing, Y. Li, D. Huan and C. Xia, *J. Power Sources*, 2018, **402**, 363–372.
193 F. Tietz, *Ionics*, 1999, **5**, 129–139.
194 Y. Zhang, L. Shen, Y. Wang, Z. Du, B. Zhang, F. Ciucci and H. Zhao, *J. Mater. Chem. A*, 2022, **10**, 3495–3505.
195 D. Chen, R. Ran, K. Zhang, J. Wang and Z. Shao, *J. Power Sources*, 2009, **188**, 96–105.
196 J. Wang, F. Meng, T. Xia, Z. Shi, J. Lian, C. Xu, H. Zhao, J.-M. Bassat and J.-C. Grenier, *Int. J. Hydrogen Energy*, 2014, **39**, 18392–18404.
197 G. Kostogloudis and C. Ftikos, *Solid State Ionics*, 1999, **126**, 143–151.
198 W. Zhou, R. Ran, Z. Shao, W. Jin and N. Xu, *J. Power Sources*, 2008, **182**, 24–31.
199 S. Jiang, W. Zhou, Y. Niu, Z. Zhu and Z. Shao, *ChemSusChem*, 2012, **5**, 2023–2031.
200 Z. Shao and S. M. Haile, in *Materials for Sustainable Energy*, ed. V. Dusastre, Co-Published with Macmillan Publishers Ltd, UK, 2010, pp. 255–258.
201 E. Boehm, J.-M. Bassat, M. C. Steil, P. Dordor, F. Mauvy and J.-C. Grenier, *Solid State Sci.*, 2003, **5**, 973–981.
202 C. Munnings, S. Skinner, G. Amow, P. Whitfield and I. Davidson, *Solid State Ionics*, 2005, **176**, 1895–1901.
203 A. Flura, S. Dru, C. Nicollet, V. Vibhu, S. Fourcade, E. Lebraud, A. Rougier, J.-M. Bassat and J.-C. Grenier, *J. Solid State Chem.*, 2015, **228**, 189–198.
204 A. Flura, C. Nicollet, V. Vibhu, B. Zeimetz, A. Rougier, J.-M. Bassat and J.-C. Grenier, *J. Electrochem. Soc.*, 2016, **163**, F523–F532.
205 S. Saher, J. Song, V. Vibhu, C. Nicollet, A. Flura, J.-M. Bassat and H. J. M. Bouwmeester, *J. Mater. Chem. A*, 2018, **6**, 8331–8339.
206 M. Medarde and J. Rodríguez-Carvajal, *Z. Phys. B*, 1997, **102**, 307–315.
207 J. C. Park, D. K. Kim, S. H. Byeon and D. Kim, *J. Synchrotron Radiat.*, 2001, **8**, 704–706.
208 Z. Zhang and M. Greenblatt, *J. Solid State Chem.*, 1995, **117**, 236–246.
209 J. Wu, S. S. Pramana, S. J. Skinner, J. A. Kilner and A. P. Horsfield, *J. Mater. Chem. A*, 2015, **3**, 23760–23767.
210 T. Broux, C. Prestipino, M. Bahout, S. Paofai, E. Elkaïm, V. Vibhu, J.-C. Grenier, A. Rougier, J.-M. Bassat and O. Hernandez, *Dalton Trans.*, 2016, **45**, 3024–3033.
211 L. Minervini, R. W. Grimes, J. A. Kilner and K. E. Sickafus, *J. Mater. Chem.*, 2000, **10**, 2349–2354.
212 V. V. Kharton, A. P. Viskup, A. V. Kovalevsky, E. N. Naumovich and F. Marques, *Solid State Ionics*, 2001, **143**, 337–353.
213 V. V. Kharton, A. P. Viskup, E. N. Naumovich and F. M. B. Marques, *J. Mater. Chem.*, 1999, **9**, 2623–2629.
214 J.-M. Bassat, M. Burriel, O. Wahyudi, R. Castaing, M. Ceretti, P. Veber, I. Weill, A. Villesuzanne, J.-C. Grenier, W. Paulus and J. A. Kilner, *J. Phys. Chem. C*, 2013, **117**, 26466–26472.
215 M. Burriel, G. Garcia, J. Santiso, J. A. Kilner, R. J. Chater and S. J. Skinner, *J. Mater. Chem.*, 2008, **18**, 416–422.
216 E. Boehm, J. Bassat, P. Dordor, F. Mauvy, J. Grenier and P. Stevens, *Solid State Ionics*, 2005, **176**, 2717–2725.
217 V. Vibhu, I. C. Vinke, R.-A. Eichel and L. de Haart, *J. Power Sources*, 2021, **482**, 228909.
218 L.-P. Sun, Q. Li, H. Zhao, L.-H. Huo and J.-C. Grenier, *J. Power Sources*, 2008, **183**, 43–48.
219 A. Chroneos, D. Parfitt, J. A. Kilner and R. W. Grimes, *J. Mater. Chem.*, 2010, **20**, 266–270.
220 R. J. Woolley and S. J. Skinner, *Solid State Ionics*, 2014, **255**, 1–5.

221 M. Ferkhi, A. Ringuedé, A. Khaled, L. Zerroual and M. Cassir, *Electrochim. Acta*, 2012, **75**, 80–87.
222 M. Rieu, R. Sayers, M. A. Laguna-Bercero, S. J. Skinner, P. Lenormand and F. Ansart, *J. Electrochem. Soc.*, 2010, **157**, B477.
223 S. Skinner, *Solid State Ionics*, 2000, **135**, 709–712.
224 F. Mauvy, *Solid State Ionics*, 2003, **158**, 17–28.
225 C. Ferchaud, J.-C. Grenier, Y. Zhang-Steenwinkel, M. M. van Tuel, F. P. van Berkel and J.-M. Bassat, *J. Power Sources*, 2011, **196**, 1872–1879.
226 A. V. Kovalevsky, V. V. Kharton, A. A. Yaremchenko, Y. V. Pivak, E. N. Naumovich and J. R. Frade, *J. Eur. Ceram. Soc.*, 2007, **27**, 4269–4272.
227 V. Vibhu, J.-M. Bassat, A. Flura, C. Nicollet, J.-C. Grenier and A. Rougier, *ECS Trans.*, 2015, **68**, 825–835.
228 C. Nicollet, A. Flura, V. Vibhu, A. Rougier, J.-M. Bassat and J.-C. Grenier, *Int. J. Hydrogen Energy*, 2016, **41**, 15538–15544.
229 G. Amow, I. Davidson and S. Skinner, *Solid State Ionics*, 2006, **177**, 1205–1210.
230 G. Amow and S. J. Skinner, *J. Solid State Electrochem.*, 2006, **10**, 538–546.
231 G. Amow, *Proc. Vol.*, 2005, **2005–2007**, 1745–1750.
232 J. M. Bassat, C. Allançon, P. Odier, J. P. Loup, M. D. Carvalho and A. Wattiaux, *Eur. J. Solid State Inorg. Chem.*, 1998, **35**, 173–188.
233 E. N. Naumovich and V. V. Kharton, *J. Mol. Struct.: THEOCHEM*, 2010, **946**, 57–64.
234 V. Vibhu, I. C. Vinke, R.-A. Eichel, J.-M. Bassat and L. de Haart, *J. Power Sources*, 2019, **444**, 227292.
235 C. Berger, A. Egger, R. Merkle, E. Bucher, B. Stuhlhofer, N. Schrödl, J. Lammer, C. Gspan, G. Logvenov, J. Maier and W. Sitte, *J. Electrochem. Soc.*, 2019, **166**, F1088–F1095.
236 T. Inprasit, S. Wongkasemjit, S. J. Skinner, M. Burriel and P. Limthongkul, *RSC Adv.*, 2015, **5**, 2486–2492.
237 J. Kilner, *Solid State Ionics*, 2002, **154–155**, 523–527.
238 I. D. Unachukwu, V. Vibhu, I. C. Vinke, R.-A. Eichel and L. G. J. de Haart, *Energies*, 2022, **15**, 2136.
239 V. Dusastre and J. A. Kilner, *Solid State Ionics*, 1999, **126**, 163–174.
240 V. Vibhu, A. Rougier, C. Nicollet, A. Flura, J.-C. Grenier and J.-M. Bassat, *Solid State Ionics*, 2015, **278**, 32–37.
241 V. Vibhu, A. Flura, A. Rougier, C. Nicollet, S. Fourcade, T. Hungria, J.-C. Grenier and J.-M. Bassat, *J. Energy Chem.*, 2020, **46**, 62–70.
242 V. Vibhu, M. R. Suchomel, N. Penin, F. Weill, J.-C. Grenier, J.-M. Bassat and A. Rougier, *Dalton Trans.*, 2018, **48**, 266–277.
243 J.-M. Bassat, V. Vibhu, C. Nicollet, A. Flura, S. Fourcade, J.-C. Grenier and A. Rougier, *ECS Trans.*, 2017, **78**, 655–665.
244 R. J. Woolley and S. J. Skinner, *J. Power Sources*, 2013, **243**, 790–795.
245 T. Ramos, J. Hjelm and M. Mogensen, *J. Electrochem. Soc.*, 2011, **158**, B814.
246 M. Brown, S. Primdahl and M. Mogensen, *J. Electrochem. Soc.*, 2000, **147**, 475.
247 R. Barfod, M. Mogensen, T. Klemensø, A. Hagen, Y.-L. Liu and P. Vang Hendriksen, *J. Electrochem. Soc.*, 2007, **154**, B371.
248 V. Haanappel, J. Mertens, D. Rutenbeck, C. Tropartz, W. Herzhof, D. Sebold and F. Tietz, *J. Power Sources*, 2005, **141**, 216–226.
249 V. A. C. Haanappel, J. Mertens and A. Mai, *J. Fuel Cell Sci. Technol.*, 2006, **3**, 263–270.
250 J. Mertens, V. A. C. Haanappel, C. Tropartz, W. Herzhof and H. P. Buchkremer, *J. Fuel Cell Sci. Technol.*, 2006, **3**, 125–130.
251 M. Mogensen, *Solid State Ionics*, 1996, **86–88**, 1151–1160.
252 M. Jørgensen, *Solid State Ionics*, 2001, **139**, 1–11.
253 M. Sase, J. Suzuki, K. Yashiro, T. Otake, A. Kaimai, T. Kawada, J. Mizusaki and H. Yugami, *Solid State Ionics*, 2006, **177**, 1961–1964.
254 D. Beckel, U. Muecke, T. Gyger, G. Florey, A. Infortuna and L. Gauckler, *Solid State Ionics*, 2007, **178**, 407–415.
255 V. Haanappel, D. Rutenbeck, A. Mai, S. Uhlenbruck, D. Sebold, H. Wesemeyer, B. Röwekamp, C. Tropartz and F. Tietz, *J. Power Sources*, 2004, **130**, 119–128.
256 A. Mai, V. A. Haanappel, S. Uhlenbruck, F. Tietz and D. Stöver, *Solid State Ionics*, 2005, **176**, 1341–1350.
257 N. H. Menzler and V. A. Haanappel, *J. Power Sources*, 2010, **195**, 5340–5343.
258 S. Uhlenbruck, N. Jordan, D. Sebold, H. P. Buchkremer, V. Haanappel and D. Stöver, *Thin Solid Films*, 2007, **515**, 4053–4060.
259 M. Sogaard, P. Hendriksen, M. Mogensen, F. Poulsen and E. Skou, *Solid State Ionics*, 2006, **177**, 3285–3296.
260 F. Han, R. Mücke, T. van Gestel, A. Leonide, N. H. Menzler, H. P. Buchkremer and D. Stöver, *J. Power Sources*, 2012, **218**, 157–162.
261 N. H. Menzler, D. Sebold, Y. J. Sohn and S. Zischke, *J. Power Sources*, 2020, **478**, 228770.
262 S. E. Wolf, V. Vibhu, E. Tröster, I. C. Vinke, R.-A. Eichel and L. G. J. de Haart, *Energies*, 2022, **15**, 5449.
263 D. Marinha, L. Dessemond, J. S. Cronin, J. R. Wilson, S. A. Barnett and E. Djurado, *Chem. Mater.*, 2011, **23**, 5340–5348.
264 D. Marinha, L. Dessemond and E. Djurado, *J. Power Sources*, 2012, **197**, 80–87.
265 O. Celikbilek, C.-A. Thieu, F. Agnese, E. Calì, C. Lenser, N. H. Menzler, J.-W. Son, S. J. Skinner and E. Djurado, *J. Mater. Chem. A*, 2019, **7**, 25102–25111.
266 R. K. Sharma, M. Burriel, L. Dessemond, V. Martin, J.-M. Bassat and E. Djurado, *J. Power Sources*, 2016, **316**, 17–28.
267 B. Joshi, E. Samuel, Y. Kim, A. L. Yarin, M. T. Swihart and S. S. Yoon, *Adv. Funct. Mater.*, 2021, **31**, 2008181.
268 D. Marinha, L. Dessemond and E. Djurado, *ECS Trans.*, 2010, **28**, 93–103.
269 R. Sayers, M. Rieu, P. Lenormand, F. Ansart, J. A. Kilner and S. J. Skinner, *Solid State Ionics*, 2011, **192**, 531–534.
270 N. Hildenbrand, P. Nammensma, D. H. Blank, H. J. Bouwmeester and B. A. Boukamp, *J. Power Sources*, 2013, **238**, 442–453.

271 M. Zhi, S. Lee, N. Miller, N. H. Menzler and N. Wu, *Energy Environ. Sci.*, 2012, **5**, 7066.
272 B. Zhang, Z. Leng, Y. Ling, H. Bai, S. Li, J. Zhou and S. Wang, *Crystals*, 2022, **12**, 1624.
273 S. T. Aruna, L. S. Balaji, S. S. Kumar and B. S. Prakash, *Renewable Sustainable Energy Rev.*, 2017, **67**, 673–682.
274 J. Nowotny, *Science of Ceramic Interfaces II*, Elsevier, Burlington, 1995.
275 W. Lee, J. W. Han, Y. Chen, Z. Cai and B. Yildiz, *J. Am. Chem. Soc.*, 2013, **135**, 7909–7925.
276 K. Szot and W. Speier, *Phys. Rev. B: Condens. Matter Mater. Phys.*, 1999, **60**, 5909–5926.
277 Y. Chen, W. Jung, Z. Cai, J. J. Kim, H. L. Tuller and B. Yildiz, *Energy Environ. Sci.*, 2012, **5**, 7979.
278 H. Yokokawa, N. Sakai, T. Kawada and M. Dokiya, *J. Electrochem. Soc.*, 1991, **138**, 2719–2727.
279 H. Yokokawa, *Solid State Ionics*, 1996, **86–88**, 1161–1165.
280 A. Mitterdorfer, *Solid State Ionics*, 1998, **111**, 185–218.
281 C. Brugnoni, *Solid State Ionics*, 1995, **76**, 177–182.
282 M. Mori, *Solid State Ionics*, 1999, **123**, 113–119.
283 H. Türk, F.-P. Schmidt, T. Götsch, F. Girgsdies, A. Hammud, D. Ivanov, I. C. Vinke, L. de Haart, R.-A. Eichel, K. Reuter, R. Schlögl, A. Knop-Gericke, C. Scheurer and T. Lunkenbein, *Adv. Mater. Interfaces*, 2021, **8**, 2100967.
284 *Developments in Solid Oxide Fuel Cells and Lithium Ion Batteries. Proceedings of the 106th Annual Meeting of the American Ceramic Society, Indianapolis, Indiana, USA (2004)*, American Ceramic Society, Westerville, Ohio, 2005, vol. 161.
285 M. Backhaus-Ricoult, K. Adib, T. S. Clair, B. Luerssen, L. Gregoratti and A. Barinov, *Solid State Ionics*, 2008, **179**, 891–895.
286 M. Backhaus-Ricoult, *Solid State Ionics*, 2006, **177**, 2195–2200.
287 Y. Chen, Y. Fan, S. Lee, G. Hackett, H. Abernathy, K. Gerdes and X. Song, *J. Power Sources*, 2019, **438**, 227043.
288 S. He, K. Chen, M. Saunders, J. Li, C. Q. Cui and S. P. Jiang, *J. Electrochem. Soc.*, 2017, **164**, F1437–F1447.
289 S. He, K. Chen, M. Saunders, Z. Quadir, S. Tao, J. T. Irvine, C. Q. Cui and S. P. Jiang, *Solid State Ionics*, 2018, **325**, 176–188.
290 H. Türk, T. Götsch, F.-P. Schmidt, A. Hammud, D. Ivanov, L. G. J. de Haart, I. C. Vinke, R.-A. Eichel, R. Schlögl, K. Reuter, A. Knop-Gericke, T. Lunkenbein and C. Scheurer, *ChemCatChem*, 2022, **14**, e202200300.
291 K. Chen and S. P. Jiang, *Int. J. Hydrogen Energy*, 2011, **36**, 10541–10549.
292 A. V. Virkar, *Int. J. Hydrogen Energy*, 2010, **35**, 9527–9543.
293 J. R. Mawdsley, J. David Carter, A. Jeremy Kropf, B. Yildiz and V. A. Maroni, *Int. J. Hydrogen Energy*, 2009, **34**, 4198–4207.
294 A. Momma, T. Kato, Y. Kaga and S. Nagata, *J. Ceram. Soc. Jpn.*, 1997, **105**, 369–373.
295 V. Brichzin, *Solid State Ionics*, 2002, **152–153**, 499–507.
296 J. Mizusaki, T. Saito and H. Tagawa, *J. Electrochem. Soc.*, 1996, **143**, 3065–3073.
297 R. Knibbe, M. L. Traulsen, A. Hauch, S. D. Ebbesen and M. Mogensen, *J. Electrochem. Soc.*, 2010, **157**, B1209.
298 J. Kim, H.-I. Ji, H. P. Dasari, D. Shin, H. Song, J.-H. Lee, B.-K. Kim, H.-J. Je, H.-W. Lee and K. J. Yoon, *Int. J. Hydrogen Energy*, 2013, **38**, 1225–1235.
299 M. Keane, M. K. Mahapatra, A. Verma and P. Singh, *Int. J. Hydrogen Energy*, 2012, **37**, 16776–16785.
300 P. Hjalmarsson, X. Sun, Y.-L. Liu and M. Chen, *J. Power Sources*, 2014, **262**, 316–322.
301 S. J. Kim and G. M. Choi, *Solid State Ionics*, 2014, **262**, 303–306.
302 Z. Pan, Q. Liu, M. Ni, R. Lyu, P. Li and S. H. Chan, *Int. J. Hydrogen Energy*, 2018, **43**, 5437–5450.
303 N. Li, M. Keane, M. K. Mahapatra and P. Singh, *Int. J. Hydrogen Energy*, 2013, **38**, 6298–6303.
304 K. Chen, N. Ai and S. P. Jiang, *Electrochem. Commun.*, 2012, **19**, 119–122.
305 H. Yokokawa, N. Sakai, T. Horita, K. Yamaji, M. E. Brito and H. Kishimoto, *J. Alloys Compd.*, 2008, **452**, 41–47.
306 J. Druce, H. Téllez, M. Burriel, M. D. Sharp, L. J. Fawcett, S. N. Cook, D. S. McPhail, T. Ishihara, H. H. Brongersma and J. A. Kilner, *Energy Environ. Sci.*, 2014, **7**, 3593–3599.
307 H. Téllez, J. Druce, Y.-W. Ju, J. Kilner and T. Ishihara, *Int. J. Hydrogen Energy*, 2014, **39**, 20856–20863.
308 H. Téllez, J. Druce, J. A. Kilner and T. Ishihara, *Faraday Discuss.*, 2015, **182**, 145–157.
309 B. Wei, M. Schroeder and M. Martin, *ACS Appl. Mater. Interfaces*, 2018, **10**, 8621–8629.
310 B. Philippeau, F. Mauvy, C. Mazataud, S. Fourcade and J.-C. Grenier, *Solid State Ionics*, 2013, **249–250**, 17–25.
311 A. Montenegro-Hernández, J. Vega-Castillo, L. Mogni and A. Caneiro, *Int. J. Hydrogen Energy*, 2011, **36**, 15704–15714.
312 A. M. Hernández, L. Mogni and A. Caneiro, *Int. J. Hydrogen Energy*, 2010, **35**, 6031–6036.
313 R. Sayers, J. Liu, B. Rustumji and S. J. Skinner, *Fuel Cells*, 2008, **8**, 338–343.
314 V. Vibhu, A. Rougier, C. Nicollet, A. Flura, S. Fourcade, N. Penin, J.-C. Grenier and J.-M. Bassat, *J. Power Sources*, 2016, **317**, 184–193.
315 S. Badwal, R. Deller, K. Foger, Y. Ramprakash and J. Zhang, *Solid State Ionics*, 1997, **99**, 297–310.
316 S. Taniguchi, M. Kadowaki, H. Kawamura, T. Yasuo, Y. Akiyama, Y. Miyake and T. Saitoh, *J. Power Sources*, 1995, **55**, 73–79.
317 S. C. Paulson and V. I. Birss, *J. Electrochem. Soc.*, 2004, **151**, A1961.
318 K. Schiemann, V. Vibhu, S. Yildiz, I. C. Vinke, R.-A. Eichel and L. de Haart, *ECS Trans.*, 2017, **78**, 1027–1034.
319 L. G. J. de Haart, J. Mougin, O. Posdziech, J. Kiviaho and N. H. Menzler, *Fuel Cells*, 2009, **9**, 794–804.
320 L. Blum, Q. Fang, S. M. Groß-Barsnick, L. de Haart, J. Malzbender, N. H. Menzler and W. J. Quadakkers, *Int. J. Hydrogen Energy*, 2020, **45**, 8955–8964.
321 N. H. Menzler, D. Sebold and Q. Fang, *Meeting Abstracts*, 2015, **MA2015-03**, p. 25.
322 M. Kornely, A. Neumann, N. H. Menzler, A. Weber and E. Ivers-Tiffée, *ECS Trans.*, 2011, **35**, 2009–2017.

323 Q. Fang, N. H. Menzler and L. Blum, *J. Electrochem. Soc.*, 2021, **168**, 104505.
324 S. P. Jiang, J. P. Zhang, L. Apateanu and K. Foger, *J. Electrochem. Soc.*, 2000, **147**, 4013.
325 T. Horita, Y. Xiong, M. Yoshinaga, H. Kishimoto, K. Yamaji, M. E. Brito and H. Yokokawa, *Electrochem. Solid-State Lett.*, 2009, **12**, B146.
326 K. Chen, J. Hyodo, A. Dodd, N. Ai, T. Ishihara, L. Jian and S. P. Jiang, *Faraday Discuss.*, 2015, **182**, 457–476.
327 S. P. Jiang and X. Chen, *Int. J. Hydrogen Energy*, 2014, **39**, 505–531.
328 B. Wei, K. Chen, L. Zhao, Z. Lü and S. P. Jiang, *Phys. Chem. Chem. Phys.*, 2015, **17**, 1601–1609.
329 V. I. Sharma and B. Yildiz, *J. Electrochem. Soc.*, 2010, **157**, B441.
330 P. Qiu, J. Lin, L. Lei, Z. Yuan, L. Jia, J. Li and F. Chen, *ACS Appl. Energy Mater.*, 2019, **2**, 7619–7627.
331 B. Wei, K. Chen, C. C. Wang, Z. Lü and S. P. Jiang, *Electrochim. Acta*, 2015, **174**, 327–331.
332 N. Schrödl, A. Egger, C. Gspan, T. Höschen, F. Hofer and W. Sitte, *Solid State Ionics*, 2018, **322**, 44–53.
333 N. Schrödl, A. Egger, J. Lammer, F. Hofer and W. Sitte, *J. Electrochem. Soc.*, 2021, **168**, 14509.
334 S.-N. Lee, A. Atkinson and J. A. Kilner, *ECS Trans.*, 2013, **57**, 605–613.
335 K. J. Lee, J. H. Chung, M. J. Lee and H. J. Hwang, *J. Korean Ceram. Soc.*, 2019, **56**, 160–166.
336 J. Schuler, H. Lübbe, A. Hessler-Wyser and J. van Herle, *J. Power Sources*, 2012, **213**, 223–228.
337 M. A. Laguna-Bercero, *J. Power Sources*, 2012, **203**, 4–16.
338 M. Ni, M. K. H. Leung and D. Y. C. Leung, *Chem. Eng. Technol.*, 2006, **29**, 636–642.
339 H. Dau, C. Limberg, T. Reier, M. Risch, S. Roggan and P. Strasser, *ChemCatChem*, 2010, **2**, 724–761.
340 F. Thaler, Q. Fang, U. de Haart, L. G. J. de Haart, R. Peters and L. Blum, *ECS Trans.*, 2021, **103**, 363–374.
341 K. Zhao, Q. Bkour, X. Hou, S. W. Kang, J. C. Park, M. G. Norton, J.-I. Yang and S. Ha, *Chem. Eng. J.*, 2018, **336**, 20–27.
342 S.-D. Kim, D.-W. Seo, A. K. Dorai and S.-K. Woo, *Int. J. Hydrogen Energy*, 2013, **38**, 6569–6576.
343 A. Hauch, S. D. Ebbesen, S. H. Jensen and M. Mogensen, *J. Electrochem. Soc.*, 2008, **155**, B1184–B1193.
344 M. H. Pihlatie, A. Kaiser, M. Mogensen and M. Chen, *Solid State Ionics*, 2011, **189**, 82–90.
345 M. A. Laguna-Bercero, A. R. Hanifi, L. Menand, N. K. Sandhu, N. E. Anderson, T. H. Etsell and P. Sarkar, *Electrochim. Acta*, 2018, **268**, 195–201.
346 L. Mingyi, Y. Bo, X. Jingming and C. Jing, *Int. J. Hydrogen Energy*, 2010, **35**, 2670–2674.
347 C. Neofytidis, E. Ioannidou, L. Sygellou, M. Kollia and D. K. Niakolas, *J. Catal.*, 2019, **373**, 260–275.
348 S. P. Jiang and S. H. Chan, *J. Mater. Sci.*, 2004, **39**, 4405–4439.
349 D. A. Osinkin, D. I. Bronin, S. M. Beresnev, N. M. Bogdanovich, V. D. Zhuravlev, G. K. Vdovin and T. A. Demyanenko, *J. Solid State Electrochem.*, 2014, **18**, 149–156.
350 S.-Y. Park, C. W. Na, J. H. Ahn, U.-J. Yun, T.-H. Lim, R.-H. Song, D.-R. Shin and J.-H. Lee, *J. Power Sources*, 2012, **218**, 119–127.
351 V. Gil, J. Tartaj and C. Moure, *Ceram. Int.*, 2009, **35**, 839–846.
352 S. Aruna, M. Muthuraman and K. Patil, *Solid State Ionics*, 1998, **111**, 45–51.
353 E. Drożdż, J. Wyrwa and M. Rękas, *Ionics*, 2013, **19**, 1733–1743.
354 A. K. Soman, P. Kuppusami and A. M. Rabel, 2017, **17**, pp. 224–236.
355 S. P. Patil, L. D. Jadhav and M. Chourashiya, *Open Ceram.*, 2022, **9**, 100230.
356 A. Brisse, J. Schefold and M. Zahid, *Int. J. Hydrogen Energy*, 2008, **33**, 5375–5382.
357 C. Xi, J. Sang, A. Wu, J. Yang, X. Qi, W. Guan, J. Wang and S. C. Singhal, *Int. J. Hydrogen Energy*, 2022, **47**, 10166–10174.
358 Z. Zhan, W. Kobsiriphat, J. R. Wilson, M. Pillai, I. Kim and S. A. Barnett, *Energy Fuels*, 2009, **23**, 3089–3096.
359 Y. Tao, S. D. Ebbesen and M. B. Mogensen, *J. Power Sources*, 2016, **328**, 452–462.
360 M. Zheng, S. Wang, Y. Yang and C. Xia, *J. Mater. Chem. A*, 2018, **6**, 2721–2729.
361 V. Singh, H. Muroyama, T. Matsui and K. Eguchi, *ECS Trans.*, 2014, **64**, 53–64.
362 I. D. Unachukwu, V. Vibhu, I. C. Vinke, R.-A. Eichel and L. de Haart, *J. Power Sources*, 2023, **556**, 232436.
363 V. Vibhu, I. C. Vinke, F. Zaravelis, S. G. Neophytides, D. K. Niakolas, R.-A. Eichel and L. G. J. de Haart, *Energies*, 2022, **15**, 2726.
364 J. Zhou, Z. Ma, L. Zhang, C. Liu, J. Pu, X. Chen, Y. Zheng and S. H. Chan, *Int. J. Hydrogen Energy*, 2019, **44**, 28939–28946.
365 Z. Ma, Y. Li, Y. Zheng, W. Li, X. Chen, X. Sun, X. Chen and J. Zhou, *Ceram. Int.*, 2021, **47**, 23350–23361.
366 C. Jin, C. Yang, F. Zhao, D. Cui and F. Chen, *Int. J. Hydrogen Energy*, 2011, **36**, 3340–3346.
367 R. Xing, Y. Wang, S. Liu and C. Jin, *J. Power Sources*, 2012, **208**, 276–281.
368 S. Chen, K. Xie, D. Dong, H. Li, Q. Qin, Y. Zhang and Y. Wu, *J. Power Sources*, 2015, **274**, 718–729.
369 S. Tao and J. T. S. Irvine, *J. Electrochem. Soc.*, 2004, **151**, A252.
370 Y. Song, Q. Zhong and W. Tan, *Int. J. Hydrogen Energy*, 2014, **39**, 13694–13700.
371 K.-T. Wu and T. Ishihara, *ECS Trans.*, 2021, **103**, 561–567.
372 T. Ishihara, S. Wang and K.-T. Wu, *Solid State Ionics*, 2017, **299**, 60–63.
373 F. Tietz, I. A. Raj, M. Zahid, A. Mai and D. Stöver, *Prog. Solid State Chem.*, 2007, **35**, 539–543.
374 Y. S. Chung, T. Kim, T. H. Shin, H. Yoon, S. Park, N. M. Sammes, W. B. Kim and J. S. Chung, *J. Mater. Chem. A*, 2017, **5**, 6437–6446.
375 F. Y. Farsani, M. Jafari, E. Shahsavari and H. Salamati, *Int. J. Hydrogen Energy*, 2020, **45**, 8915–8929.

376 X. Peng, Y. Tian, Y. Liu, W. Wang, L. Jia, J. Pu, B. Chi and J. Li, *J. CO_2 Util.*, 2020, **36**, 18–24.
377 F. B. Wede, Master thesis, TU Graz, 2013.
378 S. Wang and T. Ishihara, *ECS Trans.*, 2013, **57**, 3171–3176.
379 Q. Qin, K. Xie, H. Wei, W. Qi, J. Cui and Y. Wu, *RSC Adv.*, 2014, **4**, 38474–38483.
380 O. Marina, *Solid State Ionics*, 2002, **149**, 21–28.
381 Q. X. Fu, F. Tietz and D. Stöver, *J. Electrochem. Soc.*, 2006, **153**, D74.
382 D. Neagu and J. T. S. Irvine, *Chem. Mater.*, 2010, **22**, 5042–5053.
383 S. Li, Y. Li, Y. Gan, K. Xie and G. Meng, *J. Power Sources*, 2012, **218**, 244–249.
384 Y. Li, J. Zhou, D. Dong, Y. Wang, J. Z. Jiang, H. Xiang and K. Xie, *Phys. Chem. Chem. Phys.*, 2012, **14**, 15547–15553.
385 S. Paydar, O. Korjus, M. Maide, I. Kivi, E. Lust and G. Nurk, *ECS Trans.*, 2021, **103**, 1971–1979.
386 O. A. Marina, L. R. Pederson, M. C. Williams, G. W. Coffey, K. D. Meinhardt, C. D. Nguyen and E. C. Thomsen, *J. Electrochem. Soc.*, 2007, **154**, B452.
387 W. Qi, Y. Gan, D. Yin, Z. Li, G. Wu, K. Xie and Y. Wu, *J. Mater. Chem. A*, 2014, **2**, 6904–6915.
388 S. E. Wolf, V. Vibhu, C. L. Coll, N. Eyckeler, I. C. Vinke, R.-A. Eichel and L. de Haart, *ECS Trans.*, 2023, **111**, 2119–2130.
389 S. Zhang, K. Zhu, X. Hu, R. Peng and C. Xia, *J. Mater. Chem. A*, 2021, **9**, 24336–24347.
390 Y. Jiang, Y. Yang, C. Xia and H. J. M. Bouwmeester, *J. Mater. Chem. A*, 2019, **7**, 22939–22949.
391 Y. Wang, T. Liu, M. Li, C. Xia, B. Zhou and F. Chen, *J. Mater. Chem. A*, 2016, **4**, 14163–14169.
392 Y. Li, B. Hu, C. Xia, W. Q. Xu, J. P. Lemmon and F. Chen, *J. Mater. Chem. A*, 2017, **5**, 20833–20842.
393 B.-W. Zhang, M.-N. Zhu, M.-R. Gao, X. Xi, N. Duan, Z. Chen, R.-F. Feng, H. Zeng and J.-L. Luo, *Nat. Commun.*, 2022, **13**, 4618.
394 C. Li, Y. Deng, L. Yang, B. Liu, D. Yan, L. Fan, J. Li and L. Jia, *Adv. Powder Mater.*, 2023, **2**, 100133.
395 K. Kamlungsua and P.-C. Su, *Electrochim. Acta*, 2020, **355**, 136670.
396 N. Dai, Z. Wang, T. Jiang, J. Feng, W. Sun, J. Qiao, D. Rooney and K. Sun, *J. Power Sources*, 2014, **268**, 176–182.
397 R. D. Shannon, *Acta Crystallogr., Sect. A*, 1976, **32**, 751–767.
398 T. Xia, N. Lin, H. Zhao, L. Huo, J. Wang and J.-C. Grenier, *J. Power Sources*, 2009, **192**, 291–296.
399 R. Lan, P. I. Cowin, S. Sengodan and S. Tao, *Sci. Rep.*, 2016, **6**, 31839.
400 B. Ge, J. T. Ma, D. Ai, C. Deng, X. Lin and J. Xu, *Electrochim. Acta*, 2015, **151**, 437–446.
401 B. Ge, J. Sheng, Y. Zhuang, J. Ma, Z. Yang, C. Li and S. Peng, *Mater. Res. Express*, 2020, **7**, 56302.
402 S. Tao, J. Canales-Vázquez and J. T. S. Irvine, *Chem. Mater.*, 2004, **16**, 2309–2316.
403 R. Fu, P. Jiang, H. Xu, B. Niu, F. Jiang, L. Yang, T. Feng and T. He, *Int. J. Hydrogen Energy*, 2019, **44**, 31394–31405.
404 J. Zhou, *Mater. Lett.*, 2019, **257**, 126758.
405 B. S. Teketel, B. A. Beshiwork, D. Tian, S. Zhu, H. G. Desta, K. Kashif, Y. Chen and B. Lin, *Catalysts*, 2022, **12**, 488.
406 S. Sengodan, S. Choi, A. Jun, T. H. Shin, Y.-W. Ju, H. Y. Jeong, J. Shin, J. T. S. Irvine and G. Kim, *Nat. Mater.*, 2015, **14**, 205–209.
407 H. Ding, Z. Tao, S. Liu and J. Zhang, *Sci. Rep.*, 2015, **5**, 18129.
408 R. M. Clemmer and S. F. Corbin, *Solid State Ionics*, 2009, **180**, 721–730.
409 S. K. Pratihar, A. Dassharma and H. S. Maiti, *J. Mater. Sci.*, 2007, **42**, 7220–7226.
410 A. R. Hanifi, M. A. Laguna-Bercero, N. K. Sandhu, T. H. Etsell and P. Sarkar, *Sci. Rep.*, 2016, **6**, 27359.
411 M. B. Mogensen, M. Chen, H. L. Frandsen, C. Graves, A. Hauch, P. V. Hendriksen, T. Jacobsen, S. H. Jensen, T. L. Skafte and X. Sun, *Fuel Cells*, 2021, **21**, 415–429.
412 F. Monaco, M. Hubert, J. Vulliet, J. P. Ouweltjes, D. Montinaro, P. Cloetens, P. Piccardo, F. Lefebvre-Joud and J. Laurencin, *J. Electrochem. Soc.*, 2019, **166**, F1229–F1242.
413 A. Hauch, K. Brodersen, M. Chen and M. B. Mogensen, *Solid State Ionics*, 2016, **293**, 27–36.
414 A. Hauch, PhD thesis, Risoe National Lab., DTU, Roskilde, Denmark, 2007.
415 A. Hagen, R. Barfod, P. V. Hendriksen, Y.-L. Liu and S. Ramousse, *J. Electrochem. Soc.*, 2006, **153**(6), A1165–A1171.
416 A. Hauch, S. D. Ebbesen, S. H. Jensen and M. Mogensen, *J. Mater. Chem.*, 2008, **18**(20), 2331–2340.
417 M. Trini, A. Hauch, S. de Angelis, X. Tong, P. V. Hendriksen and M. Chen, *J. Power Sources*, 2020, **450**, 227599.
418 S. He and S. P. Jiang, *Prog. Mater. Sci.*, 2021, **31**, 341–372.
419 Q. Fang, L. Blum, N. H. Menzler and D. Stolten, *ECS Trans.*, 2017, **78**, 2885–2893.
420 M. Trini, P. S. Jørgensen, A. Hauch, J. J. Bentzen, P. V. Hendriksen and M. Chen, *J. Electrochem. Soc.*, 2019, **166**, F158–F167.
421 S. D. Ebbesen, X. Sun and M. B. Mogensen, *Faraday Discuss.*, 2015, **182**, 393–422.
422 Y. Wang, W. Li, L. Ma, W. Li and X. Liu, *J. Mater. Sci. Technol.*, 2020, **55**, 35–55.
423 P. Moçoteguy and A. Brisse, *Int. J. Hydrogen Energy*, 2013, **38**, 15887–15902.
424 X. Sun, Y. Liu, P. V. Hendriksen and M. Chen, *J. Power Sources*, 2021, **506**, 230136.
425 C. E. Frey, Q. Fang, D. Sebold, L. Blum and N. H. Menzler, *J. Electrochem. Soc.*, 2018, **165**, F357–F364.
426 F. Tietz, D. Sebold, A. Brisse and J. Schefold, *J. Power Sources*, 2013, **223**, 129–135.
427 Q. Fang, L. Blum, N. H. Menzler and D. Stolten, *ECS Trans.*, 2017, **78**, 2885–2893.
428 J. Uecker, I. D. Unachukwu, V. Vibhu, I. C. Vinke, R.-A. Eichel and L. de Haart, *Electrochim. Acta*, 2023, **452**, 142320.
429 Y. Song, Z. Zhou, X. Zhang, Y. Zhou, H. Gong, H. Lv, Q. Liu, G. Wang and X. Bao, *J. Mater. Chem. A*, 2018, **6**, 13661–13667.

430 J. Schefold, A. Brisse, A. Surrey and C. Walter, *Int. J. Hydrogen Energy*, 2020, **45**, 5143–5154.
431 C. K. Lim, Q. Liu, J. Zhou, Q. Sun and S. H. Chan, *Fuel Cells*, 2017, **17**, 464–472.
432 D. Schäfer, L. Queda, V. Nischwitz, Q. Fang and L. Blum, *Processes*, 2022, **10**, 598.
433 D. Schäfer, T. Janßen, Q. Fang, F. Merten and L. Blum, *Energies*, 2021, **14**, 544.
434 W. Z. Zhu and S. C. Deevi, *Mater. Sci. Eng., A*, 2003, **348**, 227–243.
435 S. Fontana, R. Amendola, S. Chevalier, P. Piccardo, G. Caboche, M. Viviani, R. Molins and M. Sennour, *J. Power Sources*, 2007, **171**, 652–662.
436 K. Huang and S. C. Singhal, *J. Power Sources*, 2013, **237**, 84–97.
437 S. Geng, J. Zhu and Z. Lu, *Solid State Ionics*, 2006, **177**, 559–568.
438 B. Königshofer, M. Höber, G. Nusev, P. Boškoski, C. Hochenauer and V. Subotić, *J. Power Sources*, 2022, **523**, 230982.
439 R. Sachitanand, J.-E. Svensson and J. Froitzheim, *Oxid. Met.*, 2015, **84**, 241–257.
440 M. Stanislowski, E. Wessel, K. Hilpert, T. Markus and L. Singheiser, *J. Electrochem. Soc.*, 2007, **154**, A295.
441 S. Fontana, S. Chevalier and G. Caboche, *Oxid. Met.*, 2012, **78**, 307–328.
442 B. Talic, H. Falk-Windisch, V. Venkatachalam, P. V. Hendriksen, K. Wiik and H. L. Lein, *J. Power Sources*, 2017, **354**, 57–67.
443 R. Vaßen, N. Grünwald, D. Marcano, N. H. Menzler, R. Mücke, D. Sebold, Y. J. Sohn and O. Guillon, *Surf. Coat. Technol.*, 2016, **291**, 115–122.
444 N. Grünwald, D. Sebold, Y. J. Sohn, N. H. Menzler and R. Vaßen, *J. Power Sources*, 2017, **363**, 185–192.
445 M. Kornely, N. H. Menzler, A. Weber and E. Iver-Tiffée, *Meeting Abstracts*, 2012, **MA2012-02**, p. 1972.
446 M. Bianco, J. Tallgren, J.-E. Hong, S. Yang, O. Himanen, J. Mikkola, J. van Herle and R. Steinberger-Wilckens, *J. Power Sources*, 2019, **437**, 226900.
447 S. Frangini, A. Masi, L. Della Seta, M. Bianco and J. van Herle, *J. Electrochem. Soc.*, 2018, **165**, F97–F104.
448 M. M. Del Juez Lorenzo, V. Kolarik, V. Kuchenreuther-Hummel, M. Pötschke and D. Schimanke, *Oxid. Met.*, 2017, **88**, 279–290.
449 C.-H. Park and K.-H. Baik, *Met. Mater. Int.*, 2014, **20**, 63–67.
450 N. H. Menzler, D. Sebold and O. Guillon, *J. Power Sources*, 2018, **374**, 69–76.
451 J. Malzbender, P. Batfalsky, R. Vaßen, V. Shemet and F. Tietz, *J. Power Sources*, 2012, **201**, 196–203.
452 N. Grünwald, P. Lhuissier, L. Salvo, J. Villanova, N. H. Menzler, O. Guillon, C. L. Martin and R. Vaßen, *J. Mater. Sci.*, 2020, **55**, 12725–12736.
453 N. Grünwald, Y. J. Sohn, X. Yin, N. H. Menzler, O. Guillon and R. Vaßen, *J. Eur. Ceram. Soc.*, 2019, **39**, 449–460.
454 J. Zurek, N. Margaritis, D. Naumenko, N. H. Menzler and W. J. Quadakkers, *Oxid. Met.*, 2019, **92**, 353–377.
455 K. Sick, N. Grigorev, N. H. Menzler and O. Guillon, in *Proceeding of the 42nd International Conference on Advanced Ceramics and Composites*, ed. J. Salem, D. Koch, P. Mechnich, M. Kusnezoff, N. Bansal, J. LaSalvia, P. Balaya, Z. Fu and T. Ohji, John Wiley & Sons, Inc, Hoboken, NJ, USA, 2019, pp. 99–111.
456 Z. Yang, G. Xia, P. Singh and J. W. Stevenson, *J. Power Sources*, 2006, **155**, 246–252.
457 J. Kupecki, R. Kluczowski, D. Papurello, A. Lanzini, M. Kawalec, M. Krauz and M. Santarelli, *Int. J. Hydrogen Energy*, 2019, **44**, 19405–19411.
458 D. Yan, C. Zhang, L. Liang, K. Li, L. Jia, J. Pu, L. Jian, X. Li and T. Zhang, *Appl. Energy*, 2016, **175**, 414–420.
459 W. Wu, G. L. Wang, W. B. Guan, Y. F. Zhen and W. G. Wang, *Fuel Cells*, 2013, **13**(5), 743–750.
460 M. C. Tucker, L. Cheng and L. C. DeJonghe, *J. Power Sources*, 2011, **196**, 8313–8322.
461 X. Li, S. M. Groß-Barsnick, T. Koppitz, S. Baumann, W. A. Meulenberg and G. Natour, *J. Eur. Ceram. Soc.*, 2022, **42**, 2879–2891.
462 Y. Mizutani, M. Tamura, M. Kawai and O. Yamamoto, *Solid State Ionics*, 1994, **72**, 271–275.
463 A. Hammouche, E. Siebert and A. Hammou, *Mater. Res. Bull.*, 1989, **24**, 367–380.
464 J. Xiang, Z.-G. Liu, J.-H. Ouyang and F.-Y. Yan, *J. Power Sources*, 2014, **251**, 305–310.
465 L. Blum, L. de Haart, J. Malzbender, N. H. Menzler, J. Remmel and R. Steinberger-Wilckens, *J. Power Sources*, 2013, **241**, 477–485.
466 F. Tietz, A. Schmidt and M. Zahid, *J. Solid State Chem.*, 2004, **177**, 745–751.
467 M.-F. Han, X. Du and Z. Liu, *ECS Trans.*, 2009, **25**, 1379–1386.
468 X. Montero, N. Jordán, J. Pirón-Abellán, F. Tietz, D. Stöver, M. Cassir and I. Villarreal, *J. Electrochem. Soc.*, 2009, **156**, B188.
469 X. Montero, F. Tietz, D. Sebold, H. P. Buchkremer, A. Ringuede, M. Cassir, A. Laresgoiti and I. Villarreal, *J. Power Sources*, 2008, **184**, 172–179.
470 C. Yang, A. Coffin and F. Chen, *Int. J. Hydrogen Energy*, 2010, **35**, 3221–3226.
471 M. Liang, B. Yu, M. Wen, J. Chen, J. Xu and Y. Zhai, *J. Power Sources*, 2009, **190**, 341–345.
472 Y. Tao, S. D. Ebbesen and M. B. Mogensen, *J. Electrochem. Soc.*, 2014, **161**, F337–F343.
473 Y. Li, Z. Zhan and C. Xia, *Catal. Sci. Technol.*, 2018, **8**, 980–984.
474 V. Vibhu, I. C. Vinke, R.-A. Eichel and L. G. J. de Haart, *ECS Trans.*, 2021, **103**, 1505–1515.
475 A. Usenka, V. Pankov, V. Vibhu, A. Flura, J.-C. Grenier and J.-M. Bassat, *ECS Trans.*, 2019, **91**, 1341–1353.
476 V. Vibhu, I. C. Vinke, R.-A. Eichel, J.-M. Bassat and L. de Haart, *ECS Trans.*, 2019, **91**, 1327–1339.
477 T. Ogier, F. Mauvy, J.-M. Bassat, J. Laurencin, J. Mougin and J.-C. Grenier, *Int. J. Hydrogen Energy*, 2015, **40**, 15885–15892.

